Structure-activity-selectivity relationships for iron-based catalysts in CO₂ Fischer-Tropsch synthesis

Dissertation

zur Erlangung des akademischen Grades
Doctor rerum naturalium
(Dr. rer. nat.)

der Matematisch-Naturwissenschaftlichen Fakultät
der Universität Rostock

vorgelegt von

Diplom-Chemiker Andrey Skrypnik

geboren am 16. September 1995 in Kemerowo, Russland

Rostock 2022

I

Gutachter

1. Gutachter:

    Prof. Dr. habil. Evgenii V. Kondratenko

    Leibniz-Institut für Katalyse e.V. an der Universität Rostock (Deutschland)

2. Gutachter:

    Prof. Dr. Malte Behrens

    Christian-Albrechts-Universität zu Kiel (Deutschland)

Tag der Einreichung: 22. August 2022

Tag der mündlichen Prüfung: 6. Dezember 2022

Zusammenfassung

Der stetige Anstieg der anthropogenen CO_2-Emissionen in die Atmosphäre kann zu einer globalen Erwärmung und anderen schädlichen Klimawandelphänomenen führen. In dieser Hinsicht ist die direkte CO_2-Hydrierung zu synthetischen Kraftstoffen oder niederen Olefinen (C_2-C_4-Alkenen), auch bekannt als CO_2-Fischer-Tropsch-Synthese (CO_2-FTS), eine attraktive Möglichkeit, "Netto-Null" humanbedingte CO_2-Emissionen zu erreichen. Eisenhaltige Katalysatoren werden in der Regel für die CO_2-FTS aufgrund ihrer Umweltfreundlichkeit, niedrigen Kosten, hohen Aktivität und attraktiven Selektivität zu höheren Kohlenwasserstoffen (hauptsächlich zu Olefinen) eingesetzt. Einer der Hauptnachteile solcher Katalysatoren ist jedoch die ausgeprägte Bildung von CH_4, das als unerwünschtes Produkt angesehen wird.

Diese Arbeit ist auf die Aufklärung von Grundlagen fokussiert, die für die zielgerichtete Herstellung von eisenhaltigen Katalysatoren für die CO_2-Hydrierung zu höheren Kohlenwasserstoffen (C_{2+}-Kohlenwasserstoffe) mit unterdrückter Methanproduktion relevant sind. Dazu wurden Katalysatorpräparation und Materialcharakterisierung durch modernste Techniken mit ortsaufgelösten stationären und transienten kinetischen Analysen kombiniert.

Es ist bekannt, dass die Methan-Bildung an Katalysatoren im stationären Zustand durch CO-Hydrierung an metallischem Eisen erfolgt. Fe_3O_4, welches die umgekehrte Wassergas-Shift-Reaktion (RWGS) katalysiert, ist außerdem für die CO_2-Hydrierung zu CH_4 verantwortlich. Daher könnte die unerwünschte Methanbildung durch Minimierung der Gehalte an metallischem Fe und Fe_3O_4 in der stationären Katalysatorzusammensetzung zugunsten von Eisencarbiden, die für die Bildung von C_{2+}-Kohlenwasserstoffen verantwortlich sind, unterdrückt werden. Die Reduzierbarkeit des Fe_2O_3 in frischen Katalysatoren wurde als wichtiger Deskriptor für die *in-situ*-Bildung von Fe_5C_2 und dessen Fähigkeit, Methan zu bilden, festgestellt. Diese Eigenschaft von Eisen(III)-oxid kann durch die Größe von α-Fe_2O_3-Kristalliten und das Verhältnis von α-Fe_2O_3 zu γ-Fe_2O_3 eingestellt werden. Zwar erleichtert eine höhere Reduzierbarkeit die CO-Hydrierung zu Methan, sie senkt jedoch stark den Beitrag der direkten CO_2-Methanisierung, sodass eine geringere Gesamtbildung von CH_4 stattfindet. Die Morphologie des Eisens-(II)-oxalat-dihydrats, das als Präkursor zur Herstellung von Eisenoxiden verwendet wird, hat den größten Einfluss auf die Methan-Selektivität. Die Morphologie beeinflusst die Abweichung des *in situ* gebildeten Fe_5C_2 von der stöchiometrischen Zusammensetzung (Verhältnis von C/Fe). Je geringer diese Abweichung ist, desto geringer ist die Fähigkeit von Fe_5C_2, Wasserstoff zu aktivieren, und desto höher ist dessen Fähigkeit, CO und CO_2 zu adsorbieren. Dies führt zu einer Senkung der

Reaktionsgeschwindigkeit der gesamten CO_2-Umsetzung und sowohl zu einem höheren Olefin-zu-Paraffin-Verhältnis ($O(C_2\text{-}C_4)/P(C_2\text{-}C_4)$) als auch zu einem höheren Verhältnis der Bildungsgeschwindigkeiten von C_{2+}-Kohlenwasserstoffen und CH_4.

Eine weitere Möglichkeit, die Reaktionsgeschwindigkeit der gesamten CO_2-Umsetzung zu kontrollieren, ist die Verwendung von Alkalimetallen als Promotor. Es wurde eine positive Korrelation zwischen der Elektronegativität dieser Promotoren gemäß der Pauling-Skala und der anfänglichen Reaktionsgeschwindigkeit des gesamten CO_2-Umsatzes festgestellt. Obwohl jedes Alkalimetall die Selektivität zu C_{2+}-Kohlenwasserstoffen erhöht und die Methanproduktion hindert, bestimmt die Art des Promotors die Ursache des letzteren Effekts, der die direkte CO_2-Methanisierung und die sekundäre CO-Hydrierung zu Methan beeinflusst. Die letztgenannte Reaktion ist der Hauptweg der CH_4-Bildung an Rb- oder Cs-dotierten Katalysatoren, während die direkte CO_2-Methanisierung an nichtdotierten sowie Li-, Na- oder K-haltigen Materialien überwiegt. Obgleich die Fähigkeit des Alkalimetall-Promotors die Selektivität zu C_{2+}-Kohlenwasserstoffen und das $O(C_2\text{-}C_4)/P(C_2\text{-}C_4)$-Verhältnis zu erhöhen sowie die Methan-Selektivität zu hindern nicht von der verwendeten Menge an Alkalimetallen abhängt, gibt es einen optimalen Promotorgehalt, um die höchste Katalysatorleistung zu erzielen.

Abstract

The steady increase of anthropogenic CO_2 emissions into the atmosphere can result in global warming and other harmful climate change phenomena. In this regard, direct CO_2 hydrogenation to synthetic fuels or lower olefins (C_2-C_4 alkenes) as well known as CO_2 Fischer-Tropsch synthesis (CO_2-FTS) is an attractive approach to achieve "net-zero" human-related CO_2 emissions. Fe-based catalysts are usually applied for CO_2-FTS because of their non-toxicity, low cost, high activity and attractive selectivity to higher hydrocarbons (mainly to olefins). However, one of the major drawbacks of such catalysts is high selectivity to methane, which is regarded as an undesired product.

This study focuses on the evaluation of fundamentals relevant for the purposeful preparation of Fe-based catalysts for CO_2 hydrogenation to higher hydrocarbons (C_{2+}-hydrocarbons) with suppressed methane production. For this purpose, tailored catalyst preparation, sophisticated material characterization by state-of-the-art techniques were combined with spatially resolved steady-state and transient kinetic analyses. It was found that metallic iron in steady-state catalysts facilitates the CO hydrogenation to CH_4. Fe_3O_4 is responsible for CO_2 hydrogenation towards CH_4 in addition to catalyzing the reverse water gas shift (RWGS) reaction. Respectively, the undesired methane formation could be hindered by minimizing the contents of metallic Fe and Fe_3O_4 in the steady-state catalyst composition in favor of iron carbides responsible for the formation of C_{2+}-hydrocarbons. The reducibility of fresh catalysts was established to be an important descriptor for *in situ* formation of Fe_5C_2 and the ability of the latter to form methane. This property of iron (III) oxide can be tuned through the size of α-Fe_2O_3 crystallites and the ratio of α-Fe_2O_3 to γ-Fe_2O_3. Higher reducibility facilitates the CO hydrogenation to methane, but strongly lowers the contribution of the direct CO_2 methanation, thus, ensuring lower total CH_4 formation. The morphology of iron (II) oxalate dihydrate precursor used for the preparation of iron oxides has the largest influence on the selectivity to methane. The morphology affects the deviation from the stoichiometric composition of *in situ* formed Fe_5C_2, which is expressed as the ratio of C/Fe. The lower the deviation is, the lower the ability of Fe_5C_2 to activate H_2 and the higher the ability to adsorb CO and CO_2 is. This results in lowering the overall rate of CO_2 consumption, but higher olefin to paraffin ratio among C_2-C_4-hydrocarbons (O(C_2-C_4)/P(C_2-C_4)) and higher C_{2+}-hydrocarbons/CH_4 formation rate ratio.

Another way to control the overall rate of CO_2 consumption is the usage of alkali promoters. A positive correlation between the electronegativity of the promoter according to the Pauling scale and the overall initial CO_2 consumption rate was established. Any promoter enhances the

selectivity to C_{2+}-hydrocarbons and hinders the selectivity to CH_4. However, the origin of the latter effect depends on the nature of the promoter, which influences the direct CO_2 methanation and secondary CO hydrogenation to methane. The latter reaction is the dominant pathway of CH_4 production over Rb- or Cs-doped catalysts, while the direct CO_2 methanation prevails over non-promoted, Li-, Na- or K-promoted materials. Although any amount of alkali metal promoter positively influences the selectivity to C_{2+}-hydrocarbons and the $O(C_2-C_4)/P(C_2-C_4)$ ratio as well as hinders the selectivity to CH_4, there is an optimal dopant content to achieve the highest performance.

Eidesstattliche Versicherung

Hiermit versichere ich, Andrey Skrypnik, dass ich die vorliegende Dissertation selbständig verfasst habe. Die benutzten Hilfsmittel wurden in der Arbeit aufgeführt.

Acknowledgment

Table of Contents

Abbreviations and symbols

AMU	atomic mass unit
ASF	Anderson-Schulz-Flory
BET	Brunauer-Emmett-Teller
CCS	carbon capture and storage
CCU	carbon capture and utilization
CRI	Carbon Recycling International
CSR	coherent scattering region
DME	dimethyl ether
DRIFT	diffuse reflectance infrared Fourier transform
FID	flame ionization detector
FTS	Fischer-Tropsch synthesis
GHSV	gas hourly space velocity
ICDD	International Center of Diffraction Data
NBR	nitrile butadiene rubber
MS	mass spectrometry
MTBE	methyl tert-butyl ether
MTO	methanol to olefins
MFTS	modified Fischer-Tropsch synthesis
PE	polyethylene
PET	polyethylene terephthalate
PP	polypropylene
PS	polystyrene
PVC	polyvinyl chloride
RWGS	reverse water gas shift
SBR	styrene butadiene rubber
SEM	scanning electron microscopy
Syngas	synthesis gas
TAP	temporal analysis of products
TCD	thermal conductivity detector
TEM	transmission electron microscopy
TGA	thermogravimetric analysis
TPR	temperature-programmed reduction
XRD	X-ray diffraction

XPS	X-ray photoelectron spectroscopy
a_i	number of carbon atoms
B_{hf}	magnetic hyperfine field (T)
C_{total}	total concentration of surface species
$D_{Knudsen}^{eff}$	effective Knudsen diffusion coefficient (m²/s)
F_{feed}	volume flow rate of feed gas (ml/min)
ΔH^0_{298K}	enthalpy of reaction (kJ/mol)
K	equilibrium constant
k_{ads}^{eff}	effective adsorption constant (s^{-1})
k_{des}	desorption constant (s^{-1})
k_{diss}^{eff}	effective dissociation constant (s^{-1})
k_{des}	association constant (s^{-1})
L	reactor length (m)
m	catalyst amount (g)
M_n	molar fraction of the C_n product
$\dot{n}_i$	molar flow of gas-phase component (mol/min)
P	total pressure (bar)
PS	pulse size (molecules)
r_p	rate of chain propagation (mol/g$_{cat}$/s)
r_t	rate of chain termination (mol/g$_{cat}$/s)
S	selectivity
S_{BET}	specific surface area (m²/g)
T	temperature (K)
t	time (s)
W_n	weight fraction of the C_n product
X	conversion
α	chain growth probability
θ	Bragg diffraction angle (°)
λ	wavelength (nm)
x_i	molar fraction of product i

1 Introduction

1.1 Carbon dioxide – waste or feedstock?

Increasing emissions of greenhouse gases, such as methane, nitrous oxide, fluorinated gases and mostly (80%) carbon dioxide (CO_2), have become a major concern worldwide during the last few decades. There is a correlation between CO_2 concentration in the atmosphere and the global temperature [1]. Carbon dioxide is considered to be responsible or partly responsible for global warming and to have a negative impact on our environment, causing harmful climate changes leading to natural disasters such as floods, hurricanes, and droughts [2, 3]. The main sources of carbon dioxide are power generation and manufacturing (stationary emission sources: cement production, refineries, iron and steel industry, petrochemical industry, oil and gas processing) [4]. In 2020, the overall CO_2 emission into the atmosphere was 33.5 Gt and this value is expected to rise every year and to increase to 45 Gt in 2040 [5, 6]. The reduction of CO_2 concentration in the atmosphere could help to improve ecological situation, but this would require companies to change their politics, which is impossible without economic stimulus. Apart from reducing CO_2 emissions, this gas can be captured directly from flue gases of industrial processes or from the atmosphere and stored (CCS) [7-9]. But the limit of storage capacity and the absence of production of any intrinsic value make this option unfavorable [10]. Another way to mitigate CO_2 emissions is to consider it as a feedstock rather than a waste. Thus, carbon dioxide could be captured and utilized (CCU). CO_2 utilization processes can be categorized in two main pathways: physical and chemical. First category includes using CO_2 in the production of carbonated drinks, fire extinguishers, dry ice, solvent, process fluid, refrigerant, and welding medium. But these applications need low CO_2 amounts and, therefore, have a low effect on the overall CO_2 emissions [11]. Second category of applications implies using carbon dioxide as a reactant for production of value-added chemicals. However, CO_2 is highly thermodynamically stable and inert compound, ΔG_{298}^{0}=-394.4 kJ/mol. In order to engage it in any chemical process, high reaction temperatures, reducing agents and active catalysts should be applied. There are already industrially realized processes using CO_2 as a reactant (Figure 1.1). The production of urea is the largest production utilizing CO_2 with more than 50% of the overall annual usage of carbon dioxide. Its production is about 100 Mt per year and proceeds into two steps. Carbon dioxide reacts with ammonia forming ammonium carbamate followed by its dehydration to urea, which is used as a fertilizer and for the production of resins [12, 13].
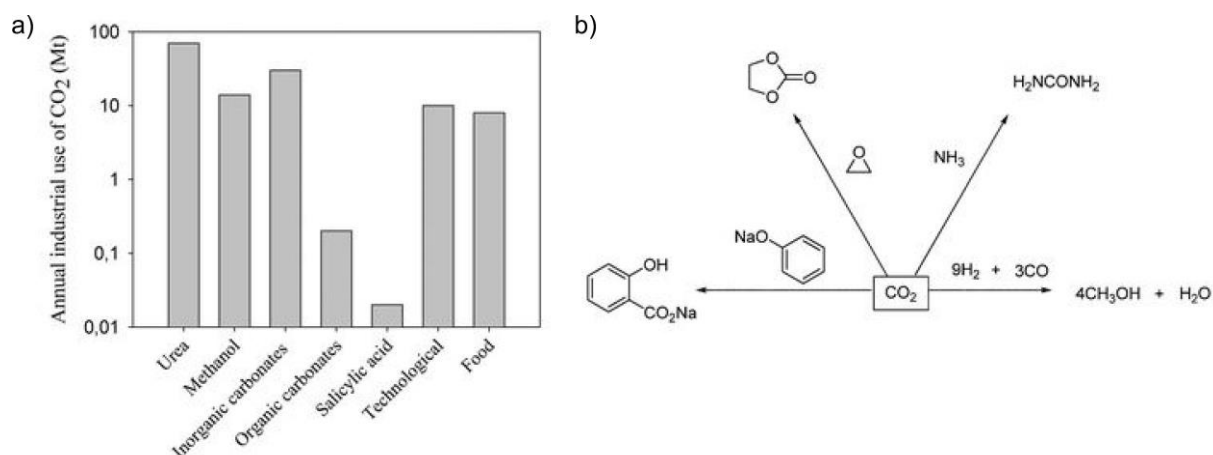
Figure 1.1. (a) The annual industrial use of CO_2 (Mt). Y-axis is in a logarithmic scale. (b) Industrial syntheses using CO_2 as a feedstock [13].

CO_2 is also used for large-scale production of methanol. Around 40 Mt of methanol are produced annually. It should, however, be noted that CO is the main carbon-containing source in the methanol production. CO_2 is co-converted in smaller amounts. Catalysts based on oxides of copper and zinc are usually applied for the methanol synthesis. The direct conversion of CO_2 to methanol is being under the investigation for decades and will be highlighted below. Methanol is an important compound and used as an intermediate for the production of a variety of chemicals such as dimethyl ether (DME), formaldehyde, methyl tret-butyl ether (MTBE) and acetic acid [14, 15].

Carbon dioxide can be homogeneously and without any hydrogenation transformed into carboxylates, esters, carbamates or organic/inorganic carbonates. Generally, there are two routes: a) reaction of CO_2 with unsaturated hydrocarbons, or b) insertion of CO_2 into metal-element (C, H or O) bonds followed by subsequent transformations into different products [16]. The most important industrialized (since the 1950s) process in this regard is ethylene carbonate production through CO_2 reaction with ethylene oxide (Figure 1.1b). Cyclic organic carbonates have a high boiling point and therefore ethylene carbonate is often used as a solvent for natural and synthetic polymers including nylon, lignin, cellulose ester, and polyvinyl chloride (PVC). Organic carbonates can be also used as an intermediate for polymers and polycarbonates production [13, 17, 18]. Another important process utilizing CO_2 is carboxylic acids production. Potassium or sodium phenol salts react with CO_2 under pressure (5-7 bar) to yield salts of carboxylic acids. The latter can be recovered through acidification with H_2SO_4. One of the most important products is salicylic acid, which is already industrially produced for almost 150 years. It is used as an intermediate for acetylsalicylic acid (aspirin) production [13, 18].

The industrial processes utilize currently only 0.5% of the total anthropogenic CO_2 emissions [13]. Therefore, development and investigation of technologies for CO_2 conversion are required to mitigate the negative impact of this greenhouse gas on our environment and to provide an additional sustainable carbon source. A promising way is thermocatalytic CO_2 hydrogenation to value-added chemicals. The reduction of CO_2 with H_2 produced on CO_2-free basis is a very attractive approach to mitigate CO_2 emissions and to obtain alcohols, oxygenates, paraffins, olefins or aromatics and other valuable compounds.

1.2 CO₂ hydrogenation to methanol and related transformations

CO_2 hydrogenation to methanol is one of the processes of great importance for controlling CO_2 emissions and producing building blocks for the chemical industry. Methanol synthesis from CO_2 (equation 1.1) is being under investigations for decades and has been successfully commercialized. The first plant using patented Lurgi MegaMethanol® process of CO_2 hydrogenation to methanol was founded in 2004 [19]. Since then, this technology was introduced in 19 more plants. Carbon Recycling International (CRI) company has founded in 2011 their first plant of methanol production from CO_2, which is situated in Iceland [20]. Its production capacity was scaled from 1.3 to 4 kt per year within the four first years. The company is opening new plants and increasing the methanol production worldwide every year. However, no more or less detailed information about the type of the catalyst or reactor is available.

$$CO_2 + 3H_2 \rightleftarrows CH_3OH + H_2O, \ \Delta H^0_{298K} = -49.3 \text{ kJ/mol} \tag{1.1}$$
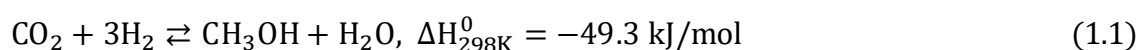
According to the literature, the most active and selective catalysts are based on Cu as the main active component and ZnO as the supporting material [8, 21]. ZrO_2, Al_2O_3, In_2O_3, SiO_2, Ga_2O_3 or La_2O_3 are the most excessively studied promoters reported to enhance catalyst activity and product selectivity [22, 23]. It is assumed that oxygen vacancies in their structure are active sites for CO_2 activation and hydrogenation [24, 25]. From a mechanistic viewpoint, CO_2 hydrogenation to methanol can proceed through two alternative pathways (Figure 1.2). The process starts with non-dissociative adsorption of CO_2 and dissociative adsorption of H_2. The adsorbed CO_2 species can be hydrogenated to hydrocarboxyl (COOH) or formate (HCOO) species, which stand for the key difference between the two mechanisms. These species are subsequently transformed into HCOH or H_2CO species and finally into CH_3OH.

CO_2 hydrogenation to methanol is an exothermic reaction (equation 1.1) [26]. The RWGS reaction occurs in parallel as a side reaction and is favored at higher temperatures due to its

endothermic nature (equation 1.2). Therefore, CO_2 hydrogenation to methanol is usually conducted at lower temperatures to avoid the formation of CO through the RWGS reaction. An optimal temperature for CO_2 to methanol conversion is 300-325 °C [25]. However, as catalysts applied for CO_2 hydrogenation to methanol can also catalyze CO conversion to methanol, CO formed as a by-product is also hydrogenated through a similar to formate route. But it should be emphasized that when comparing CO_2 and CO-based processes over the same catalyst, the former one is reported to be less effective in terms of productivity. The reason is the negative effect of H_2O, which is formed in higher amounts during CO_2 hydrogenation [19].

$$CO_2 + H_2 \rightleftarrows CO + H_2O, \ \Delta H_{298K}^0 = 42.1 \text{ kJ/mol} \tag{1.2}$$
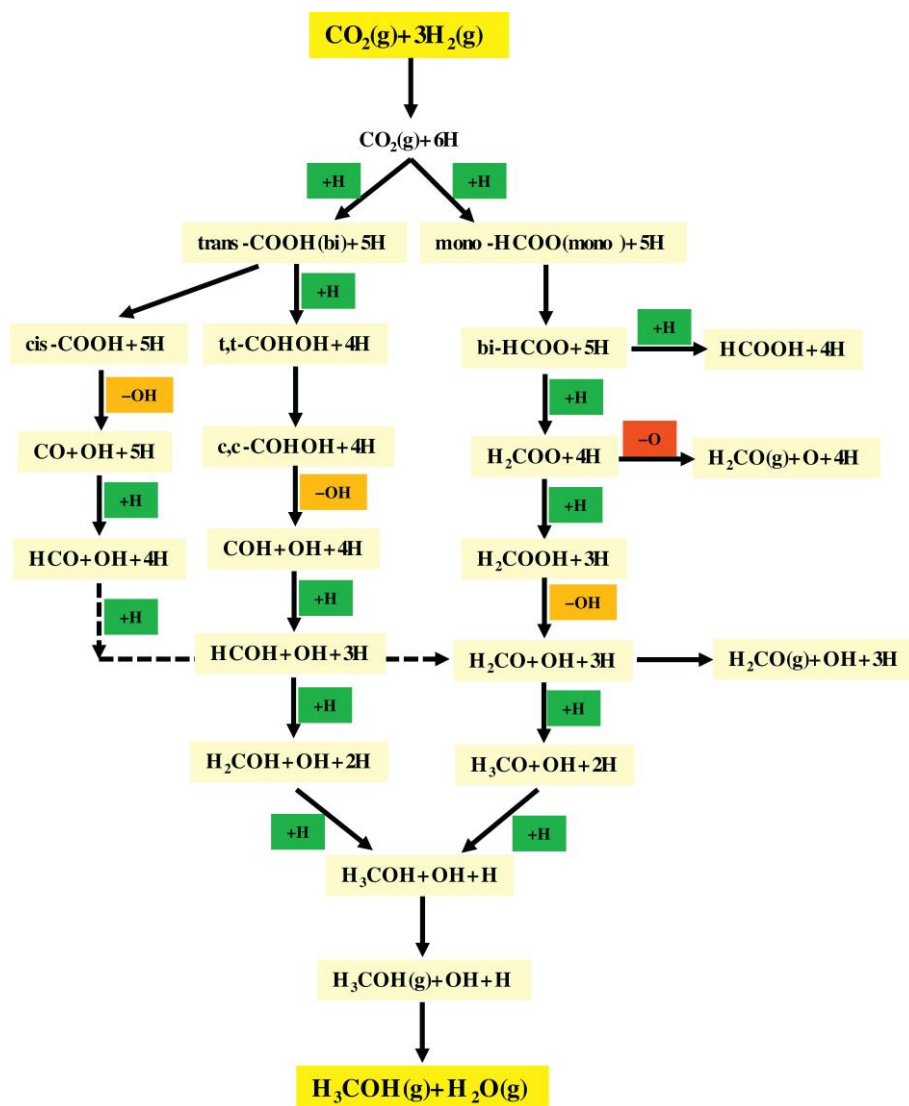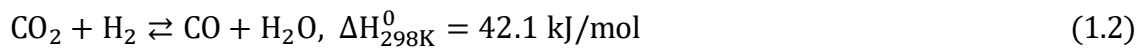
Figure 1.2.   A scheme of CO_2 hydrogenation to methanol on the surface of metallic Cu [21].

When discussing the CO_2 hydrogenation to methanol process, it should be also mentioned that methanol could be further converted to hydrocarbons *via* methanol to olefins (MTO) process

4

(Figure 1.3). This includes alkanes, alkenes and aromatics. Alkenes, which are usually divided into lower (light) olefins (C_2-C_4) and higher olefins (C_{5+}), are of the most interest. Higher olefins are important for industrial production of surfactants, PVC plasticizers, detergents and synthetic lube oils [27]. Lower olefins are important building blocks for plastics, rubbers, solvents and synthetic textiles production [28]. Ethylene, propylene and 1,3-butadiene have the highest value. Ethylene is mostly used for the plastic production, such as polyethylene (PE), polyethylene terephthalate (PET), polystyrene (PS) and PVC. It is also used in production of chemical intermediates, such as ethylene dichloride, ethyl benzene and ethylene oxide [29]. Propylene is mostly used for the production of polypropylene (PP), but also for propylene oxide and cumene production [28, 29]. 1,3-butadiene is mostly used for the production of synthetic rubber: styrene butadiene rubber (SBR), polybutadiene rubber, nitrile butadiene rubber (NBR) and etc. It is also applied in the production of adiponitrile and acrylonitrile-butadiene-styrene [28, 30]. The demand for these chemicals is rising every year. That is why CO_2 hydrogenation to hydrocarbons is a promising way to close this gap.

Methanol-mediated hydrocarbons synthesis

$$CO_2 + H_2 \xrightarrow{\text{Methanol synthesis}} CH_3OH + H_2O \xrightarrow{\text{Methanol to olefins}} C_xH_y + H_2O$$
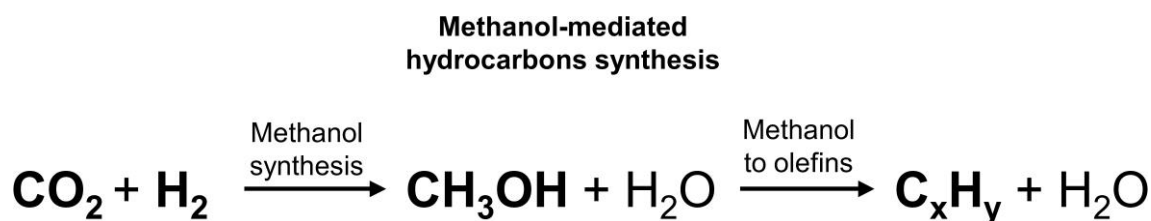
Figure 1.3.   Pathways of hydrocarbon production through methanol-mediated synthesis.

As the methanol-mediated synthesis comprises two consecutive steps: methanol synthesis and its conversion into hydrocarbons through MTO reactions (equations 1.1, 1.3-1.5), a two-stage reactor (indirect route) with the catalysts suited for each step could be used. An advantage of such operation is that each reactor could be run under specific optimized reaction conditions. However, as two steps are not mutually exclusive, a single-reactor operation (direct route) is possible and even preferable, because it is more economical and energy-efficient. This is crucial for the process commercialization [31]. For this reason, many researchers are focused on the investigation of the direct route. Therefore, the catalysts applied for CO_2 hydrogenation through methanol-mediated synthesis should be active in both mentioned reactions. As was mentioned above, metal oxides are usually employed to catalyze the first step (methanol synthesis). Solid acid catalysts are used for the conversion of methanol to the desired hydrocarbons [32, 33]. ZSM-5 and SAPO-34 are usually applied in the MTO step. Acidic sites of zeolites are suggested to be responsible for the chemical conversion of methanol into hydrocarbons [32, 34].

Therefore, a physical mixture of metal oxides or mixed-metal oxides and zeolites is often applied for methanol-mediated hydrocarbons synthesis.

$$2CH_3OH \rightleftarrows C_2H_4 + 2H_2O, \ \Delta H^0_{298K} = -29.3 \ kJ/mol \qquad (1.3)$$

$$3CH_3OH \rightleftarrows C_3H_6 + 3H_2O, \ \Delta H^0_{298K} = -102.3 \ kJ/mol \qquad (1.4)$$

$$nCH_3OH \rightleftarrows C_nH_{2n} + nH_2O, \ \Delta H^0_{298K} < 0 \qquad (1.5)$$
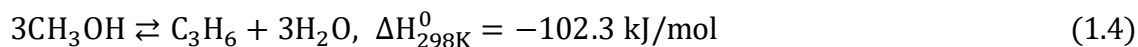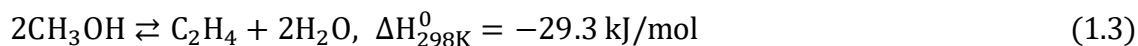
While the mechanism of CO_2 hydrogenation to methanol is well studied and was already highlighted above (Figure 1.2), there is much less understanding about the MTO reactions mechanism. It is reported that methanol conversion rate during the MTO reaction is very low at the initial period of time but increases drastically after the induction period. It is assumed that olefins formed during this induction period are then taking part in the reaction and enhancing the rate of methanol conversion. That indicates that the MTO reaction is an autocatalytic process. The pool mechanism was suggested to describe the reaction pathways (Figure 1.4). Methanol forms first a pool of active hydrocarbon species inside the pores of zeolite catalysts. Then methanol reacts with such species to yield light olefins, which are further transformed through condensation, cyclization, alkylation and hydrogen transfer reactions into alkanes, higher olefins, and aromatic hydrocarbons [35, 36]. The product selectivity is usually tuned by the zeolite pore architecture. Small pores prevent the formation of heavy and/or branched hydrocarbons in favor of lower linear olefins [37]. However, the exact pathway of product formation is not yet established.
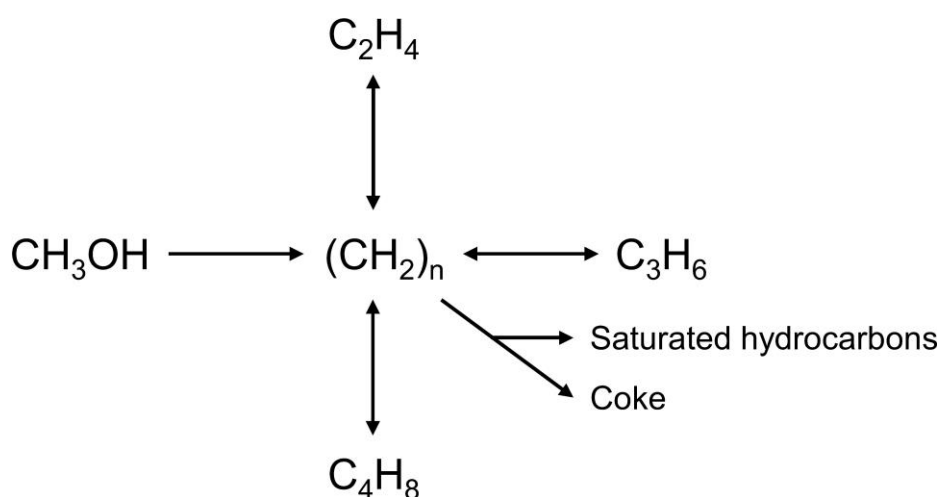
Figure 1.4.   A carbon-pool mechanism for the conversion of methanol to hydrocarbons [38].

As was stated above, an optimal temperature for CO_2 hydrogenation to methanol is 300-325 °C [25]. But the MTO reaction requires higher temperatures. For instance, 400-450 °C was reported to be the optimal temperature for this reaction over SAPO-34. These temperatures are, however, too elevated for the selective hydrogenation of CO_2 to methanol [39]. A compromise in the reaction conditions should always be found for an optimal combination of both processes. Because of above mentioned limitations, the best-performing catalysts showed the conversion of CO_2 on the level of only 13% with 47% CO selectivity. However, it should be mentioned, that among all hydrocarbons produced the lower olefins fraction was 80% [26]. Therefore, the methanol-mediated pathway of CO_2 hydrogenation to hydrocarbons is potentially a very promising way of CO_2 utilization, if selectivity to CO could be further suppressed.

1.3 CO₂ Fischer-Tropsch synthesis

Another possibility to convert CO_2 into higher hydrocarbons (C_{2+}-hydrocarbons) is modified Fischer-Tropsch synthesis (MFTS) as well known as CO_2 Fischer-Tropsch synthesis (CO_2-FTS). It is distinguished from the methanol-mediated synthesis by its intermediate. In CO_2-FTS carbon dioxide is first reduced to CO through the reverse water gas shift (RWGS) reaction followed by the chain propagation through the classical CO Fischer-Tropsch synthesis (CO-FTS) (Figure 1.5) [29, 40, 41].

Modified Fischer-Tropsch synthesis

$$CO_2 + H_2 \xrightarrow[\text{reaction}]{\substack{\text{Reverse Water} \\ \text{Gas Shift}}} CO + H_2O \xrightarrow[\text{synthesis}]{\text{Fischer-Tropsch}} C_xH_y + H_2O$$
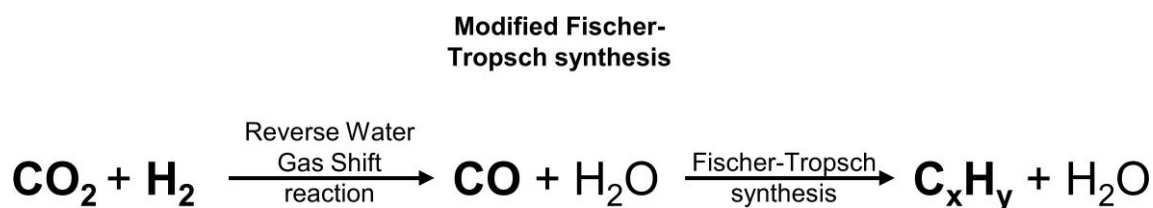
Figure 1.5   A pathway of hydrocarbon production through modified Fisher-Tropsch synthesis.

1.3.1 Thermodynamic aspects of CO₂-FTS

As was mentioned above, the RWGS reaction is an endothermic process (equation 1.2) and requires high temperatures to reach high degrees of CO_2 conversion, while the CO-FTS is an exothermic reaction (equations 1.6-1.8). Thus, the conversion and product distribution are directly affected by the reaction temperature as well as pressure and H_2/CO_2 feed ratio (equations 1.9-1.10). Therefore, like in the case of the methanol-mediated pathway of hydrocarbons formation, a compromise in the reaction temperature is required to efficiently convert CO_2 into the desired products. The CO_2 conversion through the RWGS step is

thermodynamically limited. It is between 23 and 30% at typically applied reaction temperatures (300 – 400 °C) for CO_2-FTS. However, the consecutive CO hydrogenation steps, which are limited kinetically, usually shift the equilibrium of CO_2 conversion towards higher levels. Yao et al. [42] analyzed the thermodynamics of CO_2-FTS considering only the formation of olefins as hydrocarbon representatives. These compounds are regarded as primary products in the CO hydrogenation reaction.

$$2CO + 4H_2 \rightleftarrows C_2H_4 + 2H_2O, \ \Delta H^0_{298K} = -210.32 \text{kJ/mol} \tag{1.6}$$

$$3CO + 6H_2 \rightleftarrows C_3H_6 + 3H_2O, \ \Delta H^0_{298K} = -373.6 \text{ kJ/mol} \tag{1.7}$$

$$nCO + 2nH_2 \rightleftarrows C_nH_{2n} + nH_2O, \ \Delta H^0_{298K} < 0 \tag{1.8}$$
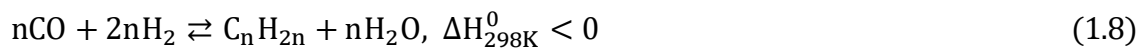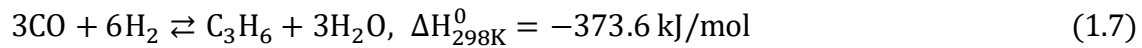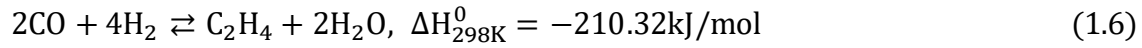
$$K = \exp{(-\frac{4577.8}{T} + 4.33)} \tag{1.9}$$

$$K = \frac{X^2}{(n-X)(1-X)} \tag{1.10}$$

where K is equilibrium constant, X is conversion of CO_2 and n stands for the H_2:CO_2 ratio.

Yao et al. [42] found that the equilibrium conversion of CO_2 decreases with an increase in the temperature in the range of 100 – 450 °C and increases with an increase in the temperature in the range of 450 – 1000 °C. The reason is that the CO-FTS reaction is favored at lower temperatures and all CO formed through the RWGS reaction is converted into olefins. Thus, the equilibrium of the RWGS reaction shifts to the right side resulting in a high CO_2 conversion and low CO selectivity. This selectivity is very low below 400 °C but increases rapidly with a further increase in the temperature. The selectivity to olefins follows an opposite trend. It is almost 100% below 400 °C and decreases sharply with rising temperature [42]. An optimal temperature for the synthesis of lower olefins (C_2-C_6) is between 300 and 400 °C while the formation of higher olefins (C_{7+}) is favored below 300 °C [43]. An increase in the reaction pressure has a positive effect both on the CO_2 conversion and the selectivity to lower as well as higher olefins. The selectivity to olefins, however, grows slightly after a sharp increase in the range of 0.1 – 3 bar. The ratio of H_2/CO_2 also affects catalytic performance. For example, CO_2 conversion increases significantly with an increase in the molar ratio of H_2/CO_2 from 0.1 to 3. Further increase in the molar ratio has almost no effect on the conversion of CO_2 [44]. The selectivity to olefins is almost not affected when the H_2/CO_2 ratio increases above 1 [42]. However, it should be noted, that when considering the formation of all hydrocarbons, using a feed with the H_2/CO_2 molar ratio higher than 3 leads to a significant production of methane and

paraffins [45]. The H_2/CO_2 ratio of 3 – 4 is reported to be optimal for the high level of CO_2 conversion and olefins production. Thus, reaction conditions beneficial for the production of lower olefins at high degrees of CO_2 conversion are medium reaction temperature (300 - 400 °C), high reaction pressure ($\geq$ 3 bar) and high H_2/CO_2 molar ratio (3 - 4). These theoretical finding were supported by practical works of multiple researchers [46-48].

1.3.2   *Product distribution in CO$_2$(CO)-FTS*

The Anderson-Schulz-Flory (ASF) theory was developed to describe the product distribution in CO-FTS [49]. It provides the relationship between the selectivity and the chain growth probability (equation 1.11). The latter is represented by the α factor, which reflects the probability that a CO molecule will react to extend the hydrocarbon chain. α factor is determined by the rates of chain propagation and termination (equation 1.12). It is assumed that the chain growth probability does not depend on the number of carbon atoms in a hydrocarbon, but it could be influenced by different factors such as process conditions, type of catalyst and chemical promoters [50]. The typical ranges of α over Ru-, Co-, and Fe-based catalysts in CO-FTS are 0.85–0.95, 0.70–0.80, and 0.50–0.70, respectively [51]. More common expressions for the product selectivity and α are given by equation 1.13. It is usually applied in the logarithmic form because the chain growth probability could be easily estimated as the slope tangent from the linear dependence of $\ln \left(\frac{W_n}{n}\right)$ from n (equation 1.14).

$$M_n = (1 - \alpha)\alpha^{n-1} \tag{1.11}$$

$$\alpha = \frac{r_p}{r_p + r_t} \tag{1.12}$$

$$W_n = n(1 - \alpha)^2\alpha^{n-1} \tag{1.13}$$

$$\ln \left(\frac{W_n}{n}\right) = n\ln\alpha + \ln \frac{(1-\alpha)^2}{\alpha} \tag{1.14}$$

where M_n is the molar fraction of the C_n product, α is the chain growth probability, n is the number of carbon atoms in a hydrocarbon (n $\geq$ 1), r_p is the rate of chain propagation, r_t is the rate of chain termination and W_n is the weight fraction of the C_n product.

Figure 1.6 shows the selectivity to hydrocarbons as a function of the α parameter. It could be seen that according to the ASF model the lower the chain growth probability, the higher selectivity to methane is. The maximal selectivity to C_2-C_4 hydrocarbons reaches 58% with an α value between 0.4 and 0.5 [52]. This feature was long considered as a major restriction for

the industrial application of the CO-FTS [53]. However, significant deviations from the ASF distribution have been reported in the literature [54]. One of such deviations is relatively high selectivity to methane. Several explanations have been proposed to describe the observed feature. Wojciechowski [55] modeled the distribution of hydrocarbons using different termination probabilities. Thus, the excess of methane formation was described with a separate parameter having an increased termination probability of C_1 precursor. The termination probability of methane was reported to be 5 - 20 times larger than the termination probability of other hydrocarbons [56].
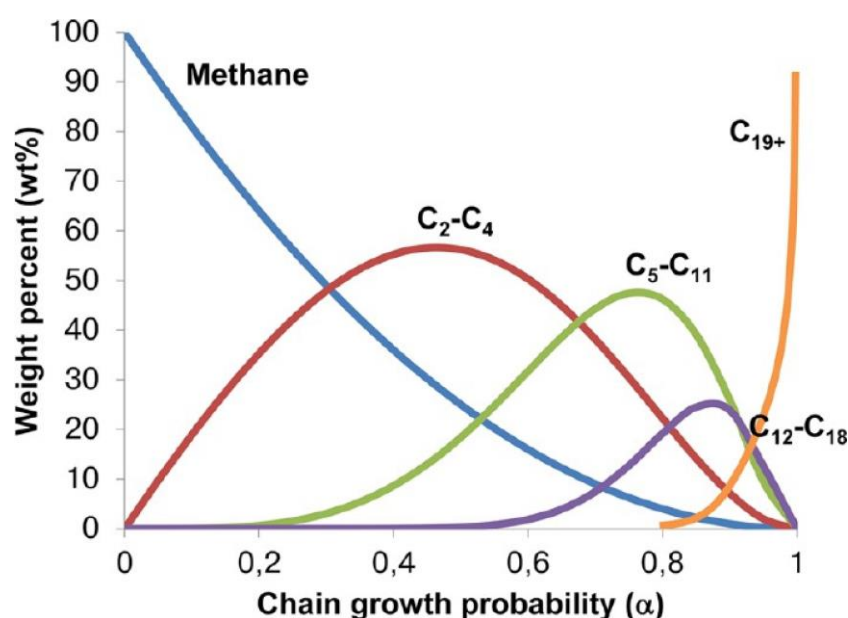
Figure 1.6. Selectivity dependence on the chain growth probability parameter according to Anderson-Schulz-Flory model [28].

Another possible reason for high methane formation is mass- and heat-transfer limitations [51]. The mass-transfer limitations would result in an increase in the formation of thermodynamically favored product - methane. The heat-transfer limitations could lead to the appearance of hot spots because of reaction exothermicity, which may result in a decrease in the chain growth probability factor and a higher formation of methane [57]. Third explanation is possible secondary hydrogenolysis reactions of higher hydrocarbons (equation 1.15) [58]. It should be noted that the hydrogenolysis is strongly hindered with increasing CO and H_2O pressures [59]. Thus, the hydrogenolysis could participate in methane formation, but it is unlikely that it is alone responsible for high methane yield. One more assumption for this ASF deviation is a different catalytic site for the methanation reaction [60]. It is supported by some other studies, where the negative deviation of the ASF model for methane yield was observed [61, 62]. It is

assumed that catalysts possess different active sites responsible for C-C coupling reactions and for methane formation. It is reported that these sites could be modified independently by addition of promoters such as sulfur [63]. However, the exact nature of these sites is not specified. Therefore, it is problematic to point out a single process accountable for the deviations in methane production from the ASF model under all circumstances.

$$C_nH_{2n+1}^* + H^* \rightleftarrows C_{n-1}H_{2n-1}^* + CH_3^* \qquad\qquad (1.15)$$

Another disagreement of the experimentally obtained data from the ASF model prediction is anomalistic low production of ethane and especially ethene. Wojciechowski [55] suggested a higher reactivity of C_2 products in comparison with other higher hydrocarbons. A higher chain propagation rate would lead to a lower yield of ethane and ethene. Another possible explanation is the presence of secondary reactions. One of the possible secondary reactions is the incorporation of ethene into growing chains [64]. Adsorbed ethene may act as the chain growth initiator or be converted into methylene monomer, which participates in chain growth reactions. This reaction would have an effect on the distribution of C_2 and longer-chain hydrocarbons [65]. Iglesia et al. [59] found that ethene and propene have not only a higher reactivity in comparison with other olefins but also a higher adsorption constant. The strong adsorption of formed ethene would lead to a decrease in its yield and an increase in the production of ethane and higher hydrocarbons through ethene secondary hydrogenation. As it was mentioned above, the hydrogenolysis of ethane and ethene to methyl (equation 1.15) could also contribute to lower C_2-hydrocarbons yield [66].

One more deviation from the ASF distribution model is the change of chain growth probability factor for long-chained hydrocarbons. At a carbon number of about 10, α value is reported to increase with an increase in a number of carbon atoms in a hydrocarbon [57]. An explanation of this effect is the inhibited diffusion and enhanced adsorption of heavy hydrocarbons. Longer residence times facilitate secondary hydrogenation and chain prolongation. As a result, accumulation of long-chained hydrocarbons is observed. The increased concentration is followed from internal diffusion limitation [67]. Therefore, it should be kept in mind that the ASF model is deficient and useful only as an approximation.

1.3.3 Mechanistic aspects of CO₂-FTS

It is generally accepted that CO_2 is initially reduced to CO through the RWGS reaction. The formed CO is then hydrogenated to hydrocarbons. Two mechanisms are proposed to describe

the RWGS reaction: i) the redox mechanism, and ii) the associative mechanism (Figure 1.7). In the redox mechanism, dissociative adsorption of CO_2 occurs on an active site, which leads to the oxidation of the latter and the formation of adsorbed CO species. CO then desorbs from the surface. The active site is reduced back with the help of H_2 yielding the water [68]. In the associative mechanism, CO_2 adsorbs non-dissociative on an active site. H_2 adsorbs and dissociate on another active site and reacts with adsorbed CO_2 with the formation of a surface intermediate. It is accepted that the surface intermediate is formate, however, carbonate, carbonyl and carboxylate species were also considered [69]. The intermediate dissociates and desorbs as CO and water. In both mechanisms oxygen vacancies of the active site are believed to play an important role for CO_2 adsorption [6]. The adsorption of CO_2 with or without the dissociation refills the oxygen vacancy on the surface of the catalyst and CO desorbs.

Redox pathway	Associative pathway
1) CO_2 (g) + s $\rightleftarrows$ $CO_2 \cdot$s	**1)** H_2 (g) + s $\rightleftarrows$ $H_2 \cdot$s
2) $CO_2 \cdot$s + s $\rightleftarrows$ $CO \cdot$s + $O \cdot$s	**2)** $H_2 \cdot$s + s $\rightleftarrows$ $H \cdot$s + $H \cdot$s
3) $CO \cdot$s $\rightleftarrows$ CO (g) + s	**3)** CO_2 (g) + s $\rightleftarrows$ $CO_2 \cdot$s
4) H_2 (g) + $O \cdot$s $\rightleftarrows$ $H_2O \cdot$s	**4)** $H \cdot$s + $CO_2 \cdot$s $\rightleftarrows$ $COOH \cdot$s + s
5) $H_2O \cdot$s $\rightleftarrows$ H_2O (g) + s	**5)** $COOH \cdot$s + $H \cdot$s $\rightleftarrows$ CO (g) + H_2O (g) + 2s
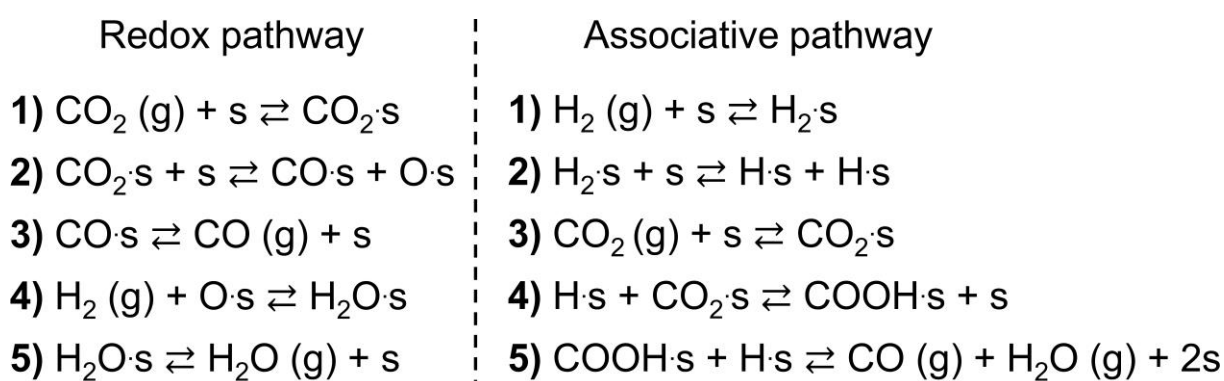
Figure 1.7. Redox and associative pathways of the RWGS reaction on the surface (s) of a catalyst [70].

There are several mechanisms proposed for CO hydrogenation reactions [71]. The generally accepted mechanism describing the formation of hydrocarbons is the so-called carbide mechanism [54]. The building block in the carbide mechanism is considered to be a methylene (CH_2) group. The first step is the dissociative adsorption of CO and H_2 (Figure 1.8). CH, CH_2, and CH_3 species are formed through the interaction of adsorbed C and H atoms. The insertion of CH_2 into a growing alkyl chain is the elementary step of chain propagation reactions. According to the mechanism, olefins are formed when the process is terminated by dehydrogenation. On the other hand, if the chain propagation reaction is terminated by addition of H_2 or CH_3 paraffins are produced.
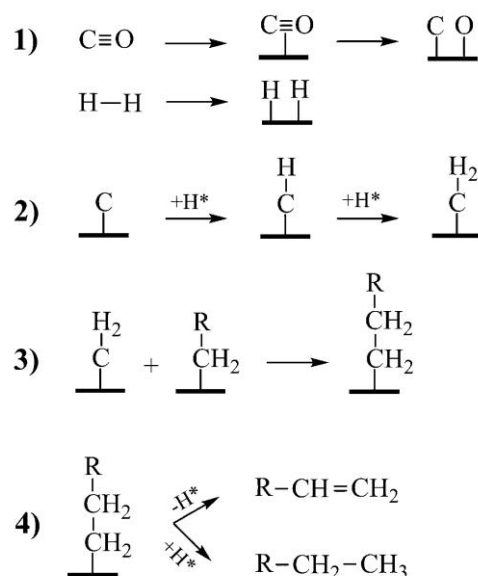
Figure 1.8. The carbide mechanism of the CO-FTS on the surface of Fe-based catalyst [54].

1.3.4 *Iron-based catalysts and their structural changes under CO$_2$-FTS conditions*

A CO$_2$-FTS catalyst should be able to catalyze both the RWGS and CO-FTS reactions under the same conditions. Unfortunately, Co-based catalysts – a well-known materials for CO-FTS – produce mainly methane in CO$_2$-FTS due to its low activity in the RWGS reaction. Cu containing catalysts, on the other hand, usually applied for the RWGS reaction are inefficient in CO$_2$-FTS. As Fe-based catalysts show reasonable activity for both the RWGS and CO-FTS reactions, they are typically applied for CO$_2$-FTS [9, 52]. Their additional advantages are low cost, non-toxicity, reasonable CO$_2$ conversion levels and selectivity to higher hydrocarbons, especially target products – lower olefins [29, 72]. Although it is not rare that iron-based catalysts are promoted with moderate amounts (up to 17 wt%) of Co or Cu to facilitate the CO$_2$ conversion [73, 74].

Fe-based catalysts undergo structural changes under CO$_2$-FTS conditions and are transformed mainly into Fe$_3$O$_4$ and iron carbides. These *in situ* transformations and, correspondingly, the resulting catalytic performance depend on many factors, such as catalyst initial composition, its microstructure, preparation method, presence of support or/and promoter(s), pretreatment and reaction conditions as reported in many studies dealing with CO$_2$-FTS [75-80]. Fe$_3$O$_4$ is regarded to be an active phase for the RWGS reaction, while iron carbides are responsible for the formation of higher hydrocarbons [81-83]. Different iron carbides such as Fe$_2$C, Fe$_{2.2}$C, Fe$_7$C$_3$, Fe$_5$C$_2$ and Fe$_3$C are reported to be formed under CO$_2$-FTS conditions [84]. All of them were proved to be active, with Fe$_7$C$_3$ and Fe$_3$C possessing the highest and the lowest activity,

respectively [85]. The thermal stability of iron carbides increases with a decrease in carbon fraction: $Fe_2C < Fe_{2.2}C < Fe_7C_3 < Fe_5C_2 < Fe_3C$. The Fe_2C and $Fe_{2.2}C$ carbides are formed at low temperatures and converted into Fe_5C_2 above 250 °C. Hägg´s carbide (Fe_5C_2) is stable in the temperature range from 250 to 350 °C and transformed into Fe_3C above 350 °C [86]. The rate of such phase transformations depends on the size of crystallites and the kind of impurities/promoters. The phase composition of iron carbides, their content and microstructure (particle size) have a significant influence on the catalytic activity and product selectivity in CO-FTS [87]. In the range of typically applied reaction temperatures for CO_2-FTS (300 – 400 °C) Fe_5C_2 is the main active and predominant iron carbide phase. Its activity increases with a decrease in the particle size. It was suggested that there is an optimal particle size which leads to a high activity in CO-FTS and moderate selectivity to lower olefins [84, 88]. However, the decrease in the particle size also leads to an increase in methane selectivity. *It should nevertheless be emphasized that the role of iron carbides in CO/CO_2-FTS, including their formation and the influence of their parameters on the reaction is still a matter of debates despite a great number of studies in this field.*

To moderate the product distribution and enhance the activity of Fe-based catalysts, promoters are usually introduced. Many alkali, alkali-earth and transition metals have been studied for CO_2-FTS application. For example, Ce promotion of iron catalyst was shown not to modify the degree of CO_2 conversion or selectivity to target products, but to shorten the time required to reach steady-state operation [89, 90]. Cu and Co are employed to facilitate CO_2 conversion [48, 91, 92]. The addition of Mn is reported to inhibit the methane formation and to enhance olefin/paraffin ratio. Mn acts as a structural promoter, increases catalyst basicity, iron oxide reducibility and accordingly enhances the formation of iron carbides [93, 94]. Among all the dopants, alkali metals have the most significant positive effect on the degree of CO_2 conversion, the selectivity to C_{2+}-hydrocarbons as well as the olefin/paraffin ratio [95-99]. They are known to increase the production of long-chained and olefinic hydrocarbons in CO_2-FTS. Different mechanisms were put forward to explain their promotional effect: (i) site blocking effect (promoter adsorbs on an active site complicating the adsorption of reagents), (ii) metal electronic interactions (promoter donates electronic density to Fe and increases its basicity), (iii) direct chemical interaction (promoter interacts with a catalyst forming a new phase), (iv) alkali-induced surface reconstructions (promoter causes catalyst surface reconstruction) [48, 90, 98]. Li has the least pronounced effect [98, 100]. Na as well as K are the commonly utilized dopants. Their introduction hinders the formation of methane, shifts the products distribution to higher molecular weight hydrocarbons and positively influences the olefin production [77,

101-103]. The strength of promotional effect of Na is reported to be lower than that of K as well as of Rb and Cs in terms of light olefin production and suppressing methane formation [98]. Although catalytic performance of iron oxides promoted with K, Rb or Cs is similar, several researchers reported that Rb has the highest CO_2 hydrogenation activity and olefin/paraffin ratio within C_2-C_4 hydrocarbons [97, 98]. *However, it should be mentioned that the reported information is often controversial, and several fundamental questions still remain unclear. For example, does the presence of the promoter has an effect on the in situ formation of iron carbides, and if yes, to what extent? Is there an optimal content of the promoter or the more the merrier?*

Another topic of controversial debates is the influence of the crystallite size of catalytically active phases or their precursor on product selectivity and CO_2 conversion. Thus, some authors established an increasing tendency both for CO_2 conversion and the selectivity to methane and C_{2+}-hydrocarbons with an increase in the particle size of Fe_2O_3 in fresh supported catalyst [78]. They explain the observed effect through a higher number of terrace sites on larger particles, which endorse the adsorption of CO participating in chain-growth reaction. Other researchers also reported an increase in the conversion of CO_2 and the selectivity to C_{2+}-hydrocarbons but a decrease in the selectivity to methane with an increase in the particle size of Fe_2O_3 in fresh supported catalyst. The particle size was tuned through the variation of the size of support pores [104, 105]. However, the explanation for the observed effects given by the authors differs. Numpilai et al. [104] concluded that larger pores enhance the formation of more molecular weight hydrocarbons and favor olefin/paraffin ratio owing to the improvement of the product diffusion, that hinders the secondary hydrogenation of olefins to paraffins. While Xie et al. [105] stated that pore size itself is inadequate to describe the difference in hydrocarbons selectivity. They put forward that the influence of the particle size on the reducibility of FeO_x is an important parameter for *in situ* formation of active Fe_xC_y species under CO_2-FTS conditions. *Therefore, despite the fact that many researchers agree on the importance of the particle size of catalytically active phase or its precursor, there is no uniform explanation of the observed effects, which are as well quite controversial.*

Q. Yang et al. [73] recently performed a statistical analysis of available literature data about CO_2-FTS, where they identified descriptors for efficient CO_2 hydrogenation to higher hydrocarbons. Along with the reaction conditions such as total pressure, reaction temperature, and catalyst pretreatment as well as the presence of various promoters, the kind of iron precursor and the preparation method of iron oxides were assumed as the most decisive parameters

affecting the C_{2+}-hydrocarbons selectivity and the olefin/paraffin ratio. Albrecht et al. [75] showed that unpromoted bulk catalysts prepared through precipitation and template-assisted synthesis demonstrated different catalytic performance with the later yielding an unexpectedly efficient catalyst. *While the effects of dopants and reaction conditions have been investigated for many years, much less attention was paid to studying the effects of iron oxide precursor and composition of fresh (as-prepared) catalyst on reaction-induced restructuring and accordingly catalyst activity and product selectivity in CO$_2$-FTS.*

2 Objectives and strategy of this thesis

2.1 Objectives

As demonstrated above in the literature review, there are many challenges to overcome in the CO_2 hydrogenation to higher hydrocarbons from an applicational viewpoint. In addition, many fundamental questions are still open to ensure tailored catalyst design and synthesis. The most key aspects are the understanding of the formation of iron carbides and their physico-chemical properties (adsorption properties, oxidizability, reactivity) to establish the most decisive parameters determining catalyst activity and product distribution. Fe-based compositions can be purposefully created upon catalyst preparation or pretreatment before the reaction. The presence of a support and/or promoter in a catalyst complicates the understanding of the effects of steady-state composition because the above-mentioned catalyst components can also directly or indirectly participate in the activation of feed components and product formation. Therefore, the studying of well-defined $Fe_xO_yC_z$ compositions without any support and/or promoter in CO_2-FTS could put light on the reaction-induced phase restructuring and help to obtain structure-activity-selectivity relationships. The investigation of undoped bulk materials would allow an unambiguous identification of iron oxide/carbide descriptors affecting catalyst activity and product selectivity. Having such descriptors, the effect of promoters on *in situ* formed steady-state catalyst composition and performance could be more reasonably investigated. Such knowledge would allow the tailored design of catalysts with desired performance.

Therefore, the main goal of the present work is to establish the relationships between the phase composition, microstructure and physico-chemical properties of different iron oxides, their reaction-induced transformations into steady-state phases and the consequences for CO_2 hydrogenation to higher hydrocarbons. To successfully reach this goal, the following specific objectives were set:

i. To investigate the influence of the preparation method and synthesis parameters of iron oxides on their microstructure, phase composition and crystallite size through the preparation of well-defined catalyst compositions and their thorough characterization.

ii. To investigate the evolution of the microstructure and the phase composition of as-prepared iron oxides during reductive/oxidative treatments and under CO_2-FTS conditions. It was achieved by analyzing the kinetics of as-prepared catalyst reduction

or oxidation with H_2 or CO_2, conducting CO_2-FTS experiments and determining the steady-state composition as well as its spatial distribution along the catalyst bed.

iii. To identify descriptors of iron oxides/carbides relevant for efficient CO_2 hydrogenation to higher hydrocarbons and the possibilities to control them during the design and the preparation of catalysts. It was possible owing to the analysis of the physico-chemical properties of steady-state catalyst composition including the mechanistic analysis of product formation and spatially resolved and transient kinetic analysis.

iv. To investigate the effect(s) of alkali metal dopants including the amount and the nature of promoter on the catalytic performance and the pathways of product formation. It was achieved through the spatially resolved product formation reaction rates analysis.

2.2 Strategy and outline

The strategy for achieving the above stated objectives is described below. All catalysts were prepared using iron (II) oxalate dihydrate as precursor for different Fe-containing phases (Figure 2.1). In **Section 4.1**, a number of catalysts consisting of Fe_3O_4, FeO, Fe and Fe_xC_y were prepared. The idea was to understand how different iron compounds are restructured under CO_2-FTS conditions. The as-prepared and spent (after about 95 h on CO_2-FTS stream) catalysts were thoroughly characterized by complementary methods. Several catalytic experiments were conducted over these materials to elucidate their activity and product selectivity in CO_2-FTS. Reaction pathways leading to CO, CH_4 and C_{2+}-hydrocarbons were also identified. The transformation of as-prepared materials during CO_2-FTS into steady-state phases and spatial distribution of the latter were also investigated. This information was instrumental to successfully correlate the steady-state catalyst composition with product selectivity and, thus, to provide hints for hindering the selectivity to CH_4 in favor of C_{2+}-hydrocarbons.

Section 4.2 is focused on the investigation of hematite-containing catalysts prepared through controlled decomposition of in-house synthesized and commercial iron (II) oxalate dihydrate. A special focus was put on the role of redox properties of Fe_2O_3 for reaction-induced transformation into iron carbides. To this end, single-phase hematite materials with different size of crystallites as well as mixed phase materials differing in the hematite/maghemite ratio (α-/γ-Fe_2O_3) were prepared, characterized (both as fresh materials and after CO_2-FTS) and tested in CO_2-FTS. The obtained structural and catalytic results combined with mechanistic analysis of product formation as well as spatially resolved and transient kinetic scrutiny allowed to establish structure-activity-selectivity relationships. The defectiveness of iron carbides

determined from Mössbauer spectroscopic analysis and expressed as the C/Fe ratio of spent catalysts was established to be a key property relevant for the ability of iron carbides to activate CO_2, CO and H_2 and, consequently, for controlling product distribution.

Section 4.1
Generation of $Fe_xO_yC_z$

Fe_3O_4, Fe, FeO, Fe_xC_y
(different composition)

Section 4.2
Generation of Fe_2O_3

α-Fe_2O_3
(different crystallite size)

Section 4.3
Generation of promoted $Fe_xO_yC_z$

$\dfrac{Ar}{T\ °C}$ $FeC_2O_4 \cdot 2H_2O$ $\dfrac{air}{T\ °C}$

Fe_3O_4, Fe, Fe_xC_y
(different promoter)

IWI: M_2CO_3
(M=Li, Na, K, Rb, Cs)

α-Fe_2O_3 + γ-Fe_2O_3
(different composition)
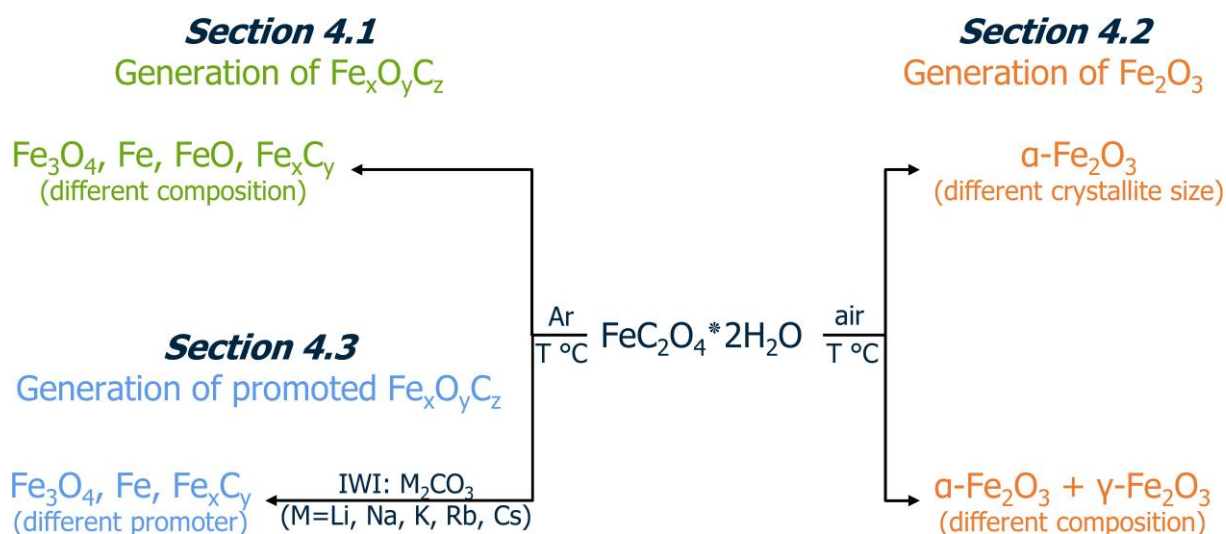
Figure 2.1.   A scheme demonstrating the strategy for achieving the stated objectives.

Finally, **Section 4.3** deals with magnetite-containing catalysts derived from commercial iron (II) oxalate dihydrate and promoted with an alkali metal (Li, Na, K, Rb or Cs). The effects of the kind and the amount of the dopant on the composition and physico-chemical properties of fresh and spent catalysts as well as on their performance in CO_2-FTS were analyzed in detail. Owing to spatially resolved analyses of catalyst composition and reaction rates of product formation in CO_2-FTS, it was possible to understand the role of the promoter for catalyst efficiency. The individual contribution of two different formation routes of methane production was established over materials with different alkali metal promoters or with different amounts of Rb. Secondary CO hydrogenation was determined to be the dominant pathway of CH_4 production over Rb- or Cs-doped catalysts. While direct CO_2 methanation prevails over non-promoted and Li-, Na- or K-promoted materials.

The main results and the relationships established in the current work are summarized in the **Conclusions**. A possible direction for further investigations is suggested in the **Outlook**.

3 Experimental part

3.1 Catalyst preparation

3.1.1 Iron (II) oxalate dihydrate synthesis

Iron (II) oxalate dihydrate was selected as the catalyst precursor because its decomposition can produce a big variety of single Fe-containing products (iron oxides, iron carbides, metallic iron) or their mixtures. Thus, the decomposition of iron (II) oxalate dihydrate in air leads to the formation of hematite (α-Fe_2O_3) or/and maghemite (γ-Fe_2O_3) [106-110]. Treating this precursor in an inert atmosphere below 570 °C produces magnetite (Fe_3O_4) or a mixture of magnetite and different iron carbides, e.g. Fe_3C (cementite), Fe_5C_2 (Hägg´s carbide), while the decomposition above 570 °C results in wüstite (FeO) [111-113]. The decomposition of iron (II) oxalate dihydrate in a flow of hydrogen or in a mixture of hydrogen and inert gas leads to the formation of α-Fe or a mixture of α-Fe and Fe_3C [114].

In the present study, commercial ($FeC_2O_4 \cdot 2H_2O$, Sigma Aldrich, 99 %) and in-house prepared iron (II) oxalate dihydrate materials were used for catalyst preparation. The synthesis of the latter material was carried out through a precipitation method as follows. Oxalic acid in the amount of 10% molar excess in regard to the total amount of Fe (including iron pellets) was dissolved in the minimal amount of water to prepare a saturated solution. This solution was added dropwise to a saturated aqueous solution of iron (II) sulfate, which contained a few metal-iron pellets (0.3 mm in diameter) in order to prevent the oxidation of Fe^{2+} to Fe^{3+}. Sulfuric acid was added to the solution of iron (II) sulfate until pH of 3 in order to prevent the formation of hydroxides. The reaction was carried out at 90 °C for 1 hour resulting in the formation of yellow precipitate, which was then filtered hot, properly washed with cold ethanol, and finally dried at 50 °C for 1 day.

Two different types of catalysts based on magnetite or hematite were prepared using commercial and in-house synthesized iron oxalate. To distinguish the kind of the precursor used for catalyst preparation "_c_" or "_h_" endings are introduced in the catalyst name, respectively.

3.1.2 Synthesis of magnetite-containing catalysts

Five magnetite-containing catalysts were synthesized from the in-house prepared iron (II) oxalate dihydrate as follows. The precursor was placed in a form of powder (about 3 g) into a

quartz tubular reactor located in an electrically heated furnace allowing 16 reactors to be treated in parallel. The samples were heated up in a flow of argon (20 mL/min) to the treatment temperature with a constant heating rate of 5 °C/min. Then the materials were tempered at the desired temperature of 330, 400 or 650 °C for 24, 1 or 1 h. The obtained materials are denoted as Fe_h_330, Fe_h_400 and Fe_h_650 (Figure 3.1). Two more catalysts were synthesized from the Fe_h_330 sample through its additional thermal treatment (after exposure to air at room temperature) in argon flow at 500 or 650°C for 5 h. They are abbreviated as Fe_h_330_500 and Fe_h_330_650.
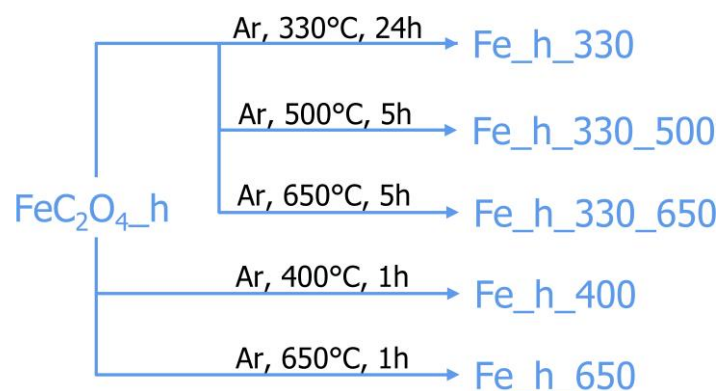
Figure 3.1. A scheme demonstrating preparation of magnetite-containing samples through thermal decomposition of in-house prepared iron (II) oxalate dihydrate ($Fe_2C_2O_4\_h$).

3.1.3 Synthesis of magnetite-containing catalysts promoted with an alkali metal

Magnetite-containing catalysts promoted with an alkali metal were prepared from commercial iron (II) oxalate dihydrate ($FeC_2O_4*2H_2O$, Sigma Aldrich, 99 %). Alkali metals, i.e., Li, Na, K, Rb or Cs, in form of the corresponding carbonate solutions were added to the oxalate through an incipient wetness impregnation followed by drying at 110 °C for 24 h. Hereafter, promoted or unpromoted catalyst precursors were placed into calcination apparatus described above and heated up to 330 °C with a heating rate of 5 °C/min. The decomposition was conducted in a flow of Ar (20 mL/min) for 24 h. The described conditions were applied previously for the synthesis of Fe_h_330 sample except in this case commercial iron (II) oxalate was used as a precursor. The prepared catalysts are denoted as Fe_c_xM, where "_c_" reflects the precursor used for synthesis, "x" and "M" represent the atomic ratio of alkali metal to Fe and the type of alkali metal, respectively. Two series of materials were synthesized by varying the nature of alkali metal (M = Li, Na, K, Rb or Cs) with a fixed ratio of the dopant to Fe (x = 0.005) and by varying the amount of Rb promoter (x = 0, 0.001, 0.005, 0.01, and 0.05).

3.1.4 Synthesis of hematite-containing catalysts

Two series of iron (III) oxide samples were synthesized using both in-house prepared and commercial iron (II) oxalates dihydrate. Generally, the preparation procedure was similar to that described above (see section 3.1.2). The first series (Series 1) of Fe_2O_3 catalysts includes single-phase hematite materials with different size of crystallites. They were obtained as follows. Commercial iron (II) oxalate dihydrate was first heated up to 180 °C in a flow of air (20 mL/min) and tempered for 16 h. After cooling down to room temperature, the catalysts were heated up again in a flow of air and calcined at 300, 400, 500 or 600 °C for 24 h. The prepared catalysts are abbreviated as Fe_c_10nm, Fe_c_14nm, Fe_c_19nm and Fe_c_26nm, respectively (Figure 3.2). Where the number in the catalyst name reflects the crystallite size of the hematite phase in nanometers as was determined by powdered XRD analysis (Table 4.6). Fe_h_31nm was synthesized through a decomposition of in-house prepared iron (II) oxalate dihydrate in a flow of air (20 mL/min) at 330 °C for 24 h and subsequent calcination (after cooling down to room temperature) in a flow of air at 650 °C for 5 h.
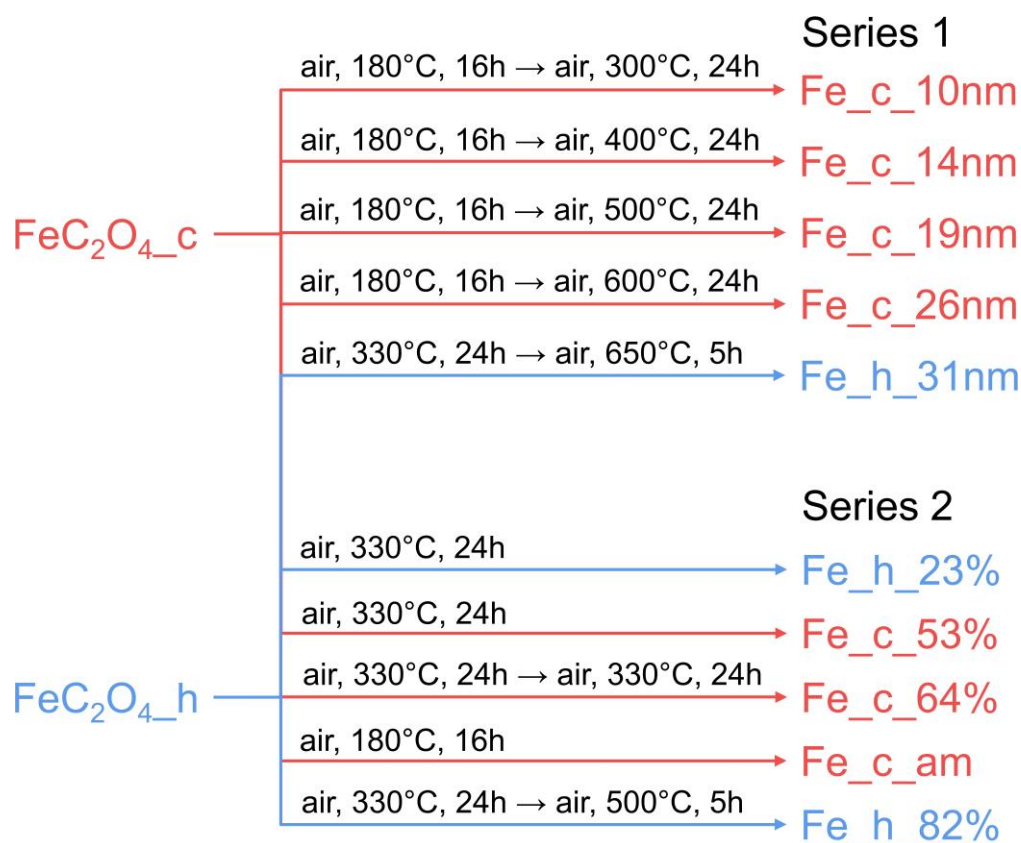

Figure 3.2.   A scheme demonstrating preparation of hematite-containing samples through a thermal decomposition of commercial ($Fe_2C_2O_4$_c) or in-house prepared ($Fe_2C_2O_4$_h) iron (II) oxalate dihydrates.

The second series (Series 2) of iron (III) oxide catalysts consists of mixed-phase (α-Fe_2O_3/γ-Fe_2O_3) samples differing in the hematite-maghemite ratio. The number in the catalyst name reflects the weight amount of the α-Fe_2O_3 phase in the prepared material as was determined by powdered XRD analysis (Table 4.6). Three catalysts were obtained using the commercial iron (II) oxalate dihydrate. Fe_c_am (X-ray amorphous material) and Fe_c_53% were prepared through its thermal decomposition in a flow of air (20 mL/min) at 180 °C for 16 h and at 330 °C for 24 h, respectively (Figure 3.2). The catalyst abbreviated as Fe_c_64% was obtained through an additional thermal treatment (after cooling down to room temperature) of Fe_c_53% in a flow of air at 330 °C for 24 h. Two other catalysts were synthesized using the in-house prepared iron (II) oxalate dihydrate. Fe_h_23% was obtained through its thermal decomposition in a flow of air (20 mL/min) at 330 °C for 24 h. Fe_h_82% was obtained through an additional calcination of the as-prepared Fe_h_23% material in a flow of air at 500 °C for 5 h.

3.2 Characterization methods

The specific surface area of as-prepared catalysts was calculated from *nitrogen adsorption-desorption isotherms* obtained at -196 °C using a BELSORP-mini II (BEL Japan, Inc.) instrument. To remove adsorbed gases from the surface of all materials, they were initially treated in vacuum at 100 °C for 30 min prior to the measurements. The specific surface area was calculated applying the Brunauer-Emmet-Teller (BET) equation for the N_2 relative pressures $0.1 < p/p_0 < 0.3$.

X-ray diffraction (XRD) patterns were recorded on a Stoe Stadi P transmission diffractometer equipped with a DECTRIS Mythen2 1K detector applying Ge (111) monochromatized Mo Kα_1 radiation (40 mA, 50 kV, 0.70930 Å). Prior to the measurements, the materials were grinded to a fine powder and placed between two acetate foils. Data collection was made with 0.01 °/s resolution. The pattern fit was performed with Pseudo-Voigt function using the HighScore Plus software package (Panalytical) to determine reflexes positions and phase profiles. The phase composition of the samples was identified using the PDF-2 database of the International Center of Diffraction Data (ICDD). The Rietveld method was applied for quantitative phase analysis. The size of crystallite was calculated using Scherrer equation applied to the reflexes characteristic for a specific Fe-containing phase, i.e. ((111), (220), (311), (222), (422)) characteristic for Fe_3O_4; ((110), (200), (211)) characteristic for Fe; ((111), (200), (220), (311), (222)) characteristic for FeO; (012), (104), (110), (113), (024) characteristic for α-Fe_2O_3; (022),

(113), (004), (224), (115), (333), (044) characteristic for γ-Fe_2O_3. The crystallite size values determined for different reflexes were then averaged.

The phase composition of as-prepared and spent (after CO_2-FTS) catalysts was also determined by *Mössbauer spectroscopy*. The measurements were performed at room temperature on a conventional spectrometer (NZ-640, Hungary) operating in a constant acceleration mode with a speed reversal. The spectra were recorded in the mode of moving radiation source [57]Co placed in a matrix of metal rhodium. Chemical shifts are presented in relation to α-Fe. The data were processed using an in-house developed program for spectrum deconvolution into Lorentzian functions.

To investigate the reducibility of as-prepared materials *hydrogen temperature-programmed reduction (H_2-TPR) measurements* were performed using an in-house built set-up containing eight quartz tubular reactors, which are individually heated and connected to an on-line mass spectrometer (Pfeiffer OmniStar GSD 300 01) for analyzing gas-phase components. Prior to the measurements all catalysts placed into individual reactors (about 50 mg) were heated up to 300 °C in a flow of argon in order to remove the adsorbed gases. After the treatment, the reactors were cooled down to room temperature in the same flow. The feed gas mixture was changed to 5 vol% H_2/Ar (20 mL/min per reactor) while the reactors were heated up to 900 °C in a sequential mode with a constant heating rate of 10 °C/min. The data were recorded at the following atomic mass units (AMU): 2 (H_2), 16 (O, CH_4), 17 (OH), 18 (H_2O), 28 (CO, CO_2), 32 (O_2), 40 (Ar) and 44 (CO_2). The hydrogen concentration was calculated from the ratio of AMU signal of 2 (H_2) to AMU signal of 40 (Ar) using the sensitivity factor obtained by analyzing calibration gas mixtures.

The kinetics of reduction of fresh catalysts with H_2 and reoxidation of their reduced counterparts with CO_2 was analyzed by means of *thermogravimetric analysis (TGA)*. The measurements were carried out on a SETSYS Evolution 16/18 (Setaram) instrument. Typically, 20 mg of a sample was placed into a cup of thermal balances. Hereafter, the system was evacuated at room temperature. Then the volume of thermal balances was flushed with He at ambient pressure accompanied with heating up to 300 °C with a heating rate of 10 °C/min in order to remove the adsorbed gases. After no weight change was registered, the feed gas was changed to a H_2:He = 1:1 (32 mL/min) mixture and TGA data were recorded for about 3 hours until the reduction process was finished. After that the system was flushed with He to remove H_2. Then a mixture of CO_2:He = (1:1) was fed and the data of catalyst reoxidation was collected for about 24 h. Another type of the experiments was performed in addition to the above described. In these

experiments a CO_2:He (1:1) mixture was directly fed to the non-reduced materials after flushing the thermal balances with He and reaching 300 °C in order to investigate oxidizability of fresh magnetite-containing catalysts.

Transmission electron microscopy (TEM) analysis was carried out on a FEI Tecnai G2 20 S-TWIN instrument operating at 200 kV. Sample preparation included its grinding into a fine powder and dispersion in ethanol using an ultrasonic bath. The dispersed sample was put on the copper grids coated with a 2 nm carbon layer and dried for 5 min at 60 °C. Then a second copper grid also coated with 2 nm carbon layer was placed on top and the sample was transferred into the microscope. *Selected area electron diffraction (SAED) analysis* was performed on the same instrument using a slot that allowed the investigation of the sample area with a diameter of 200 nm.

Scanning electron microscopy (SEM) was applied to investigate the morphology of iron oxalates, fresh and spent (after CO_2-FTS) catalysts. The analysis was performed on a Hitachi TM-1000 (Japan) instrument operating at 15 kV. The sample was dispersed on electro conducting tape before the transfer into the instrument.

The interaction of selected catalysts with CO_2 at ambient pressure was investigated using *in situ diffuse reflectance infrared Fourier transform spectroscopy (in situ DRIFTS)*. The DRIFT spectra were obtained using a Nicolet 6700 FTIR spectrometer (ThermoFischer Scientific) equipped with a commercial DRIFT cell (Harrick) with CaF_2 windows and a highly sensitive MCT detector. The catalyst in a form of a fine powder was placed in the sample holder and heated up to 300 °C in He flow (25 mL/min). After waiting for 30 minutes in order to remove adsorbed gases, the starting spectrum was recorded. After that the feed gas was changed to a CO_2:He = 1:1 mixture (25 mL/min) and spectra were collected after 30 min of exposure at 300 °C with a spectral resolution of 4 cm^{-1}. Then the sample was cooled down in the flow of He to the room temperature and exposed again to a CO_2:He mixture. Other spectra were recorded after 30 min of exposure.

X-ray fluorescence spectroscopy was applied for the element content analysis. The data were collected using a Panalytical Epsilon 1 spectrometer operating with an Ag X-ray source. Typically, each sample in form of powder was placed into the sample holder which was capped with Mylar Foil towards the source/detector. The spectra analysis was made using the fundamental parameter approach based on the theoretical relationship between measured X-ray intensities and the concentrations of elements in the sample.

Inductively coupled plasma optical emission spectroscopy (ICP-OES) was utilized to determine the amount of Fe and different alkali promoters (except for Cs) using Varian 715-ES ICP-Emission-Spectrometer. The amount of Cs in the catalysts was identified by means of *atomic absorption spectroscopy (AAS)* using Perkin-Elmer AAnalyst 300 spectrometer. Generally, 10 mg of each sample was dissolved in 8 ml of aqua regia. The sample preparation system (Multiwave PRO, Anton Paar) operating at 220 °C and 50 bar was applied for the sample digestion with a microwave-assisted method. The digested solution was diluted to 100 ml and measured by ICP-OES. The data analysis was carried out on the software (ICP Expert) of 715-ES.

3.3 Transient experiments and their kinetic evaluation

To derive mechanistic and kinetic insights into the investigation of CO, CO_2 and H_2 interaction with spent catalysts, pulse experiments were performed in a *temporal analysis of products reactor (TAP-2)* system. This technique was described in detail elsewhere [115-117]. Typically, a small amount of catalyst (20 mg, $250 - 450$ µm fraction) was placed in a quartz tubular reactor and fixed between two layers of quartz particles ($250 - 450$ µm fraction) within the reactor's isothermal zone. The reactor was initially evacuated at room temperature and then heated up to 300 °C in vacuum with a heating rate of 10 °C/min. CO_2 and CO interactions were studied by means of single pulse experiments introducing CO_2:Ar = 1:1 or CO:Ar = 1:1 mixtures in the reactor at 300 °C. H/D exchange experiments were carried out by pulsing of a H_2:D_2:Ar = 1:1:1 mixture at 400 °C.

The single pulse introduced in the reactor contained approximately 10^{15} molecules. The mass transport is quantitatively described by the Knudsen diffusion regime under these conditions and any collisions of gas-phase species could be neglected. Therefore, only the analysis of heterogeneous reaction steps was performed. An on-line quadrupole mass spectrometer (HAL RC 301, Hiden Analytical) was used for the quantitative analysis of the feed components and possible reaction products. The following atomic mass units (AMU) were recorded: 44 (CO_2), 40 (Ar), 28 (CO, CO_2), 4 (D_2), 3 (HD), and 2 (H_2). Each mixture was pulsed 10 times and the signal for each AMU was averaged to improve the signal-to-noise ratio. The concentration of the pulsed gases and the formed products was determined from the peak area of the corresponding signal related to that of Ar. Blank pulsing of the mixtures used in the experiment in the reactor containing only quartz particles was performed to determine the sensitivity factors and fragmentation patterns required for the calculation. The model-free approach developed for

this technique [115] was used to transform the experimental responses of CO_2, CO and Ar into dimensionless form according to equations 3.1-3.2. This transformation allows to unambiguously give information about the type of interaction (diffusion, reversible or irreversible adsorption) of pulsed component with the catalyst.

$$\text{Dimensionless flow} = \frac{F(CO_x)*L^2}{PS*D(CO_x)} \tag{3.1}$$

$$\text{Dimensionless time} = \frac{t*D(CO_x)}{L^2} \tag{3.2}$$

where $F(CO_x)$ is the flux of CO or CO_2, L stands for the reactor length, PS is the abbreviation for the pulse size, t is time and $D(CO_x)$ stands for the diffusion coefficient of CO or CO_2.

Different kinetic models were applied to fit the transient responses of CO_2 and CO in order to gain mechanistic and kinetics insights into the activation (adsorption/desorption and dissociation/association) of these reactants as described elsewhere [118, 119]. The TAP reactor is considered as a pseudo-homogeneous reactor consisting of three different sequential zones: upstream inert zone, catalyst zone and downstream inert zone. The mass balances for gas-phase and surface species outside the catalyst layer can be described by equations 3.3 and 3.4, respectively:

$$\frac{\partial C_i}{\partial t} = D_{Knudsen}^{eff} \times \frac{\partial^2 C_i}{\partial x^2} \tag{3.3}$$

$$\Theta_i = 0 \tag{3.4}$$

The expression for the reaction in the catalyst zone was included in the mass balances for gas-phase (equation 3.5) and surface species (equation 3.6):

$$\frac{\partial C_i}{\partial t} = D_{Knudsen}^{eff} \times \frac{\partial^2 C_i}{\partial x^2} + \sum_j \rho_{cat} v_{ij} r_j \tag{3.5}$$

$$\frac{\partial \Theta_m}{\partial t} = \sum_j \frac{v_{ij} r_j}{C_{total}} \tag{3.6}$$

where

$$r_j = k_j \prod_1 C_i^{n_i} \prod_m \Theta_m^{n_m} \tag{3.7}$$

where C_{total} is the total concentration of surface species and $D_{Knudsen}^{eff}$ stands for the effective Knudsen diffusion coefficient of gas-phase species, $0 \leq n_i \leq 1$, $0 \leq n_m \leq 2$, $\Theta_i = \frac{C_i}{C_{total}}$.

Spatial approximation was applied to transform the resulting partial differential equations into coupled ordinary differential equations, which were then integrated by numerical routine PDEONE. The determination of kinetic parameters was carried out in a wide range of possible values ($10^{-4} - 10^8$) by using first a genetic algorithm in order to find good starting values and then the Nelder–Mead simplex algorithms to find the exact values. The quality of the fit was defined by an objective function determined as the sum of squares of the lowest deviation between the respective points of the experimental data and simulated data. The significance of the parameters for the objective function was determined by applying the sensitivity analysis to the best describing kinetic model.

3.4 Catalytic tests

CO_2 hydrogenation tests were carried out in an in-house developed and built set-up equipped with 50 continuous-flow fixed-bed stainless-steel tube reactors operating in parallel. The reactor length, outer and inner diameters are 260, 6 and 4 mm, respectively. The total feed flow is equally distributed within all the reactors. In all catalytic tests, the reaction mixture $H_2:CO_2:N_2$ = 3:1:0.3 was fed with a flow rate of about 5.8 mL/min per reactor. The gas-phase feed components and the reaction products were analyzed by an on-line Agilent 7890A gas chromatograph. Due to the system of valves, the outlet gases after each reactor could be analyzed in a sequential mode. The chromatograph is equipped with AL/S column for C_1-C_8 hydrocarbons separation and FFAP column for C_9-C_{18} hydrocarbons separation connected to a flame ionization detector (FID) and with HP Plot/Q column for CO_2 and H_2O separation and MolSieve 5A column for H_2, O_2, N_2 and CO separation connected to a thermal conductivity detector (TCD). To avoid condensation of long-chained hydrocarbons stainless steel lines connecting the reactor outlet and the GC inlet were heated up to about 180 °C, GC valves and loops were heated up to 200 °C.

Two types of catalytic tests were performed with magnetite-containing catalysts, namely, "screening" ($T_{reaction}$ = 250 - 350 °C) and "long-term stability" ($T_{reaction}$ = 300 °C) tests and only "long-term stability" tests were performed with hematite-containing catalysts. The "screening" test with magnetite-containing samples was conducted to investigate the effect of reaction temperature on catalytic performance. The reactor was filled with about 300 mg of each catalyst (250 – 450 μm fraction) within its isothermal zone. In addition, 700 mg of SiC (ESK-SiC, F30, 500 – 710 μm fraction) was placed on top of the catalyst bed to ensure the plug flow and to preheat the feed mixture. The reactors were initially heated up to 250 °C in N_2 and

simultaneously pressurized to 15 bar. In case of magnetite-containing samples, no pretreatment is required before starting the experiment, therefore, the reaction mixture was directly fed (GHSV=1170 ml/g_{cat}/h) after reaching the set temperature. The reaction conditions were maintained for about 40 h and the data were collected. After that the temperature was increased to 300 °C and kept constant for another 40 h followed by a further increase to 350 °C, where the CO_2-FTS reaction was conducted for the final 40 h. At the end, the catalysts were cooled down in N_2 to room temperature.

The "long-term stability" tests were conducted in order to investigate: (i) catalyst on-stream stability, (ii) the effect of CO_2 conversion on product selectivity and (iii) in the case of magnetite containing catalysts to check if catalytic performance at 300 °C depends on the way how this conditions were achieved, i.e. direct feeding of the reaction mixture at the desired temperature or starting the CO_2-FTS at 250 °C with a consecutive increase in the temperature to 300 °C (see the above-described "screening" test). Hematite-containing catalysts were reductively treated before starting CO_2-FTS tests. The filled reactors were initially heated up to 300 or 400 °C in N_2 and simultaneously pressurized to 15 bar. After reaching the set temperature, a H_2:N_2 = 1:1 mixture was fed with a flow rate of about 11.8 mL/min per reactor for 2 h. After that the reactors were cooled down (if the reduction was conducted at 400 °C) in a flow of N_2 to the reaction temperature of 300 °C. Then N_2 was replaced by the reaction feed for about 110 h. In the case of magnetite-containing catalysts, the reactors were directly heated up to 300 °C and the reaction mixture was fed for about 95 h. Finally, the catalysts were cooled down in N_2 to room temperature. Different catalyst amounts (600, 300, 100, 50, 20, 10 mg) were used in the "long-term stability" test to achieve different levels of CO_2 conversion.

The conversion of CO_2 ($X(CO_2)$), product yield (Y_i) and selectivity (S_i) were calculated according to equations 3.8–3.10, respectively. The inlet molar flows of the feed components were established through separate measurements using a bypass line. The reaction-induced changes in the number of moles were considered by using the inert standard N_2 in the reaction feed. Carbon balance was established to be higher than 98 % in all experiments. Chain growth probability (α) was calculated according to the Anderson-Schulz-Flory distribution (equation 3.11) using C_3-C_8 hydrocarbons with a linear approximation accuracy higher than 95%.

$$X(CO_2) = 1 - \frac{\dot{n}_{CO_2}^{out}}{\dot{n}_{CO_2}^{in}} \tag{3.8}$$

$$Y_i = \frac{a_i \dot{n}_i^{out}}{\dot{n}_{CO_2}^{in}} \tag{3.9}$$

$$S_i = \frac{Y_i}{X_{CO_2}} = \frac{a_i \dot{n}_i^{out}}{\dot{n}_{CO_2}^{in} - \dot{n}_{CO_2}^{out}} \tag{3.10}$$

$$\ln \frac{S_i}{a_i} = a_i \ln \alpha + \ln \frac{(1-\alpha)^2}{\alpha} \tag{3.11}$$

where $\dot{n}_{CO_2}^{in}$ represents the inlet molar flow of CO_2 and $\dot{n}_{CO_2}^{out}$ is the molar flow of CO_2 at the reactor outlet. a_i and $\dot{n}_i^{out}$ stand for the number of carbon atoms in the component i and the molar flow of this component, respectively. Subscripts *in* and *out* are used to distinguish the inlet and outlet molar flows. α is the chain growth probability.

4 Results and discussion

4.1 Magnetite-containing catalysts

The advantage of catalysts composed of magnetite, wüstite, metallic iron and/or iron carbides is that they can be directly applied for CO_2-FTS experiments without any preceding reductive treatment. Thus, it is possible to understand the reaction-induced transformations of as-prepared different iron-containing phases purposefully created through the decomposition of iron (II) oxalate dihydrate.

4.1.1 General characterization of fresh catalysts

Fresh samples were characterized by means of N_2 adsorption technique. The obtained specific surface area (S_{BET}) values are presented in Table 4.1. Fe_h_330 prepared at the lowest temperature possesses the highest specific surface area of 32 m²/g within all studied catalysts. The values are lower for the samples obtained after an additional treatment of the above catalyst at 500 or 650 °C in Ar and are 22 or 17 m²/g, respectively. The corresponding S_{BET} values of the catalysts prepared directly at 400 or 650 °C are 24 and 11 m²/g, respectively. Therefore, it is likely that high-temperature treatment causes sintering of crystallites and accordingly a decrease in the surface area.

Table 4.1. The results of catalysts characterization. Phase composition (wt. %) determined from XRD and Mössbauer (in brackets) spectroscopic analysis, the size (coherent scattering region (CSR)) of Fe_3O_4, FeO and Fe crystallites, specific surface area of fresh samples (S_{BET}).

Catalyst	Fe_3O_4 / %	Fe / %	FeO / %	Fe_3C / %	Fe_5C_2 / %	CSR (Fe_3O_4) /	CSR (Fe) /	CSR (FeO) /	S_{BET} / m²/g
Fe_h_330	82.8 (70.3)	3.6 (2.4)	-	13.5 (27.3)	-	22	20	-	32
Fe_h_400	83.2 (75.9)	2.1 (1.5)	-	8.1 (5.8)	6.7 (16.8)	23	24	-	24
Fe_h_330_500	76.4 (74.6)	23.6 (25.4)	-	-	-	27	29	-	22
Fe_h_650	63.2 (63.3)	26.5 (27.4)	10.2 (9.3)	-	-	49	55	13	11
Fe_h_330_650	38.4 (41.2)	16.0 (19.4)	45.6 (39.4)	-	-	31	31	34	17

All fresh samples were characterized by means of XRD analysis to determine the phase composition (Table 4.1). The obtained XRD patterns are shown in Figure 4.1. All catalysts contain Fe_3O_4, however, its fraction as well as the fractions of metallic Fe, FeO or iron carbides depend on the temperature, at which the catalysts were prepared. Iron carbides were detected in the materials prepared at 330 or 400 °C. Fe_h_330 contains Fe_3O_4 (82.8 %), Fe_3C carbide (13.5%) and metallic Fe (3.6 %). The content of Fe_3O_4, Fe_3C and Fe in Fe_h_400 is 83.2, 8.1 and 2.1%, respectively. In addition, the presence of Fe_5C_2 carbide with the corresponding fraction of 6.7% was identified in this sample. The presence of iron carbides can be explained as follows. The decomposition of iron oxalate dihydrate yields gas-phase CO and CO_2 and FeO. Iron (II) oxide is unstable below 570 °C and disproportionates to Fe_3O_4 and metallic Fe. The latter compound can react with produced CO to iron carbides [114]. The Fe_h_330_500 sample contains only Fe_3O_4 (76.4 %) and metallic Fe (23.6%). The absence of any iron carbides in this catalyst can be due to their low thermal stability. For example, Fe_3C is unstable and decomposes in the temperature range of 415 – 535 °C [111]. When the Fe_h_330 catalyst was additionally calcined at 500 °C an increase in the content of metallic Fe from 2.6 to 23.6% was determined. The increase indirectly supports the assumption about the effect of preparation temperature on the content of iron carbides. The two catalysts treated directly at 650 °C or at 330 and 650 ℃ contain FeO with the fraction of 10.2 or 45.6%. The content of Fe_3O_4 and metallic iron determined for Fe_h_650 is 63.2 and 26.5%, respectively. The corresponding phases are present in Fe_h_330_650 with the fractions of 38.4 and 16.0%.
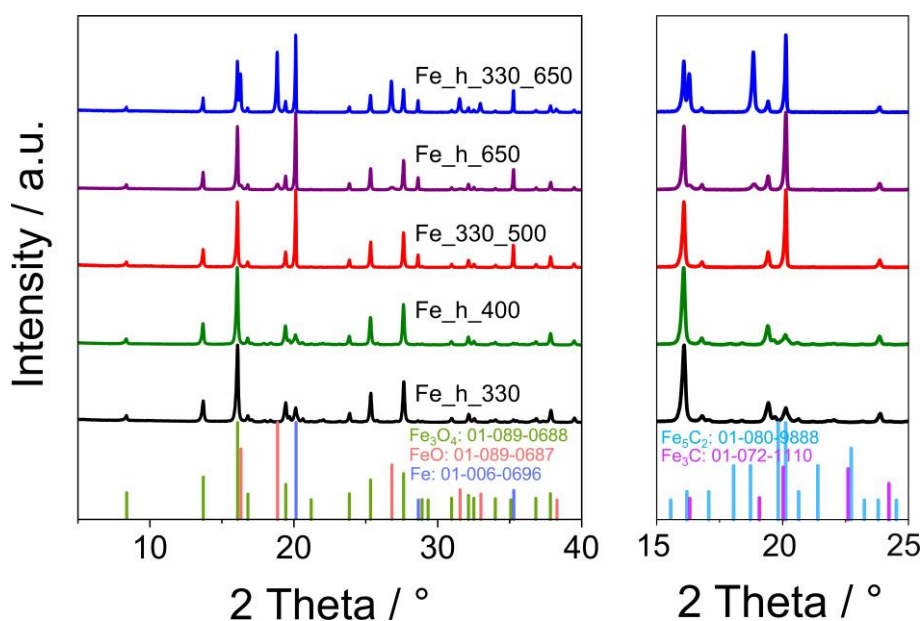

Figure 4.1.   XRD patterns of fresh magnetite-containing catalysts.

The crystallite size of Fe_3O_4 and Fe phases, which are present in all materials, corelates well with the specific surface area of the catalysts. The smaller the crystallite size, the larger the specific surface area is (Table 4.1). However, such correlation is not always present as a particle might consist of several crystallites and, therefore, the crystallite size might not reflect the particle size.

In addition to XRD analysis, which is not sensitive to amorphous phases, Mössbauer spectroscopic measurements were performed (Figure A.1). The obtained composition of Fe_h_330_500 and Fe_h_650 catalysts is in good agreement with the results of XRD analysis (Table 4.1). The amount of the FeO phase in Fe_h_330_650 is slightly lower in comparison with that obtained by XRD. There is a big discrepancy in the content of iron carbides in Fe_h_330 and Fe_h_400 catalysts determined by Mössbauer spectroscopy and XRD. It is highly underestimated by the latter method. This could be explained by the presence of amorphous phases and the fact, that the complex structure and possible non-stoichiometry of iron carbides affect the intensity of reflexes and cause their broadening. Consequently, the sensitivity lowers that is detrimental for a proper identification of iron carbide phases by XRD.

DRIFT spectra of two samples Fe_h_330 and Fe_h_330_650 were recorded after their exposure to 50 vol% CO_2 in He at 300 °C and room temperature in order to check the potential of this characterization technique to analyze the adsorptive properties of materials (Figure A.2). No adsorbates could be detected at 300 °C for both catalysts and very weak features of chemisorbed species were detected only for Fe_330_650 at room temperature. The broad and very weak bands between 1700 and 1200 cm^{-1} could be ascribed to the stretching vibrations of surface carbonate and/or carboxylate species. The characteristic bands of monodentate ($\nu_{as}COO^-$: 1530-1470 cm^{-1}; ν_sCOO^-: 1370-1300 cm^{-1}), bidentate ($\nu C=O$: 1620-1530 cm^{-1}; $\nu_{as}COO^-$: 1270 – 1250 cm^{-1}), noncoordinated carbonate ($\nu_{as}CO_3^{2-}$: 1450 -1420 cm^{-1}), and carboxylate (CO_2^-) ($\nu_{as}COO^-$: 1630-1560 cm^{-1}, ν_sCOO^-: 1420-1350 cm^{-1}) species were reported to be present in this range [120]. The absence of any bands in the spectrum of Fe_h_330, which contains mainly magnetite and small amounts of Fe_3C, suggests that these compounds weakly interact with CO_2. Previous studies dealing with magnetite materials also did not observe adsorbed carbonate species [121, 122]. Therefore, CO_2 adsorption on Fe_h_330_650 should be related to FeO present in this catalyst. However, due to the presence of a big variety of possible adsorbed species, which could superimpose in this range, a proper assignment of these broad weak bands to individual adsorbates is not possible. Moreover, the strong light adsorption by the catalysts decreases the sensitivity and makes the use of this technique non-informative.

The morphology of fresh catalysts was investigated by means of TEM analysis, which showed that all the materials consist of coarse-grained particles (Figure 4.2). However, different morphological features could be observed depending on the temperature, at which the samples were prepared. Fe_h_330 is highly crystalline. Lattice fringes detected in these images indicate the presence of Fe_3O_4. The particles are covered by a lower-crystallinity shell of about 6 nm thickness. The particles of Fe_h_400 also have a core-shell structure. But the shell is thinner (2 nm) and slightly more crystalline. Fe_h_330_500 forms a core-shell structure as well with a less defined shell appearance. No clear shell is visible in the images of Fe_h_650 and Fe_h_330_650, which consist of larger particles. The detected lattice fringes are denoted to Fe_3O_4.
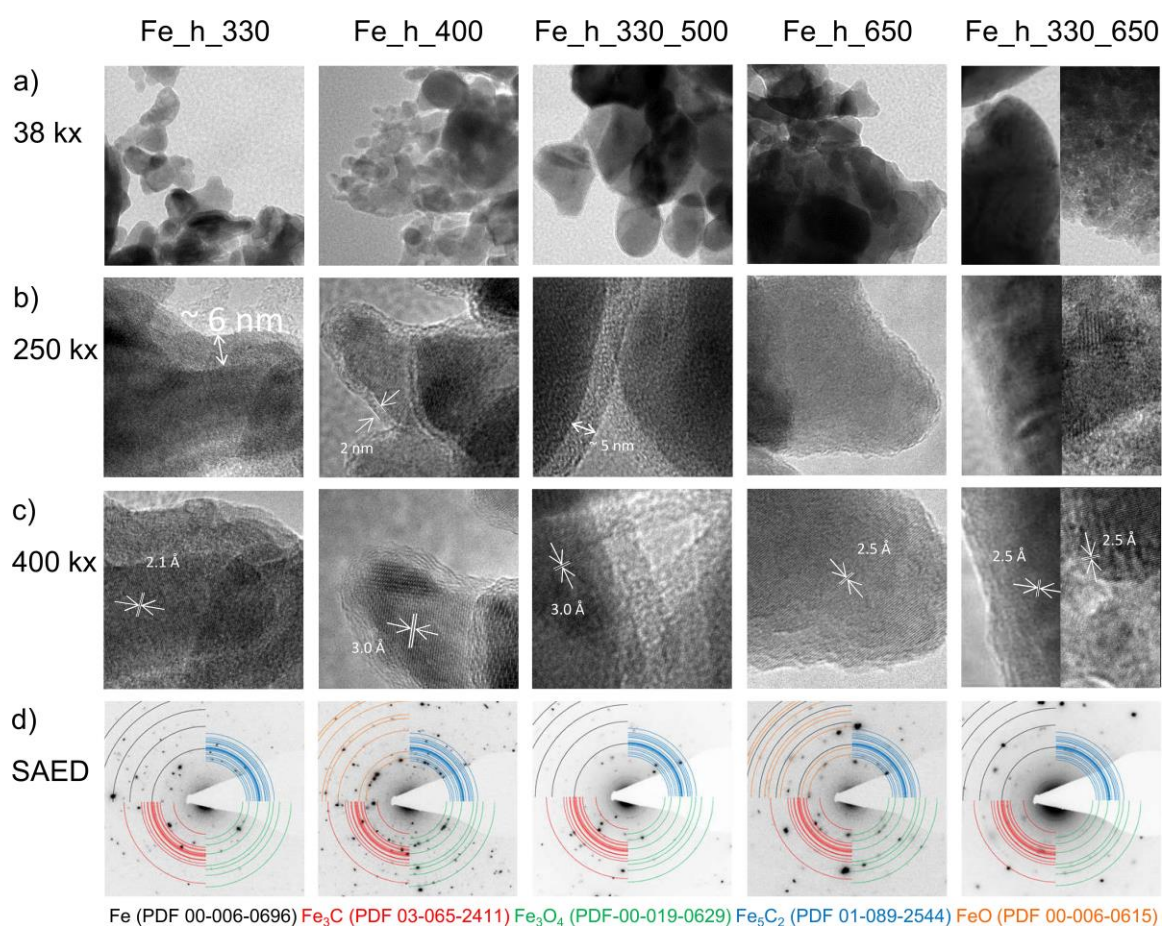
Figure 4.2. TEM images of fresh samples recorded at representative sample positions with (a) 38000, (b) 250000 and (c) 350000 magnifications; (d) SAED patterns recorded at the same sample location. Different colors reflect different possible phases present in the materials.

The information obtained from the combined XRD, Mössbauer and TEM analysis could be summarized as follows. The formation of core-shell structures in the materials prepared at low temperatures (330, 400 °C) is observed. The core supposedly consists of Fe_3O_4 with the shell

34

containing metal iron and iron carbides. The transformation of iron carbide shell into metallic iron is seen when Fe_h_330 sample was treated additionally at 500 °C. Fe_3O_4 in the core partially converted into FeO covered with the metallic iron shell is observed for the catalysts prepared at 500 and 650 °C.

4.1.2   Redox properties of fresh catalysts

Reducibility of magnetite-containing catalysts was analyzed by H_2-TPR measurements to check if this material property indirectly affects catalyst activity and product selectivity in CO_2-FTS. The corresponding H_2-TPR profiles in form of outlet H_2 flow rate are shown in Figure 4.3. A continuous consumption of hydrogen is observed for all catalysts above 400 °C without any clearly distinguished maximum. This result is in line with a previous study dealing with Fe_3O_4-nanocatalysts [76]. The reduction of magnetite comprises two consecutive steps: $Fe_3O_4{\rightarrow}FeO{\rightarrow}Fe$, with the first step proceeding at lower and second step at higher temperatures [123]. These pathways seem to be appliable for the present materials, although due to their complex composition the individual steps are not well-resolved in the obtained H_2-TPR profiles. There is a distinctive peak of H_2 consumption below 400 °C for two catalysts containing iron carbides phases. This peak is characterized by the maximum of hydrogen consumption at about 280 – 300 °C and could be ascribed to a complete reduction of iron carbides resulting in the formation of metallic Fe and gas-phase CH_4 [124]. Methane was experimentally detected at the AMU signal of 16 also having the maximum in the same temperature range, while no AMU signals of 17 and 18 attributed to water were observed.
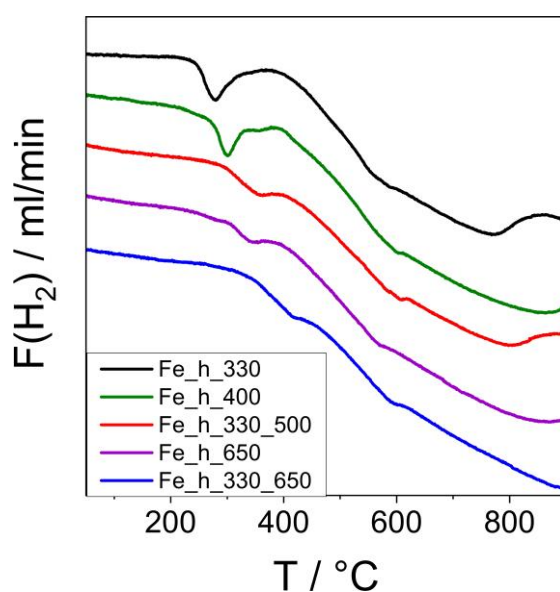

Figure 4.3.   Profiles of H_2 flow upon H_2-TPR (5 vol% H_2 in Ar, 20 mL/min) of fresh catalysts.

The kinetics of reduction/reoxidation and oxidation of magnetite-containing catalysts under isothermal conditions was also investigated. For this reason *in situ* TGA experiments were performed at 300 °C using H_2 (H_2:He = 1:1) or CO_2 (CO_2:He = 1:1) as reducing or oxidizing agents, respectively. Two kinds of oxidation experiments were carried out: i) fresh samples were first reduced with H_2 followed by reoxidation with CO_2 and ii) fresh catalysts were oxidized with CO_2 straightaway without any preceding treatment.
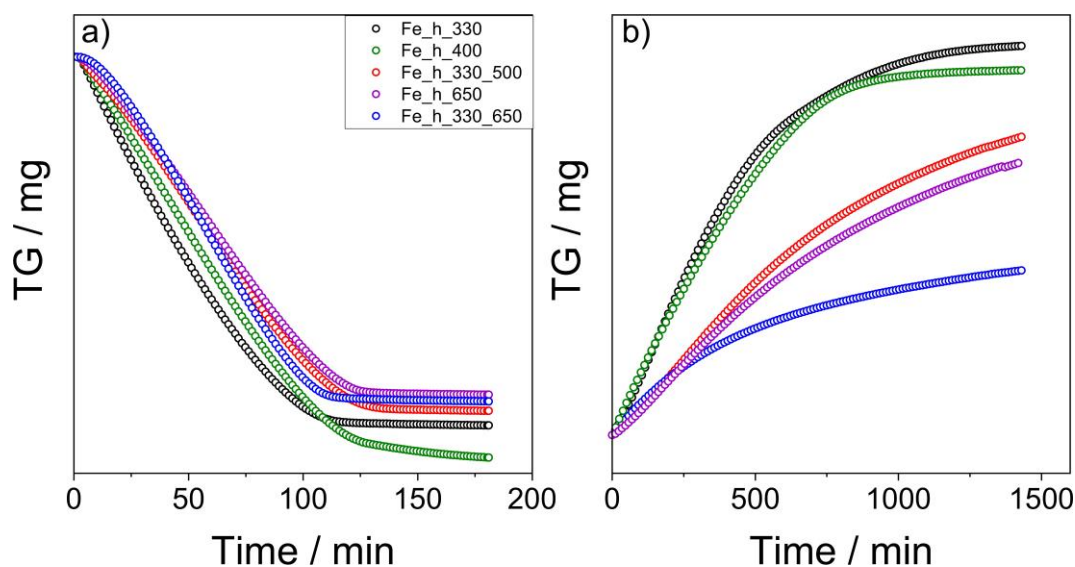
Figure 4.4.   TGA profiles obtained at 300 °C upon (a) reduction of fresh magnetite-containing catalysts with H_2 (H_2:He = 1:1) and (b) their subsequent reoxidation with CO_2 (CO_2:He = 1:1).

A decrease in the sample weight could be seen for all catalysts with rising time on H_2 stream up to about 2 h in the course of reduction of fresh samples (Figure 4.4a). No further changes were observed at longer times of treatment. The weight decrease is explained by the removal of lattice oxygen from iron oxide(s) by H_2 in form of water (equations 4.1-4.2) and due to the hydrogenation of iron carbides (equations 4.3-4.4). At a selected temperature of 300 °C the reduction of magnetite proceeds through a one-step mechanism: in this case no FeO intermediate is formed (equation 4.1) [125]. The fact that the TGA profiles reached a plateau could mean that iron oxides and iron carbides were completely converted into metallic iron. The different values of plateau observed for the different samples are accounted for the different amounts of metallic iron in the fresh catalysts, which cannot be reduced with hydrogen. The total weight loss in the TGA experiments is in accordance with the theoretical weight loss calculated based on the composition obtained from XRD analysis and Mössbauer spectroscopic measurements (Table 4.2).

Table 4.2.   Comparison of theoretical (based on Mössbauer and XRD data) and real weight loss obtained in TGA experiments upon reduction of fresh magnetite-containing catalysts.

Catalysts	Theoretical weight loss / %		Real weight loss / %
	Mössbauer	XRD	
Fe_h_330	21.26	23.79	22.13
Fe_h_400	22.42	24.07	23.59
Fe_h_330_500	20.62	21.12	21.26
Fe_h_650	19.57	19.74	20.29
Fe_h_330_650	20.16	20.77	20.69

$$Fe_3O_4 + 4H_2 \rightleftarrows 3Fe + 4H_2O \qquad\qquad (4.1)$$

$$FeO + H_2 \rightleftarrows Fe + H_2O \qquad\qquad (4.2)$$

$$Fe_3C + 2H_2 \rightleftarrows 3Fe + CH_4 \qquad\qquad (4.3)$$

$$Fe_5C_2 + 4H_2 \rightleftarrows 5Fe + 2CH_4 \qquad\qquad (4.4)$$
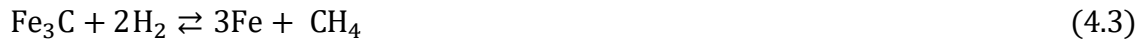
To have a quantitative comparison of the catalysts in terms of their reactivity towards reduction with H_2, an initial reduction rate was calculated using the linear part of the TGA curves (Figure A.3a). The obtained values for each catalyst are given in Table 4.3. The Fe_h_330 and Fe_h_400 catalysts possess the highest initial rates. All other materials do not differ significantly from each other in this regard. The Fe_h_330 and Fe_h_400 catalysts are composed of the smallest Fe_3O_4 crystallites within all the studied samples and accordingly possess the highest specific surface area. This could be the reason for their higher reducibility. Although there is the correlation between the initial rate of sample reduction and the specific surface area, the tendency is not strong. This might be explained by the fact that the composition of the samples is complex and different phases might have different reduction kinetics. Based on the present results, it could be concluded that the reduction of FeO proceeds faster than that of Fe_3O_4. According to the specific surface area values of Fe_h_330_650 and Fe_h_650, their reduction rate should be significantly lower. Their higher-than-expected reducibility might be related to the presence of FeO. This conclusion is in accordance with a previously reported study [125]. The fact that Fe_h_650 possessing lower specific area and FeO content than Fe_h_330_650 catalyst reveals a higher initial reduction rate could be due to much lower crystallite size of FeO. Although the reduction of iron carbides proceeds easier in comparison

with iron oxides (Figure 4.3), their contribution to the overall reduction process could not be significant, due to the low influence on the overall weight change.

Table 4.3. Initial rates of reduction of fresh catalysts with H_2 (r_{red}), reoxidation of their reduced counterparts with CO_2 (r_{reox}) and oxidation of fresh catalysts with CO_2 (r_{ox}).

Catalyst	r_{red} / mg/min	r_{reox} / mg/min	r_{ox} / mg/min
Fe_h_330	$5.53 \cdot 10^{-2}$	$8.39 \cdot 10^{-3}$	$2.19 \cdot 10^{-3}$
Fe_h_400	$4.26 \cdot 10^{-2}$	$7.62 \cdot 10^{-3}$	$1.83 \cdot 10^{-3}$
Fe_h_330_500	$3.26 \cdot 10^{-2}$	$4.00 \cdot 10^{-3}$	$1.57 \cdot 10^{-3}$
Fe_h_650	$3.03 \cdot 10^{-2}$	$3.83 \cdot 10^{-3}$	$8.52 \cdot 10^{-4}$
Fe_h_330_650	$2.79 \cdot 10^{-2}$	$3.57 \cdot 10^{-3}$	$1.03 \cdot 10^{-3}$

The reoxidation kinetics of the catalysts previously reduced by H_2 was studied through monitoring weight changes upon reaction with CO_2. After the reduction part was completed, the enclosed volume of thermobalances was flushed with He to remove H_2 without an exposure of samples to air and temperature change followed by CO_2 feeding. The obtained TGA profiles are given in Figure 4.4b. The increase in the sample weight with rising time on CO_2 stream is associated with the reaction of CO_2 with metallic iron formed upon the preceding sample reduction with H_2. As could be seen in Figure 4.4, the reoxidation process is significantly slower than reduction. No plateau is observed even after 1500 min on CO_2 stream, while the reduction process was finished after about 120 min on H_2 stream. Based on the TGA profile of Fe_h_330, for which a kind of plateau is observed, a maximal real weight gain was calculated. On this ground, it can be assumed that the final product of iron oxidation with CO_2 should be Fe_3O_4 for all catalysts (equation 4.5).

$$3Fe + 4CO_2 \rightleftarrows Fe_3O_4 + 4CO \tag{4.5}$$

An initial reoxidation rate was estimated using the linear part of the TGA curves (Figure A.3b). The determined values are one order of magnitude lower than those obtained for the reduction of magnetite-containing catalysts with H_2 (Table 4.3). Generally, the initial reoxidation rate correlates with the temperature of material preparation. The higher the temperature, the lower the reoxidation rate is. A possible explanation for such tendency might be the different crystallite size of metallic iron present already in the fresh compositions and formed during the reduction. As could be seen in Table 4.1, the crystallite size of metallic iron in the fresh catalysts

strongly depends on the temperature of catalyst preparation. It increases when the materials were treated at higher temperature. As these iron particles are also oxidized by CO_2, they may affect the kinetics of reoxidation. The increase in the size of crystallites might also happen during iron oxide(s) reduction.

The reduced Fe_h_330 and Fe_h_400 catalysts have the highest initial reoxidation rates, while the reoxidation ability of reduced Fe_h_330_500, Fe_h_330_650 and Fe_h_650 catalysts are about two times lower and do not differ much. The reduced Fe_h_330_650 material possesses the lowest rate. The fresh composition of this catalyst contains the highest concentration of wüstite with the largest size of crystallites. It could be assumed that iron formed upon reduction of FeO is less easy to reoxidize in comparison with iron formed from Fe_3O_4. This effect could be explained as follows. From a mechanistic point of view, the wüstite phase is formed as a result of the diffusion of metallic iron atoms into magnetite phase during the thermal treatment at 650 °C. Therefore, magnetite particles covered with a layer of wüstite are created. During the reduction, these particles could be completely converted into metallic iron particles with larger crystallites, which could lead to a slower reoxidation. Therefore, iron species formed after catalyst synthesis and upon reduction with H_2 differ in the reoxidation ability.

As it was mentioned above, another kind of experiments was carried out in order to investigate the oxidizability of fresh catalysts possessing metallic iron, wüstite and iron carbides, which theoretically could be oxidized. Analogously to the previous experiments, the oxidizability of fresh catalysts was studied by detecting the changes in sample weight during the reaction with CO_2. The obtained TGA profiles are given in Figure 4.5. An increase in the sample weight with rising time on CO_2 stream is observed and related to the formation of Fe_3O_4. Based on the weight gain, metallic iron, wüstite and iron carbide species should be oxidized to the magnetite phase. Similar to the reoxidation of reduced catalysts, the oxidation process of fresh materials takes a considerable period of time and is not completed even after 1500 min on CO_2 stream.

Table 4.3 presents the initial oxidation rate values calculated for each catalyst from linear dependences of weight gain on oxidation time (Figure A.3c). The oxidation rates are one to two orders of magnitude lower than the corresponding values of reduction rates and three to four times lower than the one related to the reoxidation. It could be assumed that iron formed upon reduction of fresh catalysts is oxidized easier than wüstite and iron carbide phases present in the compositions. Generally, the specific surface area of the materials correlates well with the initial oxidation rate (Figure A.4).
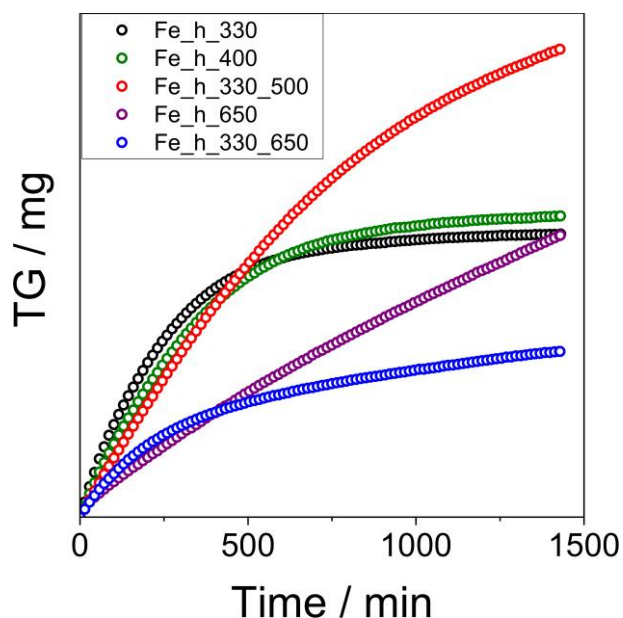
Figure 4.5. TGA profiles obtained at 300 °C upon oxidation of fresh magnetite-containing catalysts with CO_2 (CO_2:He = 1:1).

4.1.3 Catalyst screening test

To check the potential applicability of magnetite-containing catalysts for CO_2-FTS, a screening test was performed at 15 bar and at 250, 300, and 350 °C in total over 120 h on-stream. The reaction was conducted at each temperature for about 40 h starting at 250 °C. No preceding reductive catalyst treatment was performed. The profiles of CO_2 conversion and the selectivity to C_{2+} hydrocarbons, CH_4 and CO as a function of time on-stream at different temperatures are given in Figure 4.6. The Fe_h_330 and Fe_h_400 catalysts outperformed other catalysts in terms of CO_2 conversion at 250 and 300 °C. The activity of other materials improved with rising time on stream at these temperatures. No changes in the degree of CO_2 conversion were observed over all the catalysts tested at 350 °C. Fe_h_650 achieved the highest level of CO_2 conversion (0.44) at this temperature.

The catalysts also showed different product selectivity. Fe_h_400 produces mainly CH_4. The selectivity slightly increases with an increase in the reaction temperature and in CO_2 conversion. An uprising dependence was established for Fe_h_650, while a decreasing tendency in the selectivity to methane was determined for Fe_h_330 despite the increase in CO_2 conversion. The selectivity to CH_4 over Fe_h_330_500 and Fe_h_330_650 passes a minimum (below 0.1) at 300 °C and does not exceed 0.2 at 250 and 350 °C. Fe_h_650, Fe_h_330_500 and Fe_h_330_650 produce mainly CH_4 at 250 and 300 °C. But this selectivity decreases with increasing reaction temperature and conversion of CO_2. Fe_h_330 and Fe_h_400 reveal lower

40

selectivity to CO than other catalysts. The highest C_{2+}-hydrocarbons selectivity of about 0.6 was determined over Fe_h_330 and Fe_h_330_500 at 300 and 350 °C. The corresponding olefin/paraffin ratio values within C_2-C_4 hydrocarbons over these catalysts are 1 and 6 at 250 °C and 2.4 and 3.4 at 350 °C.
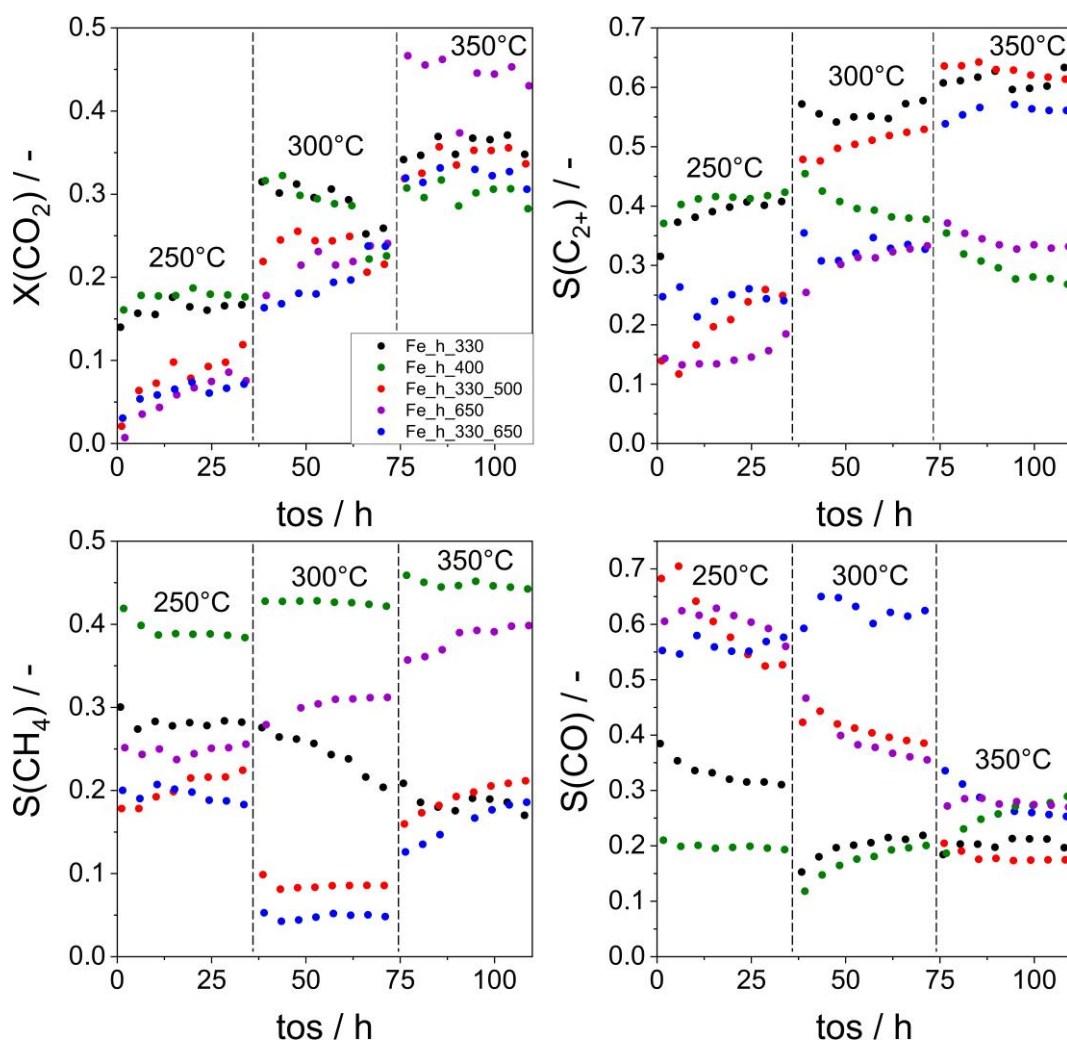
Figure 4.6.   On-stream profiles of CO_2 conversion and product selectivity in CO_2 hydrogenation over magnetite-containing catalysts. Reaction conditions: total pressure: 15 bar, reaction feed: CO_2:H_2:N_2 = 1:3:0.3, GHSV: 1170 mL/g_{cat}/h, reaction temperature: 250, 300 and 350 °C, catalyst amount: 300 mg.

The comparison of the best performing Fe_h_330, Fe_h_330_500 and Fe_h_330_650 catalysts in terms of product selectivity with the performance of the state-of-the-art non-supported and non-promoted Fe-containing catalysts is given in Figure 4.7. More detailed information about experimental conditions, such as total temperature, GHSV, pressure, etc. is provided in Table A.1. It could be seen that the Fe_h_330 and Fe_h_330_500 samples reveal high selectivity to C_{2+}-hydrocarbons on the level with top 10 best-performing materials at the same or lower

degree of CO_2 conversion. The comparison of the catalysts at similar level of CO_2 conversion shows that materials from the present study reveal the C_{2+}-hydrocarbons selectivity on the same level as the top 3 best-performing materials. The Fe_h_330_500 and Fe_h_330_650 samples showed much lower selectivity to methane and much higher olefin to paraffin (C_2-C_4 hydrocarbons) ratios of 5 or 6 in comparison with state-of-the-art catalysts. A comparable performance is usually achieved using promoted catalysts. Therefore, these results clearly demonstrate the potential of the approach applied for synthesis of selective catalysts.
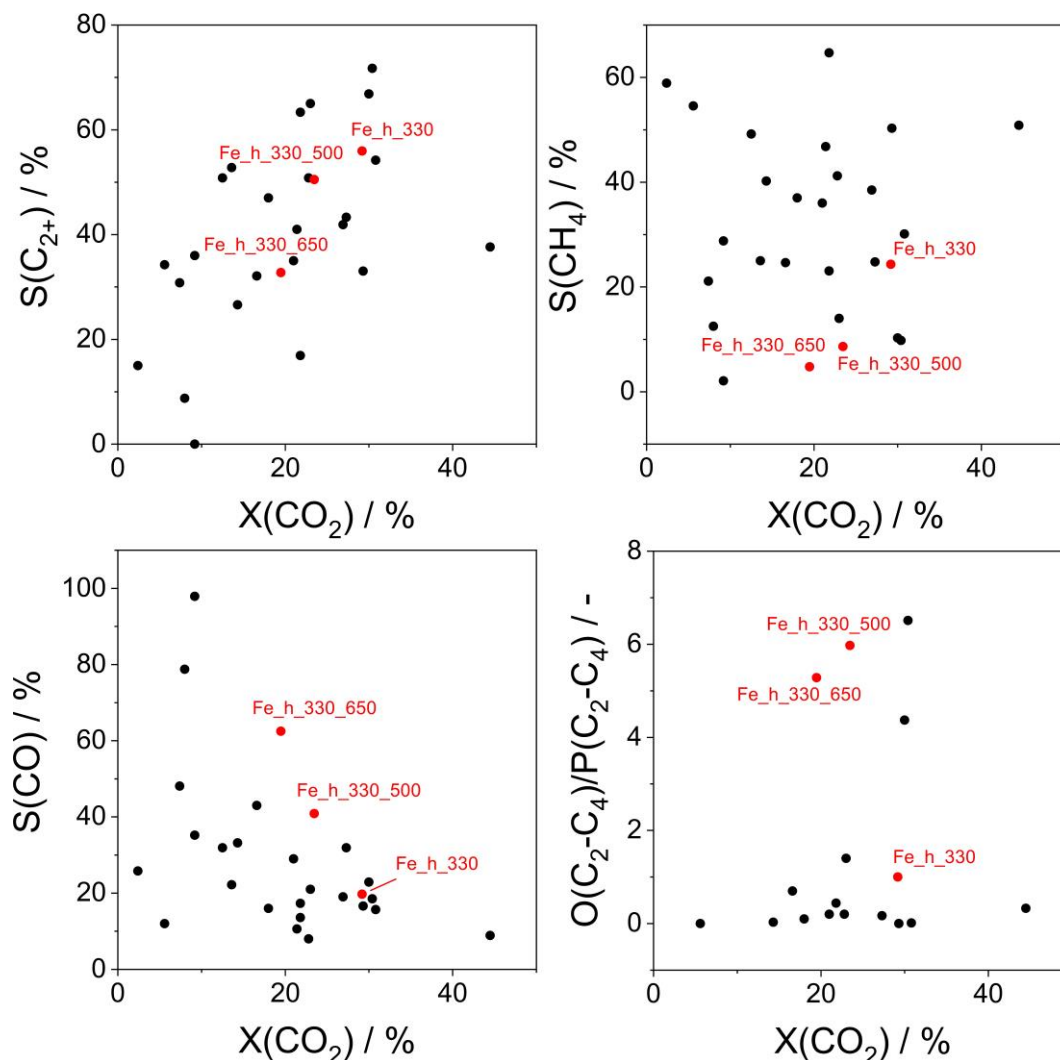
Figure 4.7.   Selectivity-conversion values obtained in the present study (red dots) and reported in literature (black dots) over Fe-based non-supported and non-doped materials. More experimental details related to the latter materials are provided in Table A.1.

4.1.4   Long-term stability catalytic test

A long-term stability test was conducted with magnetite-containing catalysts at 300 °C over about 95 h. Most samples showed stable performance for the whole time of the experiment

(Figure 4.8). The CO_2 conversion level was between 0.20 and 0.30 depending on the sample tested. The C_{2+} hydrocarbons selectivity increased with time on stream over Fe_h_330, while a decrease in the selectivity to CH_4 was observed. The corresponding values at the end of the experiment are 0.60 and 0.16, respectively, at the degree of CO_2 conversion of about 0.28. The Fe_h_330_650 sample initially showed low selectivity to CH_4 of about 0.05, but it increased drastically up to about 0.25 after 40 h on stream. It could be assumed that the catalyst went through some structural and chemical changes. The methane selectivity over the Fe_h_330_500 sample was about 0.05 during the whole time of the test, while the C_{2+}-hydrocarbons selectivity was 0.40. The olefin/paraffin ratio within C_2-C_4 hydrocarbons was 6.0. Generally, no meaningful difference in the catalytic performance between the screening and long-term stability tests at 300 °C could be determined. No deactivation of the catalyst is seen even after 95 h on-stream.
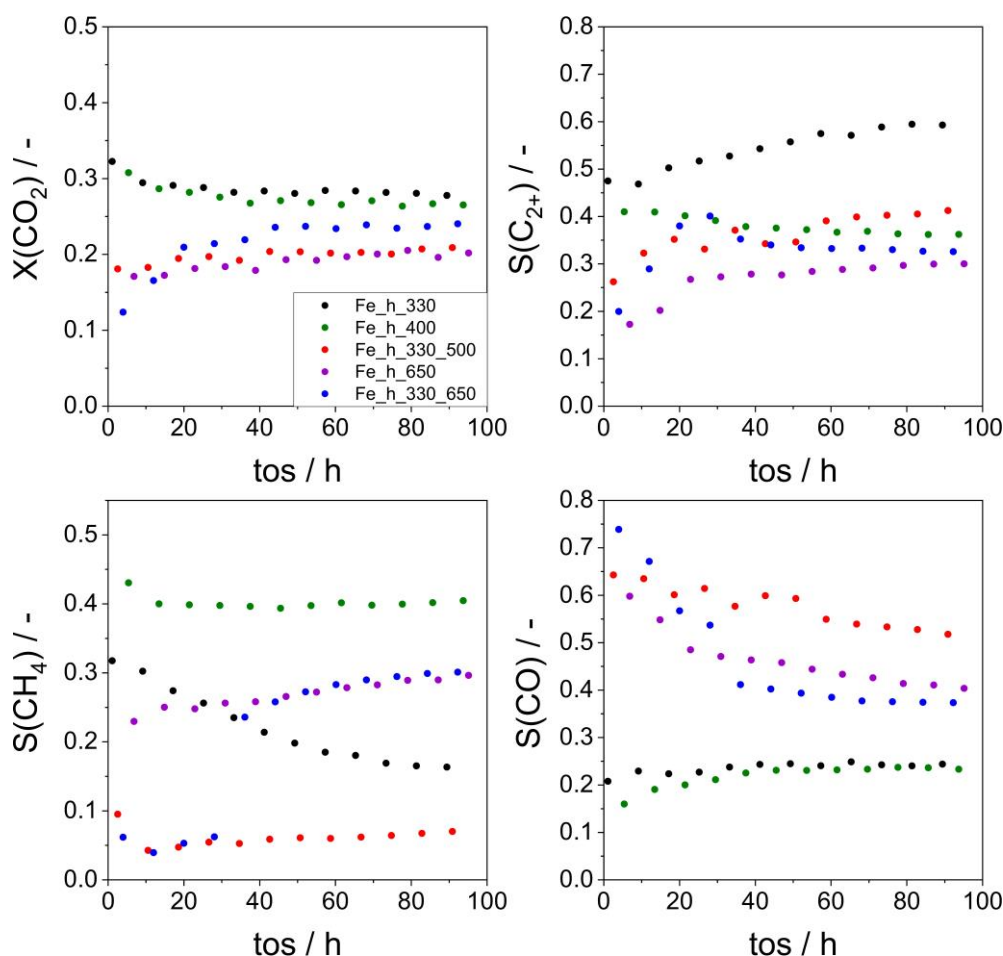

Figure 4.8. On-stream profiles of CO_2 conversion and product selectivity in CO_2 hydrogenation over magnetite-containing catalysts. Reaction conditions: total pressure: 15 bar, reaction feed: CO_2:H_2:N_2 = 1:3:0.3, GHSV: 1170 mL/g_{cat}/h, reaction temperature: 300 °C, catalyst amount: 300 mg.

4.1.5 Mechanistic scheme of CO_2 conversion into reaction products

To derive mechanistic insights into the effect of differently composed magnetite-containing catalysts on product formation, catalytic tests were conducted at 300 °C and different degrees of CO_2 conversion. To this end, catalyst amount was varied, while the total feed flow rate was fixed. The determined selectivity-conversion relationships are given in Figure 4.9. It should be emphasized that the catalytic data presented were obtained after achieving a steady-state operation.
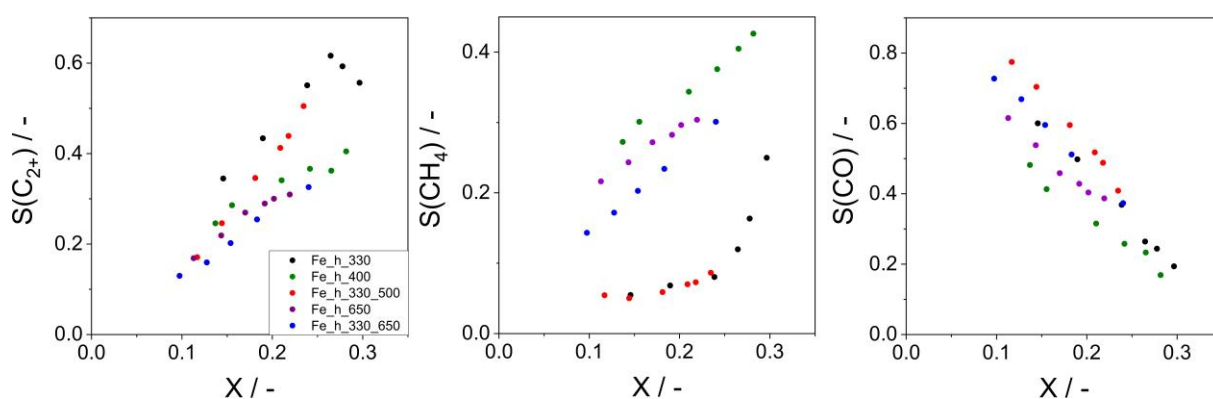
Figure 4.9.   Selectivity-conversion relationships obtained over magnetite containing catalysts. Reaction conditions: total pressure: 15 bar, reaction feed: CO_2:H_2:N_2 = 1:3:0.3, GHSV: 1170-35100 mL/g_{cat}/h, reaction temperature: 300 °C.

A decrease in CO selectivity with rising CO_2 conversion was established for all catalysts. The selectivity to C_{2+}-hydrocarbons, on the contrary, increases. The extrapolation of these data to zero CO_2 conversion would give a non-zero value for CO selectivity but, on the other hand, a zero value for C_{2+}-hydrocarbons selectivity. This dependence suggests that CO is a primary product of CO_2 conversion and formed through the RWGS reaction. CO is further hydrogenated to C_{2+}-hydrocarbons via classical CO-FTS. Based on the present results, hydrocarbons do not seem to be formed directly from CO_2.

The rate of C_{2+}-hydrocarbons formation is affected by the kind of catalyst tested as concluded from the slope of the dependence of C_{2+}-hydrocarbons selectivity on CO_2 conversion. From a kinetic point of view, the steepness of the slope reflects the reaction rate: the steeper the slope, the higher the formation rate is. On this ground, the Fe_h_330 and Fe_h_330_500 catalysts have the highest rate, while the Fe_h_330_650 catalyst possesses the lowest rate. The latter catalyst does not considerably differ from the Fe_h_400 and Fe_h_650 catalysts in this regard.

With respect to the $O(C_2-C_4)/P(C_2-C_4)$ ratio, all the tested catalysts could be divided into two groups. The Fe_h_330 and Fe_h_330_500 catalysts possessing the highest rate of C_{2+}-hydrocarbons formation produce as well the highest amount of olefins as reflected by the higher $O(C_2-C_4)/P(C_2-C_4)$ ratio in a wide range of CO_2 conversion (Figure 4.10). As olefins are regarded to be the primary products in the CO-FTS [72], it can be assumed that the Fe_h_330 and Fe_h_330_500 catalysts possess suppressed ability for secondary hydrogenation of unsaturated hydrocarbons to paraffins. This assumption is indirectly supported by the results related to CH_4 formation discussed below.
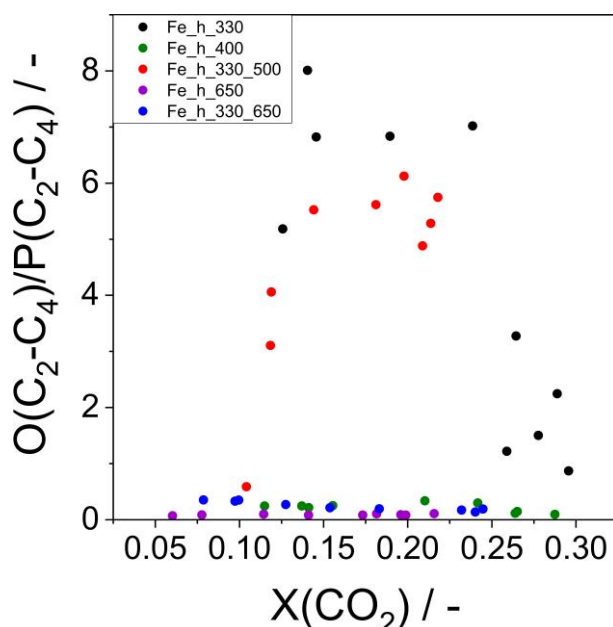
Figure 4.10. The effect of CO_2 conversion on the $O(C_2-C_4)/P(C_2-C_4)$ ratio over different magnetite-containing catalysts. Reaction conditions: total pressure: 15 bar, reaction feed: $CO_2:H_2:N_2 = 1:3:0.3$, GHSV: 1170-35100 mL/g_{cat}/h, reaction temperature: 300 °C.

The effect of CO_2 conversion on the selectivity to CH_4 also depends on the kind of catalyst applied. The selectivity over Fe_h_650, Fe_h_400 and Fe_h_330_650 increases with rising CO_2 conversion (Figure 4.9). This result suggests that methane is formed through secondary CO hydrogenation. However, the direct methanation of CO_2 cannot be completely neglected, but plays a less significant role in comparison with the CO hydrogenation route as concluded from a close-to-zero methane selectivity at zero level of CO_2 conversion. On the other hand, no prominent effect of CO_2 conversion on CH_4 selectivity over Fe_h_330 and Fe_h_330_500 could be established up to 0.25 CO_2 conversion. The selectivity value stays below 0.10. A similar value should also be at zero degree of CO_2 conversion. Therefore, this undesired product is formed directly from CO_2 over Fe_h_330 and Fe_h_330_500 catalysts below 0.25 CO_2

conversion. In addition to this route, another pathway of CH_4 formation occurs at degrees of CO_2 conversion higher than 0.25. The selectivity to methane increases drastically over Fe_h_330 catalyst above this conversion degree. The increase occurs along with a decrease in the selectivity to C_{2+}-hydrocarbons. Therefore, it could be assumed that higher hydrocarbons are converted to CH_4 probably through hydrogenolysis reaction [54]. This reaction starts to play a prominent role after the concentration of higher hydrocarbons achieved a certain level.

Based on the above discussion, the following reaction scheme of CO_2 conversion into various reaction products over magnetite containing catalysts could be proposed (Figure 4.11). CO is the primary product and formed directly from CO_2 over all the catalysts. C_{2+}-hydrocarbons are formed through further hydrogenation of CO and participation in chain-growth reaction. CH_4 is formed through three different ways. The selectivity through direct CO_2 methanation is always present at a level of about 0.05-0.08. The other two routes are CO hydrogenation and hydrogenolysis of C_{2+}-hydrocarbons. The impact of these different routes of CH_4 formation is affected by the catalyst composition.
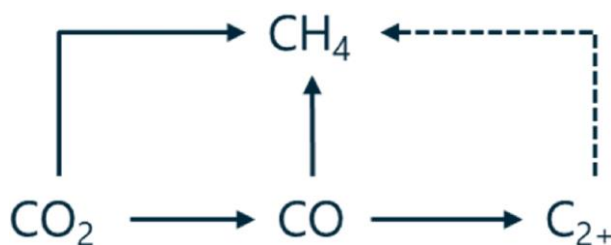
Figure 4.11. Pathways of CO_2 conversion into different reaction products.

4.1.6 Reaction-induced changes in catalyst composition

To investigate how the phase composition of differently composed magnetite-containing catalysts changes under CO_2-FTS conditions, Mössbauer spectroscopic analysis was conducted with spent materials after about 95 h on stream at 300 °C. 300 and 50 mg of spent catalysts were selected for the characterization. This allowed to check if the phase composition is homogeneously distributed along the catalyst bed as 50 mg samples represent the first 1/6 upstream layer of the 300 mg samples. The obtained spectra are given in Figure A.1, while the corresponding quantitative analysis of phase compositions is presented in Table 4.4. Assuming that the first 50 mg of 300 mg (first 1/6 upstream layer) spent sample has the same composition as 50 mg spent sample, it is possible to estimate the composition of the last 250 mg of 300 mg (5/6 downstream layer) spent sample. Hereby, the content of each individual iron containing phase in the 50 mg spent catalyst was subtracted from the corresponding content in the 300 mg

spent catalyst. The obtained difference is the content of the iron-containing phases in the remaining 5/6 down-stream layer. On this basis, the content of each phase was calculated in the first 1/6 upstream part and 5/6 downstream layers and is given in Figure 4.12.

Table 4.4. Composition (wt. %) of spent (50 or 300 mg) catalysts after long-term stability test according to Mössbauer spectroscopy as well as calculated composition of 5/6 downstream 300 mg catalyst bed. Reaction condition: total pressure: 15 bar, reaction feed: $CO_2:H_2:N_2 = 1:3:0.3$, total feed flow 5.85 mL/min, reaction temperature: 300 °C.

Catalyst	Fe_3O_4 / %	Fe / %	FeO / %	Fe_3C / %	Fe_5C_2 / %
Full catalyst bed (300 mg spent)					
Fe_h_330	80.2	-	-	4.9	14.9
Fe_h_400	89.2	-	-	2.9	7.9
Fe_h_330_500	72.2	1.6	-	-	26.3
Fe_h_650	74.7	12.6	-	2.5	10.2
Fe_h_330_650	36.5	4.3	-	-	59.2
1/6 upstream catalyst bed (50 mg spent)					
Fe_h_330	12.4	-	-	-	87.6
Fe_h_400	82.8	-	-	4.9	12.4
Fe_h_330_500	5.0	-	-	-	95.0
Fe_h_650	53.2	3.3	-	7.0	36.5
Fe_h_330_650	8.8	3.6	-	-	87.6
5/6 downstream catalyst bed					
Fe_h_330	93.7	-	-	5.9	0.4
Fe_h_400	90.5	-	-	2.5	7.0
Fe_h_330_500	85.6	1.9	-	-	12.5
Fe_h_650	79.0	14.4	-	1.6	5.0
Fe_h_330_650	42.0	4.4	-	-	53.6

The discussion starts with the consideration of the results obtained for the first 1/6 upstream catalyst layer. In comparison with the fresh catalysts, the content of metallic Fe strongly decreased even though the content of H_2 in the reaction feed is three times higher than CO_2. Apart from the Fe_h_400 catalyst, the content of Fe_3O_4 also significantly decreased. Likewise, FeO present in the fresh Fe_h_330_650 and Fe_h_650 catalysts is not present in their spent counterparts. The decrease in the content of the above-mentioned phases is associated with their conversion mainly into Fe_5C_2 and to a lesser extent into Fe_3C. The transformation occurs

47

through their reaction with CO produced from CO_2 in the thin upstream layer of the catalyst bed. The content of Fe_5C_2 in the spent Fe_h_330, Fe_h_330_500, and Fe_h_330_650 samples is above 85%, while the corresponding fraction in the spent Fe_h_400 and Fe_h_650 catalysts is only 12 and 37%. The Fe_3C phase was not identified in the spent Fe_h_330, Fe_h_330_500 and Fe_h_330_650 catalysts. The content of this phase in the spent Fe_h_400 and Fe_h_650 catalysts is 5 and 7%, respectively. As the C/Fe ratio is lower in Fe_3C than in Fe_5C_2 and the former phase could be detected only in samples containing relatively low amount of Fe_5C_2 (below 20%), it could be assumed, that Fe_3C is formed first under CO_2-FTS conditions and then transformed into Fe_5C_2.
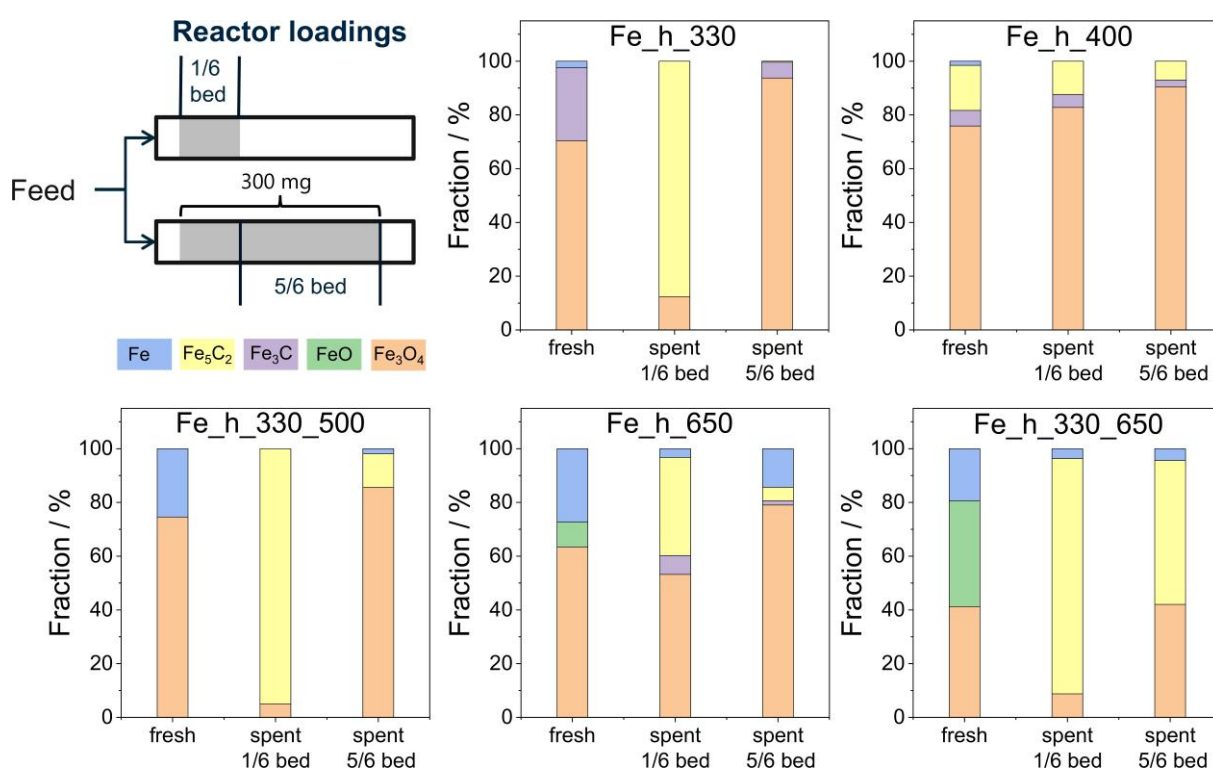
Figure 4.12. Fraction of different iron-containing phases according to Mössbauer spectroscopic analysis of fresh and spent (after CO_2 hydrogenation tests with 300 or 50 mg over 95 h on stream at 300 °C and total feed flow of 5.85 mL/min) catalysts. 1/6 bed represents 50 mg samples and 5/6 is the subtraction of 50 mg composition from the 300 mg catalyst layer. The corresponding values are given in Table 4.4.

The discussion continues with the consideration of the results obtained for the downstream 5/6 catalyst layer of 300 mg bed. In comparison with the fresh catalyst composition, the amount of metallic Fe decreased in all samples tested. Contrarily, the fraction of Fe_3O_4 in spent catalysts increased in comparison with the fresh materials and the first 1/6 upstream layer. The FeO phase present in fresh Fe_h_330_650 and Fe_h_650 is not found in the corresponding spent samples.

The differently prepared materials show different ability to generate/stabilize Fe_5C_2 under the CO_2-FTS conditions. The highest fraction of the Fe_5C_2 phase was established in the spent Fe_h_330_650 sample. The corresponding fresh catalyst contains the highest amount of the FeO phase and the lowest amount of the Fe_3O_4 phase. The former phase seems to play an important role for the formation of Fe_5C_2 presumably due to its easier transformation into metallic Fe, which reacts with CO forming iron carbides. The low content of metallic Fe and the absence of the FeO phase in fresh Fe_h_330 and Fe_h_400 catalysts are likely the reasons for the low fraction of Fe_5C_2 in their spent counterparts. Fe_3C can be converted both into Fe_3O_4 and Fe_5C_2. For the fresh Fe_h_330 and Fe_h_400 catalysts containing iron carbides, a decrease in the fraction was detected in their spent counterparts because of their oxidation to Fe_3O_4 during the CO_2-FTS reaction.

Based on the above discussion, it could be concluded that steady-state catalyst composition is not only affected by the initial composition but is also non-homogeneously distributed along the catalyst bed. However, the strength of these changes is influenced by the initial catalyst composition. The most important transformations are related to the concentration of the Fe_3O_4 and iron carbide phases. The content of the former phase in the 5/6 downstream layer of the 300 mg catalyst bed is comparable to that in their fresh counterparts but is meaningfully lower than in the 1/6 upstream layer. Contrarily, iron carbide phases are mostly located in the upstream part of the catalyst bed and their fraction in the downstream layer is significantly lower. Based on the analysis of the composition of upstream and downstream parts of the catalyst bed, the catalysts could be ordered with respect to their ability to generate/stabilize iron carbide phases as follows: Fe_h_330_650 > Fe_h_400 > Fe_h_650 > Fe_h_330_500 > Fe_h_330.

Taking into account the distinctive kinetics of reduction and oxidation of fresh materials with H_2 and CO_2, respectively (Table 4.3), it could be expected that metallic Fe should be the dominant phase under steady-state CO_2-FTS conditions. However, the content of this phase in spent samples is lower than in their fresh counterparts. This should be connected to the transformation of metallic Fe into iron carbides through the reaction with CO produced from CO_2 over Fe_3O_4. As mentioned above, Fe_3O_4 and FeO could also be transformed into iron carbides. Therefore, the rate of iron carbides formation should be greater than the rate of their reduction by H_2 and oxidation of metallic Fe by CO_2. This conclusion, however, seems to be valid only for a thin upstream catalyst layer. Except for the Fe_h_400 catalyst, the first 1/6 upstream part of all other catalysts contain predominantly (above 40%) iron carbides.

Nevertheless, their content decreases downstream along the catalyst bed, while the content of Fe_3O_4 and metallic Fe increases to larger and minor extents, respectively. The concentration of the metallic Fe in the 5/6 downstream part as well as in the 1/6 upstream part is considerably lower than in the fresh materials. Therefore, (re)oxidation should be accounted for the reaction-induced transformations downstream along the catalyst bed. As was shown earlier, CO_2 is a very weak oxidant (Table 4.3) and its concentration decreases along the catalyst bed (Figure 4.13a). Therefore, this reactant cannot be responsible for the mentioned changes.
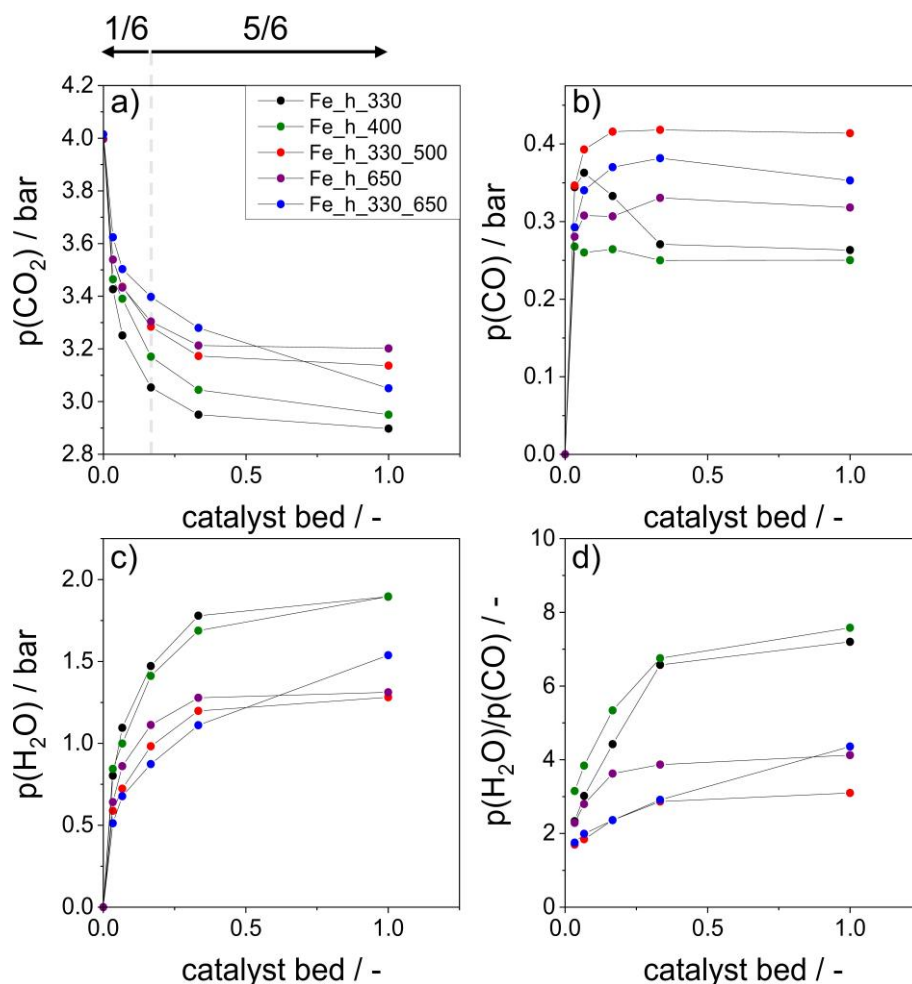
Figure 4.13. Spatial profiles of partial pressure of (a) CO_2, (b) CO, and (c) H_2O as well as (d) the ratio of partial pressure of H_2O to that of CO. Presented values are obtained over $10-300$ mg catalyst mass loads based on molar fraction of particular product and overall pressure after CO_2 hydrogenation tests over 95 h on stream at 300 °C and total feed flow of 5.85 mL/min.

The only plausible oxidant is water produced during CO_2 conversion into CO and hydrocarbons (CH_4 and C_{2+}). As the developed catalysts possess different activity for the conversion of CO_2, different partial pressures of water are achieved in the same parts of catalyst bed for different catalysts (Figure 4.13c). This is also relevant for the partial pressure of CO, which is responsible

50

for the formation of iron carbides (Figure 4.13b). The ratio of the H_2O/CO partial pressures depends on the catalyst applied and increases along the catalyst bed (Figure 4.13d). Therefore, the competition between the rates of CO and H_2O formation as well as of Fe/FeO_x reduction/carburization with CO and of oxidation of Fe/Fe_xC_y with H_2O will establish catalyst steady-state composition and consequently catalyst performance.

4.1.7 Structure-activity-selectivity relationships

According to various previous studies [8] and the present results, the conversion of CO_2 into higher hydrocarbons begins with the RWGS step forming CO. This intermediate is hydrogenated further into CH_4 and C_{2+}-hydrocarbons. The former is produced additionally directly from CO_2. As all products are generated over different iron-containing phases, it is highly important to elucidate factors affecting the formation of these phases and the role they play in the course of CO_2 hydrogenation.

It is generally accepted that Fe_3O_4 is the active phase in the RWGS reaction [29]. To check if CO_2 conversion is affected by redox properties of magnetite, the relationship between the overall rate of CO_2 conversion obtained from CO_2-FTS experiments and the initial rate of Fe_3O_4 reduction with H_2 determined from TGA experiments was plotted (Figure 4.14). A clear tendency can be seen. The CO_2 conversion rate increases with an increase in the rate of Fe_3O_4 reduction. As the RWGS reaction determines the CO_2 conversion in CO_2-FTS, this dependency could be understood when considering one of the proposed mechanisms of the RWGS reaction described in section 1.3.3. It has been repeatedly reported that CO_2 activation over metal oxide catalysts is improved in the presence of oxygen vacancies. According to the redox mechanism, when CO_2 reacts with such defect, gas-phase CO is formed, while the remaining oxygen refills the vacancy to yield lattice oxygen [6, 72]. In a second step, H_2 removes the formed oxygen species in form of water and, thus, recovers oxygen vacancy. Therefore, catalysts with high reducibility should be active in CO_2 conversion into CO through the RWGS reaction.

The discussion proceeds with the consideration of factors affecting product selectivity. It is generally accepted that iron carbides are required for chain-growth reactions. To prove this statement, the selectivity to C_{2+}-hydrocarbons obtained in experiments using 300 or 50 mg of a catalyst was related to the content of iron carbides in the corresponding amounts of spent catalysts (Figure A.5). However, no meaningful correlation could be established. The explanation could be that the catalysts significantly differ in their activity and as it was already shown above: the conversion strongly affects the product selectivity (Figure 4.9). Thus, this

result could be followed from the inconsistent catalyst activity leading to different degrees of CO_2 conversion.
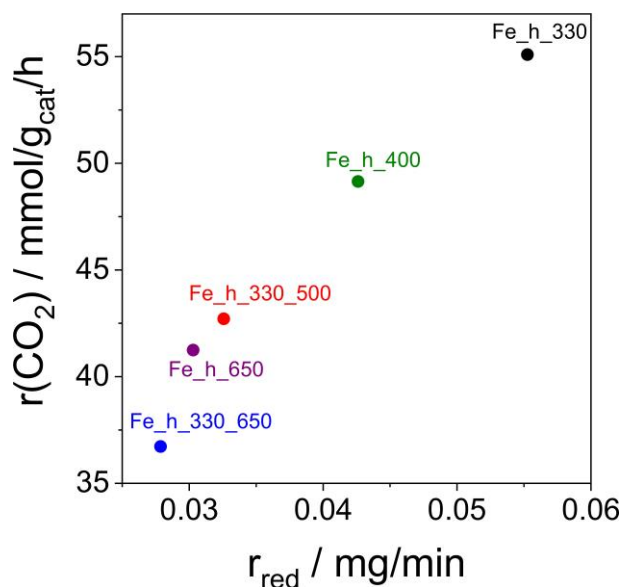

Figure 4.14. The overall CO_2 conversion rate obtained at 300 °C and CO_2 conversion of about 0.12 versus the initial rate of reduction of fresh catalyst with H_2.

For a proper comparison of catalysts in terms of product selectivity, the latter should be compared at a similar degree of CO_2 conversion. For all catalysts, it was possible to achieve the degree of CO_2 conversion of about 0.20 when using 20, 50, 300, 300, or 300 mg of Fe_h_330, Fe_h_400, Fe_h_330_500, Fe_h_330_650, or Fe_h_650 and the total feed flow of 5.85 mL/min. The phase composition in these catalyst amounts after about 95 h on stream was determined by means of Mössbauer spectroscopy. When now relating product selectivity with the steady-state catalyst composition, some correlation could be established. For all catalysts, an increase in the fraction of iron carbides (Fe_3C and Fe_5C_2) leads to an increase in the selectivity to C_{2+}-hydrocarbons (Figure 4.15a). The deviation of the data point corresponding to the content of iron carbides of about 60% could be explained when considering the influence of metallic Fe on product selectivity. This phase apparently enhances the methane formation. The selectivity to methane over the Fe_h_330_550, Fe_h_330_650 and Fe_h_650 catalysts increases with rising content of metallic Fe (Figure 4.15c). It should also be mentioned that the slope of the relationship of methane selectivity on CO_2 conversion increases with an increase in the fraction of metallic Fe (Figure 4.9b). Therefore, it could be assumed that metallic Fe participates in CO hydrogenation to CH_4. Furthermore, this reaction pathway is almost hindered over the Fe_h_330 catalyst, where no metallic Fe was detected. The highest methane selectivity was reached over the Fe_h_400 sample, where metallic Fe is not present. This spent catalyst,

on the other hand, contains the highest amount of Fe_3O_4 and the lowest content of iron carbides. A positive correlation between the methane selectivity and the fraction of Fe_3O_4 was obtained, although one data point corresponding to Fe_h_330_500 catalyst deviates from this dependence (Figure 4.15b). This catalyst possesses the lowest ability for consecutive CO hydrogenation as concluded from the dependence of this selectivity on CO_2 conversion. Therefore, an optimal ratio between the content of Fe_3O_4 and Fe_xC_y phases is required for efficient production of higher hydrocarbons from CO_2.
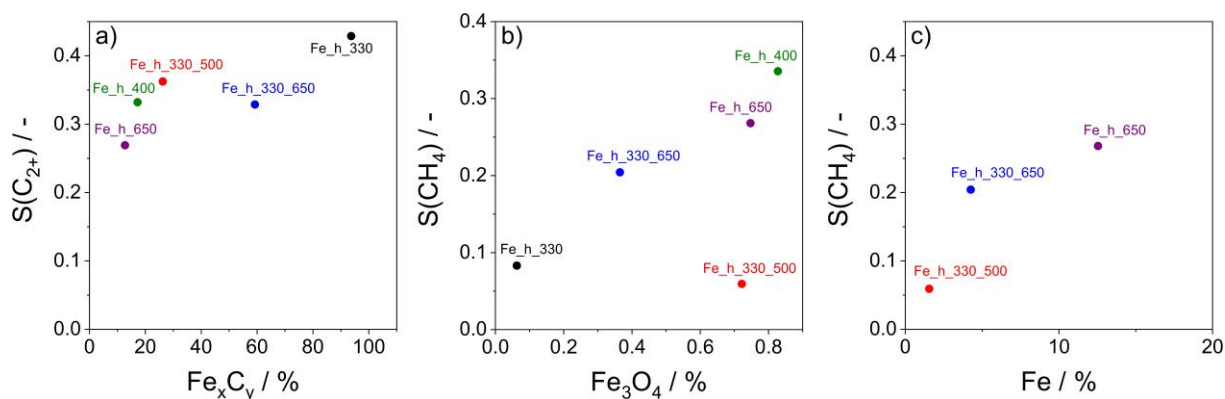

Figure 4.15. The effects of (a) Fe_xC_y, (b) Fe_3O_4 and (c) Fe content in spent catalysts on the selectivity to C_{2+}-hydrocarbons and CH_4. The selectivity values were obtained at 300 °C and CO_2 conversion of about 0.20. The fractions of the corresponding phases were determined in catalyst amounts required to achieve this conversion degree.

4.1.8 Summary

Iron (II) oxalate dihydrate is a suitable precursor for the production of iron-containing catalysts with easily tunable fractions of Fe_3O_4, FeO, Fe_5C_2, Fe_3C and metallic Fe. Such catalysts can be applied for CO_2-FTS experiments without any preceding reductive treatment. Thus, it was possible to unambiguously understand the reaction-induced transformations of iron-containing phases under reaction conditions. For instance, it was determined that the FeO is easily converted to Fe_5C_2 supposedly because of its fast reduction to metallic Fe, which reacts with CO forming iron carbides. Therefore, the steady-state composition depends on the initial composition and could be tuned through the controlled catalyst preparation. Moreover, for the first time, it was shown that the steady-state composition is not uniform and changes along the catalyst bed. Iron carbides are formed directly in the up-stream located catalyst layer. Their fraction decreases along the catalyst bed upon progressing CO_2 conversion, while the content of Fe_3O_4, on the other hand, increases.

The potential of the approach applied for catalyst synthesis is clearly demonstrated when comparing the catalytic performance results with the one reported in literature. The developed catalysts showed catalytic performance on the level with top 3 best-performing state-of-the-art non-promoted Fe-based materials in terms of suppressed selectivity to methane and enhanced olefin/paraffin ratio within C_2-C_4 hydrocarbons. In addition, reaction pathways leading from CO_2 to CO, CH_4 and higher hydrocarbons were elucidated. CO is proved to be the main primary product participating in further hydrogenation to CH_4 and higher hydrocarbons. Two additional ways of CH_4 formation were established, which are direct CO_2 methanation and hydrogenolysis of higher hydrocarbons.

Due to the above-mentioned non-homogeneous composition distribution, catalysts at similar conversion degrees should be compared in order to establish the catalytic performance – composition relationships. To this end, a positive correlation between the fraction of iron carbides and the selectivity to C_{2+}-hydrocarbons was determined. Metallic Fe was found to be responsible for CO hydrogenation to CH_4. Beside catalyzing the RWGS reaction, Fe_3O_4 is also active in CO_2 hydrogenation towards CH_4, however, with the former being the main reaction. The reducibility of the catalyst was proved to be an important factor affecting the overall CO_2 conversion rate. The higher the reducibility, the higher the CO_2 consumption rate is.

4.2 Hematite-containing catalysts

The advantage of hematite-containing catalysts is that the phase composition (α-/γ-Fe_2O_3) and the crystallite size of the materials prepared through iron (II) oxalate dihydrate decomposition could be thoroughly controlled. This allows to investigate the effects of the crystallite size and the initial composition on catalyst activity and product selectivity in the course of CO_2 hydrogenation.

4.2.1 General characterization of fresh catalysts

Two series of hematite-containing catalysts were synthesized with the variation of α-Fe_2O_3 crystallites in single-phase materials (Series 1) and with the variation of α-/γ-Fe_2O_3 phase ratio in mixed-phase materials (Series 2). For the preparation of catalysts both commercial and in-house synthesized iron (II) oxalate dihydrate were used. The obtained XRD patterns of these materials are characteristic for the monoclinic iron oxalate dihydrate (Figure 4.16a). However, the intensities of several individual reflexes are clearly different, which could implicate that the iron (II) oxalate dihydrates differ in their morphology. For this reason, SEM analysis was conducted, which showed that in-house synthesized ferrous oxalate dihydrate consists of 5 μm particles with plain grains assembled in 20 μm agglomerates (Figure 4.17a). The commercial iron (II) oxalate dihydrate is composed of 30 μm particles with cracked grains assembled in 120 μm agglomerates (Figure 4.17b).
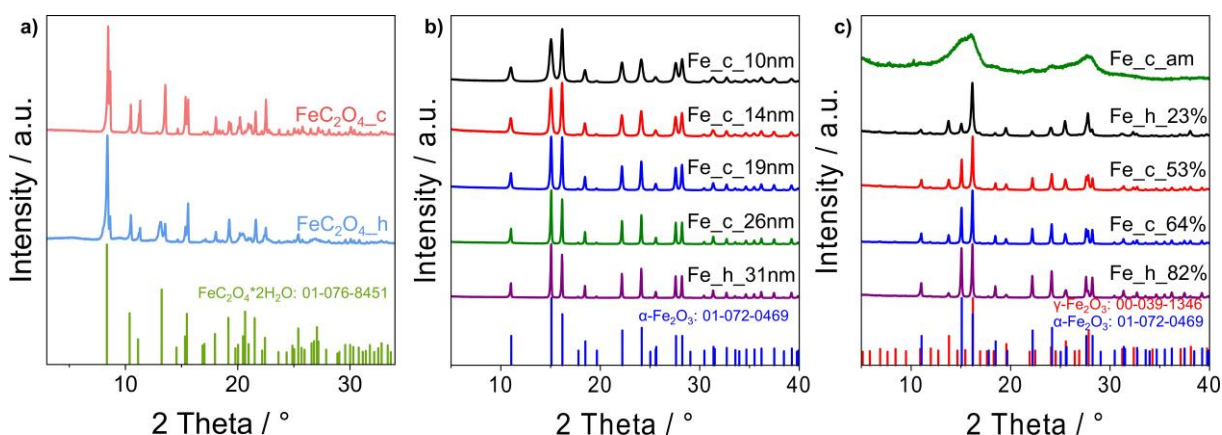
Figure 4.16. XRD patterns of (a) iron (II) oxalate dihydrate precursors (commercial ($FeC_2O_4\_c$) and in-house synthesized ($FeC_2O_4\_h$)) (b) fresh Fe_2O_3 catalysts from Series 1 and (c) fresh Fe_2O_3 catalysts from Series 2.

The content of Fe in the applied iron (II) oxalates corresponds to the theoretical value in iron (II) oxalate dihydrate as determined from X-ray fluorescence analysis (Table 4.5). The main

impurities in the materials are Si and P with the corresponding weight amounts of about 0.3 and 0.1 wt%. Any other contaminants are present in neglectable quantities.

Table 4.5. The results of X-ray fluorescence analysis of commercial and in-house synthesized iron oxalate dihydrate.

/ wt%	Si	P	Ca	Mn	Fe	Cu	Ni	Zn	Ru	Y	La
FeOx_c	0.271	0.0708	255.8 ppm	563.0 ppm	28.687	0	117.8 ppm	40.0 ppm	0.1 ppm	0	0
FeOx_h	0.290	0.110	410.9 ppm	0	28.758	38.1 ppm	0	0	0	12.7 ppm	152.4 ppm

The specific surface area (S_{BET}) of fresh catalysts is listed in Table 4.6. The highest value of 358 m^2/g was established for the sample prepared at 180 °C, while the catalyst treated at 330 and afterwards at 650 °C has the lowest value of 12 m^2/g. Generally, a decrease in the specific surface area correlates with an increase in catalyst synthesis temperature. Therefore, it is likely that high temperature treatment causes sintering of crystallites and decrease in the surface area.

Table 4.6. Phase composition (wt%) determined from XRD, the crystallite size (coherent scattering region (CSR)) of α-Fe_2O_3 and γ-Fe_2O_3 and specific surface area (S_{BET}) and the temperature of maximal rate of reduction of Fe_2O_3 to Fe_3O_4 ($T_{max}(Fe_2O_3$ to $Fe_3O_4)$) as determined from H_2-TPR profiles of fresh samples.

Catalyst	α-Fe_2O_3 / wt%	γ-Fe_2O_3 / wt%	CSR (α-Fe_2O_3) / nm	CSR (γ-Fe_2O_3) / nm	S_{BET} / m^2/g	$T_{max}(Fe_2O_3$ to $Fe_3O_4)$ / °C
Series 1						
Fe_c_10nm	100	-	10	-	95	379.3
Fe_c_14nm	100	-	14	-	40	409.3
Fe_c_19nm	100	-	19	-	38	422.6
Fe_c_26nm	100	-	26	-	34	425.8
Fe_h_31nm	100	-	31	-	12	464.1
Series 2						
Fe_h_23%	23.2	76.8	18	14	63	354.9
Fe_c_53%	52.5	47.5	21	15	50	380.0
Fe_c_64%	64.0	36.0	39	30	17	388.1
Fe_h_am	Amorphous Fe_2O_3		-	-	358	400.0
Fe_h_82%	82.0	18.0	37	25	21	439.5

The phase composition of the fresh catalysts was identified by XRD analysis (Figure 4.16b) and is given in Table 4.6 together with the crystallite size of each phase determined. All catalysts from Series 1 are single-phase materials containing only the hematite phase (α-Fe_2O_3). However, the materials differ in the crystallite size of this phase. It depends on the calcination temperature, at which they were prepared. The higher the treatment temperature, the higher the crystallite size is. Hematite samples synthesized at 300, 400, 500, 600 or 650 °C consists of crystallites of 10, 14, 19, 26 or 31 nm, respectively.
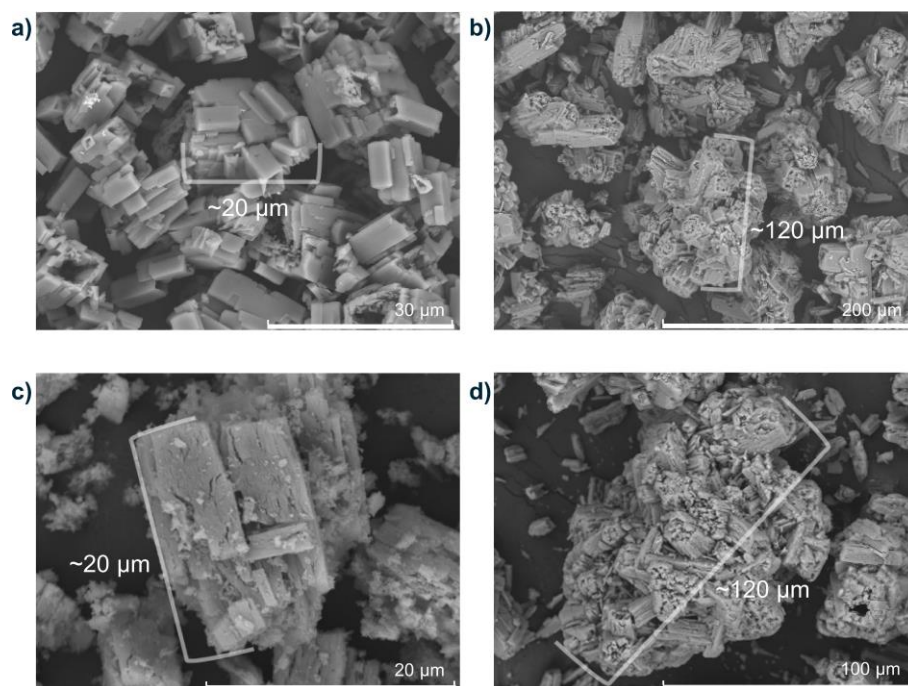

Figure 4.17. SEM images of (a) in-house synthesized and (b) commercial iron (II) oxalate dihydrates as well as fresh Fe_2O_3 prepared on their basis (c) Fe_h_23% and (d) Fe_c_53%.

Except for X-ray amorphous Fe_c_am sample, all other catalysts from Series 2 consist of a mixture of hematite (α-Fe_2O_3) and maghemite (γ-Fe_2O_3) phases with the fraction of the former phase being between 23 and 82% (Figure 4.16c). As a general tendency, the higher the fraction of hematite phase, the larger the crystallite size both of α-Fe_2O_3 and γ-Fe_2O_3 are. It could be explained by the higher temperature of synthesis of catalysts containing higher amount of hematite phase. In all crystalline materials, the hematite phase consists of larger crystallites than the maghemite phase. Interestingly, Fe_h_23% and Fe_c_53% synthesized at the same temperature but from different ferrous oxalate dihydrate precursors have different compositions. This result indicates that these two precursors might have different reactivity in the decomposition reaction supposedly because of different particle size of ferrous oxalates

(Figure 4.17a,b). Ferrous oxalate dihydrate decomposes forming solid-phase FeO and gas-phase CO and CO_2 [114]. Hermanek et al. [110] stated that the rate of the oxidation of CO by oxygen, when the decomposition proceeds in air, has an important influence on the forming composition. From a thermodynamical viewpoint, the product of FeO oxidation by oxygen should be α-Fe_2O_3, but if the transport of the oxidizing agent is slow and the oxidation of CO proceeds slowly, Fe_3O_4 is formed as an intermediate phase, which is then converted into γ-Fe_2O_3, for the reason of the similarity of the lattice structures. Prolonged thermal treatment of γ-Fe_2O_3 leads to the conversion of γ-Fe_2O_3 into α-Fe_2O_3.

According to the SEM analysis, the fresh Fe_2O_3 catalysts inherit the size and the shape of the precursor agglomerates, which are 20 μm for the samples derived from the in-house synthesized oxalate and 120 μm for the catalysts prepared from the commercial precursor (Figure 4.17c,d). However, the particles, from which these agglomerates are composed, became cracked and even fractured. These particles are porous inside and consist of nanometer sized Fe_2O_3 crystallites as determined from XRD analysis.

4.2.2   Redox properties of fresh catalysts

Reducibility of fresh catalysts was analyzed by H_2-TPR measurements. The profiles of H_2 flow collected at the reactor outlet are shown in Figure 4.18. A decrease in the flow reflects hydrogen consumption due to the reduction of iron oxides. Typically, the reduction comprises three consecutive steps, $Fe_2O_3 \rightarrow Fe_3O_4 \rightarrow FeO \rightarrow Fe$, with the first well-distinguished step happening at lower temperature and the two other overlapping steps taking place at higher temperature [125-127]. This overall reduction sequence seems to be appliable for the present materials. A small peak preceding the first reduction step of amorphous iron (III) oxide catalyst could be seen in the H_2-TPR profile. This sample possesses the highest specific surface area. Therefore, it could be assumed that this small peak of H_2 consumption is devoted to the reduction of surface oxygen from Fe_2O_3 and other consumption peaks taking place at higher temperatures are ascribed to the bulk reduction processes.

The reducibility of single-phase catalysts from Series 1 is affected by the crystallite size of α-Fe_2O_3, as could be concluded from the corresponding H_2-TPR profiles. The lower the crystallite size, the easier the reduction progresses (Figure 4.18a). The content of γ-Fe_2O_3 phase, which coexists with α-Fe_2O_3 in mixed-phase catalysts from Series 2, seems to be an important descriptor for the reducibility. There is an increase in the temperature of maximal reduction rate of Fe_2O_3 to Fe_3O_4 with rising fraction of γ-Fe_2O_3 (Figure 4.18b). The specific surface area could

be excluded as the only factor influencing the reducibility because the Fe_c_64% catalyst has lower area than the Fe_h_82% catalyst but possesses higher reducibility. This result can be explained when considering the following factors. From a crystallographic point of view, γ-Fe_2O_3 has a structure similar to Fe_3O_4, which is the product of the first step of Fe_2O_3 reduction. Both phases belong to the cubic crystal system and comprises cubic close-packed oxygen lattice. The only difference in the structures is the presence of iron vacancies in the octahedral sites and the absence of Fe^{2+} cations in the γ-Fe_2O_3 phase [128]. Therefore, no significant structural changes occur upon the reduction of maghemite to magnetite, which is favored kinetically. On the other hand, α-Fe_2O_3 is crystallized in the trigonal crystal system with the hexagonal close-packed oxygen lattice, where two thirds of the octahedral sites are occupied by Fe^{3+} cations. The hexagonal close-packed oxygen lattice should be transformed to the cubic close-packed oxygen lattice during the reduction process. Thus, the reduction of hematite to magnetite should progress slower than the reduction of maghemite.
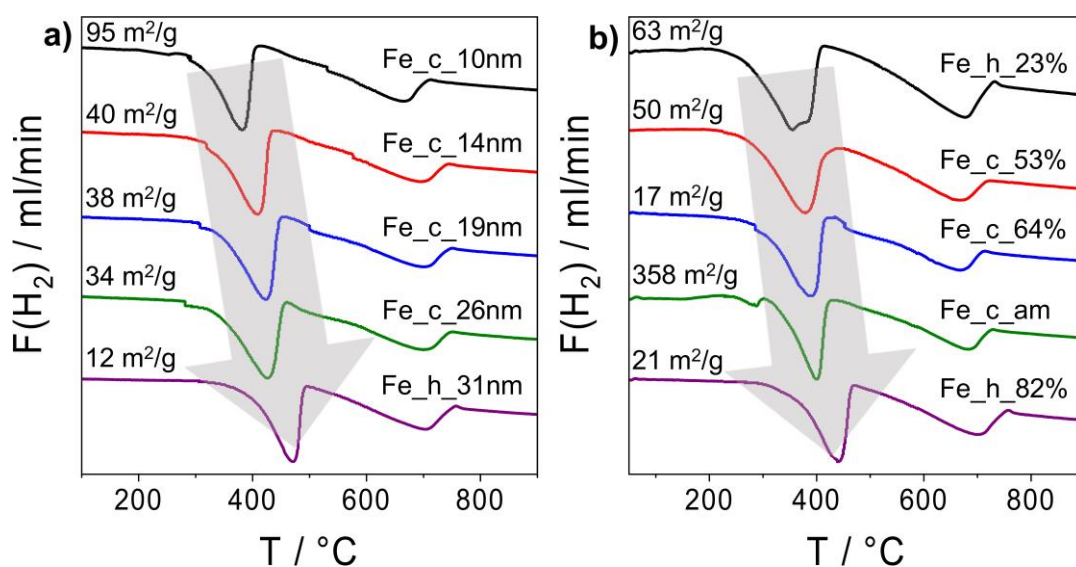

Figure 4.18. Profiles of H_2 flow at the reactor outlet upon H_2-TPR (5 vol% H_2 in Ar) of fresh catalysts from (a) Series 1 and (b) Series 2.

Even though the Fe_c_am catalyst has the highest specific surface area, it showed almost the lowest reducibility (Figure 4.18b). It could be due to the reason that the phase transformation from the amorphous Fe_2O_3 to the crystalline α-Fe_2O_3 may happen during the H_2-TPR experiment. Such transformation was described in many studies during the thermal treatment of amorphous iron (III) oxide materials in nitrogen, air, or vacuum [110, 129]. As was mentioned in the above-discussed H_2-TPR experiments with the mixed-phase Fe_2O_3, the reduction of hematite proceeds slower than the reduction of maghemite.

The reducibility of single-phase α-Fe$_2$O$_3$ fresh catalysts was also studied under isothermal conditions. For this reason, *in situ* TGA experiments were conducted at 300 °C using H$_2$ (H$_2$:He = 1:1) as a reducing agent. A decrease in the weight was observed for all catalysts with rising time on H$_2$ stream up to about 2.5 h (Figure 4.19). The decrease is associated with the removal of lattice oxygen from iron oxide(s) by H$_2$ in form of water. Two consecutive steps are well distinguished in the TGA profiles. At a selected temperature of 300 °C, the reduction of hematite proceeds through a two-step mechanism: in this case no FeO intermediate is formed (equations 4.6-4.7). The fact that the TGA profiles reached a plateau on H$_2$ stream could mean that iron oxides were completely converted into metallic iron. The total weight loss in the TGA experiments is in agreement with the theoretical values calculated based on the mass of the tested catalysts and the stoichiometry of the reduction processes.
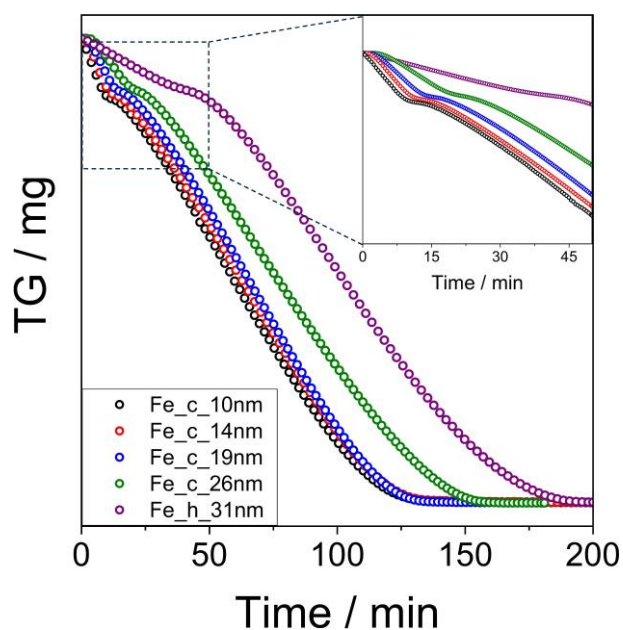

Figure 4.19. TGA profiles obtained at 300 °C upon reduction of single-phase α-Fe$_2$O$_3$ samples from Series 1 with H$_2$ (H$_2$:He = 1:1).

$$Fe_2O_3 + 3H_2 \rightleftarrows 2Fe + 3H_2O \tag{4.6}$$

$$Fe_3O_4 + 4H_2 \rightleftarrows 3Fe + 4H_2O \tag{4.7}$$
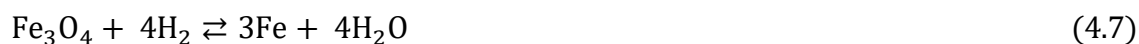
From a kinetic viewpoint, the steepness of the slope of the TGA profiles reflects the reaction rate: the steeper the slope, the higher the reduction rate is. Single-phase catalysts with low crystallite sizes and, consequently, high specific surface areas possess high reduction rate. Unfortunately, the presence of two consecutive reduction steps does not allow to perform a reliable quantitative analysis using a linear part of a curve as it was done for magnetite-

containing catalysts. However, qualitatively the order of catalyst reducibility is in a good agreement with the one derived from the H_2-TPR experiments.

4.2.3 CO₂-FTS performance of single-phase α-Fe₂O₃ catalysts

A long-term stability test (for about 110 h on stream) with the catalysts from Series 1 was carried out at 300 °C and 15 bar after preceding reductive treatment at 400 °C in a H_2:N_2 = 1:1 flow at the same pressure for 2 h. A slight decrease in CO_2 conversion with rising time on stream was observed. Unstable behavior of catalysts in terms of olefin/paraffin ratio within C_2-C_4 hydrocarbons during the experiment could also be seen. On the contrary, the selectivity to CO, CH_4 and C_{2+}-hydrocarbons was determined to be stable for the whole time of the experiment (Figure 4.20).
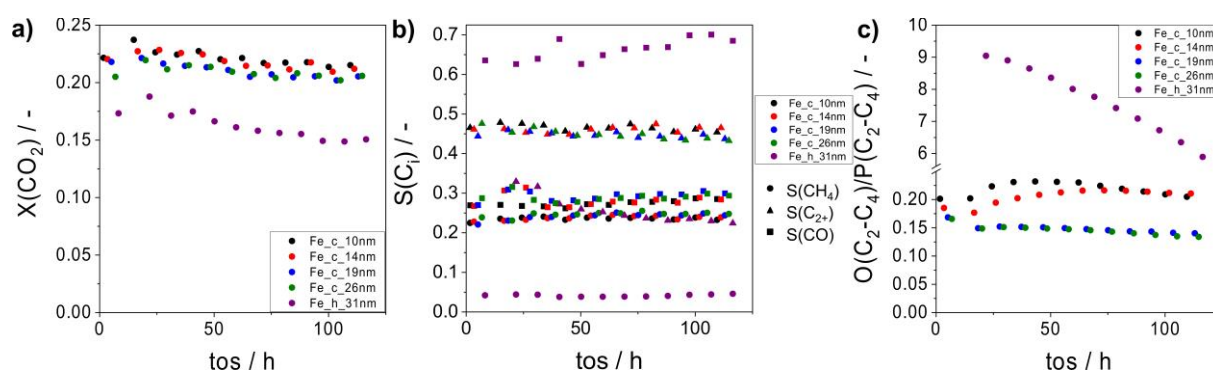

Figure 4.20. On-stream profiles of (a) CO_2 conversion, (b) product selectivity and (c) the olefin/paraffin ratio within C_2-C_4 hydrocarbons in CO_2 hydrogenation over catalysts from Series 1. Reduction conditions: temperature: 400 °C, H_2:N_2 = 1:1. Reaction conditions: total pressure: 15 bar, reaction feed: CO_2:H_2:N_2 = 1:3:0.3, GHSV: 7020 mL/g_{cat}/h, temperature: 300 °C, catalyst amount: 50 mg.

The conversion, selectivity and chain growth probability values at the end of the experiment are shown in Figure 4.21. The Fe_h_31nm catalyst strongly deviates from other materials in terms of CH_4 selectivity, which is below 0.05 at the degree of CO_2 conversion of about 0.15. The corresponding selectivity values for other samples are above 0.2, however, at a higher level of CO_2 conversion. Moreover, the olefin/paraffin ratio within C_2-C_4 hydrocarbons obtained over Fe_h_31nm is significantly higher, when comparing it with other samples, i.e., 5.9 vs. 0.2. Except for the mentioned catalyst, the selectivity to CO, CH_4 and C_2-C_4 paraffins over other materials increases with an increase in the crystallite size of fresh α-Fe₂O₃ (Figure 4.21). On the contrary, the selectivity to C_{5+}-hydrocarbons and light olefins (C_2-C_4) along with the chain growth probability and the O(C_2-C_4)/P(C_2-C_4) ratio decreases. Importantly, the degree of CO_2 conversion stays almost unchanged.
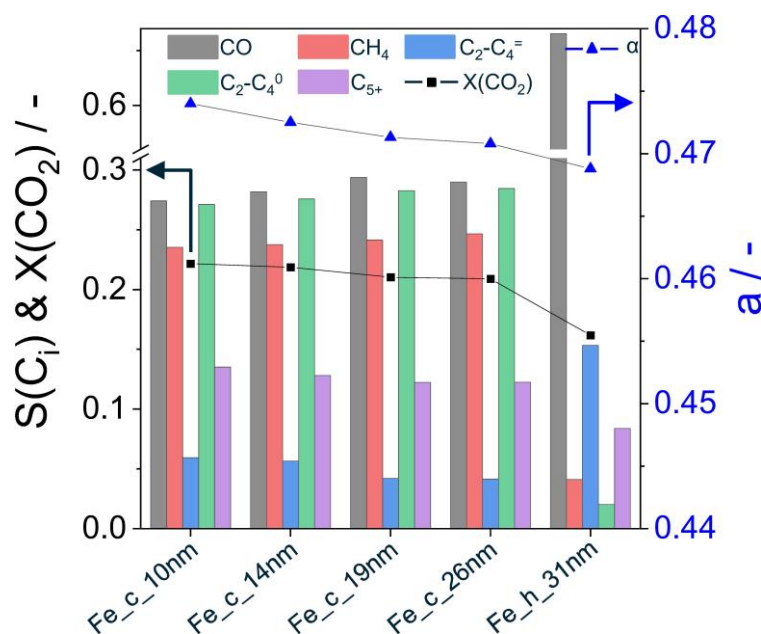
Figure 4.21. Catalytic performance of single-phase α-Fe_2O_3 catalysts from Series 1 in CO_2-FTS after 110 h on stream. Catalyst reduction conditions: temperature: 400 °C, reduction feed: H_2:N_2 = 1:1. Reaction conditions: total pressure: 15 bar, reaction feed: CO_2:H_2:N_2 = 1:3:0.3, GHSV: 7020 mL/g_{cat}/h, temperature: 300 °C, catalyst amount: 50 mg.

To derive further insights into the above-described crystallite-size effect on CO_2-FTS, the selectivity-conversion relationships for CO, CH_4 and C_{2+}-hydrocarbons were obtained. For this reason, long-term stability experiments were conducted at different levels of CO_2 conversion obtained through varying the catalyst amount (600, 300, 100, 50, 20, 10 mg) while keeping the feed flow constant. The obtained relationships are shown in Figure 4.22. For all catalysts, there is a decrease in the selectivity to CO with rising CO_2 conversion. Except for the Fe_h_31nm catalyst, a small increase in the selectivity was determined over other samples when the CO_2 conversion reached the level of 0.23. The reason for this increase is the ununiform spatial distribution of steady-state iron-containing species along the catalyst bed (considered in details in section 4.2.5). Briefly, the higher degree of CO_2 was achieved by using the higher catalyst amount. The content of Fe_3O_4 favoring the formation of CO prevails in the steady-state composition of a bigger mass loading. The extrapolation of CO selectivity to zero CO_2 conversion would lead to a non-zero high (above 0.9) value. This is the fingerprint that CO is a primary product of CO_2 conversion through the RWGS reaction. On the contrary, there is an increase in the C_{2+}-hydrocarbons selectivity with an increase in the conversion (Figure 4.22b). When extrapolating the selectivity to C_{2+}-hydrocarbons to zero CO_2 conversion, a zero value is obtained. This dependence implicates that C_{2+}-hydrocarbons are secondary products and are formed through further CO hydrogenation, as the selectivity to the latter product decreases with

rising CO_2 conversion. A small decrease in the selectivity to C_{2+}-hydrocarbons was obtained when the CO_2 conversion reached 0.23 level, which is not associated with the hydrogenolysis reactions as it was described in section 4.1.5 for the magnetite-containing catalysts. A non-homogeneous spatial distribution of steady-state catalytically active phases should be responsible for the decrease as will be discussed in detail below after considering the phase composition of spent catalysts.
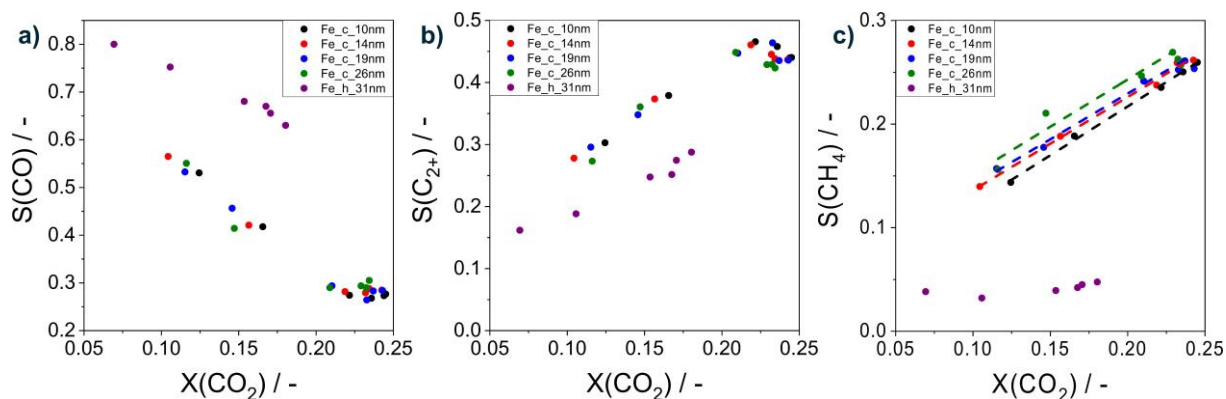

Figure 4.22. Selectivity-conversion relationships obtained for single-phase α-Fe_2O_3 catalysts from Series 1. Reduction conditions: temperature: 400 °C, H_2:N_2 = 1:1. Reaction conditions: total pressure: 15 bar, reaction feed: CO_2:H_2:N_2 = 1:3:0.3, GHSV: 585-35100 mL/g_{cat}/h, temperature: 300 °C.

CO is also converted to methane as can be concluded from increasing CH_4 selectivity with rising CO_2 conversion (Figure 4.22c). The direct hydrogenation of CO_2 into CH_4 also takes place. This conclusion is made on the experimental fact that a non-zero CH_4 selectivity value is obtained at zero level of CO_2 conversion. Generally, except for the absence of hydrogenolysis leading to the methane formation, the pathway of CO_2 hydrogenation into various reaction products corresponds to the one determined for the magnetite-containing catalysts described and discussed in section 4.1.5 (Figure 4.11). Within the two pathways of CH_4 formation over Fe_2O_3 catalysts, the direct CO_2 methanation prevails over Fe_h_31nm but with a low reaction rate, while CO hydrogenation to CH_4 dominates over other materials. This conclusion is based on the analysis of the slope of the selectivity-conversion dependence for this product. There is a small increase in selectivity to CH_4 over Fe_h_31nm with an increase in conversion of CO_2, i.e., the slope of this dependence is close to zero. On the other hand, the slope determined for other samples is noticeably greater than zero and the values differ from each other (from 0.94 to 0.83). This result implies that the Fe_h_10nm, Fe_h_14nm, Fe_h_19nm and Fe_h_26nm materials show different activity towards CH_4 formation through CO hydrogenation. The catalysts should also differ in the rates of direct CO_2 methanation because they have different

values of the methane selectivity at zero CO_2 conversion. This value grows from 0.03 to 0.07 with an increase in the crystallite size of fresh α-Fe_2O_3 catalysts from 10 to 26 nm. Therefore, the established dependence opens a possibility for controlling this undesired pathway through tuning hematite crystallite size.

Interestingly, the direct CO_2 methanation can also be regulated through catalyst reduction temperature before the CO_2-FTS reaction. While the selectivity to C_{2+}-hydrocarbons is not affected by the reduction temperature, a clear effect on the selectivity to CH_4 and CO could be seen as exemplified for Fe_c_10nm in Figure 4.23a-c. The corresponding values increase and decrease with a decrease in the reduction temperature from 400 to 300 °C. Thus, lower pretreatment temperature leads to a higher contribution of direct methanation to the overall methane formation and lower rate of CO hydrogenation to CH_4 as could be concluded from the slopes of the obtained relationships. It should be noted that these effects become less significant with increasing crystallite size and almost disappears for the Fe_c_26nm catalyst (Figure 4.23i).
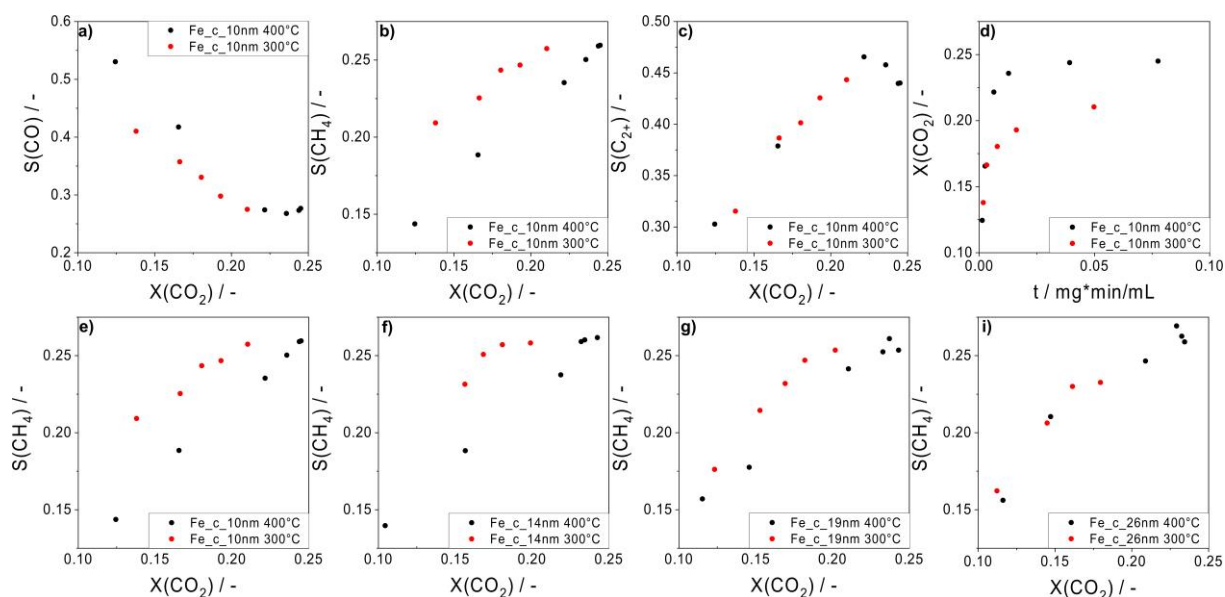
Figure 4.23. (a)-(d) Selectivity-conversion and conversion-contact time relationships obtained for one selected single-phase hematite containing catalyst prereduced at different temperatures. (e)-(i) Selectivity-conversion relationships obtained for single-phase catalysts (Series 1) prereduced at different temperatures. Reduction conditions: temperature: 300 or 400 °C, H_2:N_2 = 1:1. Reaction conditions: total pressure: 15 bar, reaction feed: CO_2:H_2:N_2 = 1:3:0.3, GHSV: 585-35100 mL/g_{cat}/h, temperature: 300 °C.

4.2.4 CO_2-FTS performance of mixed-phase α-/γ-Fe_2O_3 catalysts

Long-term stability experiments with mixed-phase α-/γ-Fe_2O_3 catalysts from Series 2 were carried out at 300 °C over about 110 h on-stream at 15 bar and different contact time after

preceding catalyst reduction (H_2:N_2 = 1:1) at 400 °C at 15 bar for 2 h (Figure 4.24). The decrease in CO_2 conversion with time on-stream was observed over Fe_c_am, Fe_c_53% and Fe_c_64%. Contrarily, they showed stable performance in terms of product selectivity. On the other hand, a decrease in the selectivity to C_{2+}-hydrocarbons was identified for Fe_h_23% and Fe_h_82% catalysts with time on-stream accompanied with a growth in the selectivity to CO (Figure 4.24). They reached a steady-state operation after 70 h on-stream. The selectivity to CH_4, on the other hand, remained stable and is meaningfully lower (0.05) than that determined for Fe_c_am, Fe_c_53% and Fe_c_64% (0.25) catalysts. In addition, Fe_h_23% and Fe_h_82% materials showed much higher $O(C_2$-$C_4)/P(C_2$-$C_4)$ ratio (6.3) in comparison with three catalysts derived from commercial ferrous oxalate dihydrate (0.15).
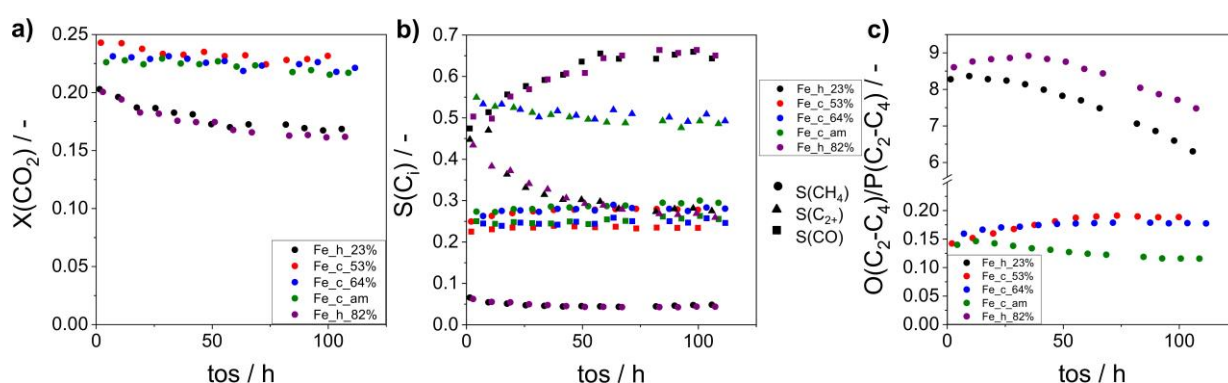

Figure 4.24. On-stream profiles of (a) CO_2 conversion, (b) product selectivity, and (c) the olefin/paraffin ratio within C_2-C_4 hydrocarbons in CO_2 hydrogenation over mixed-phase α-/γ-Fe_2O_3 catalysts from Series 2. Reduction conditions: temperature: 400 °C, H_2:N_2 = 1:1. Reaction conditions: total pressure: 15 bar, reaction feed: CO_2:H_2:N_2 = 1:3:0.3, GHSV: 7020 mL/g_{cat}/h, temperature: 300 °C, catalyst amount: 50 mg.

The obtained selectivity-conversion relationships for CO, CH_4 and C_{2+}-hydrocarbons are given in Figure 4.25. Generally, the scheme of CO_2 conversion into these products is similar to that determined for the single phase catalysts from Series 1. Shortly, CO is the main primary product taking part in further hydrogenation processes. There are two pathways of methane formation: (i) through hydrogenation of CO and (ii) through direct CO_2 methanation. Interestingly, the methane selectivity obtained over Fe_h_23% and Fe_h_82% catalysts is around 0.05 even at the degree of CO_2 conversion of 0.22 and practically does not depend on the conversion degree. Their catalytic performance in this regard is similar to that of the Fe_h_31nm catalyst from Series 1, which was also prepared from the in-house synthesized iron (II) oxalate dihydrate. Three other catalysts derived from commercial iron (II) oxalate dihydrate showed a constant apprising tendency for the selectivity to methane with rising conversion of CO_2. Therefore, the

CO_2 direct hydrogenation pathway over catalysts prepared from home-synthesized precursor is significantly hindered in comparison with other materials from this series (Figure 4.25c).
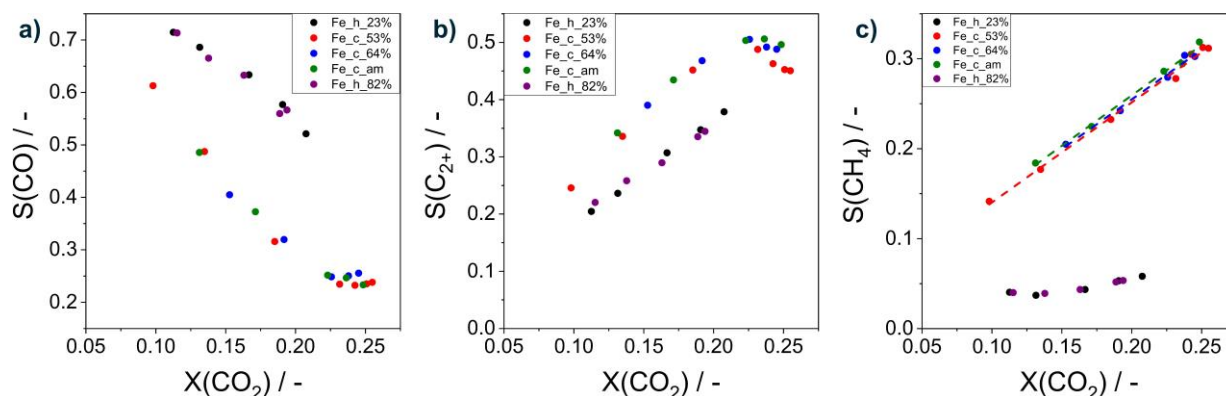
Figure 4.25. Selectivity-conversion relationships obtained for mixed-phase α-/γ-Fe_2O_3 catalysts from Series 2. Catalyst reduction conditions: temperature: 400 °C, H_2:N_2 = 1:1. Reaction conditions: total pressure: 15 bar, reaction feed: CO_2:H_2:N_2 = 1:3:0.3, GHSV: 585-70200 mL/g_{cat}/h, temperature: 300 °C.

Notably, both the slope of selectivity-conversion dependency for CH_4 and the values of methane selectivity at zero CO_2 conversion differ for catalysts prepared from commercial precursor. A correlation might be established between the primary CH_4 selectivity and the reducibility of fresh catalysts. The higher the reducibility of fresh samples, the lower the impact of direct CO_2 methanation route into overall CH_4 formation (Figure 4.26a).

Figure 4.26. The dependence of (a) intercept at zero value of CO_2 conversion and (b) slope derived from the linear extrapolation of selectivity to CH_4 – CO_2 conversion relationship from the temperature of Fe_2O_3 reduction to Fe_3O_4 determined by H_2-TPR.

This conclusion is in accordance with previous results for the catalysts from Series 1, for which a similar dependence was obtained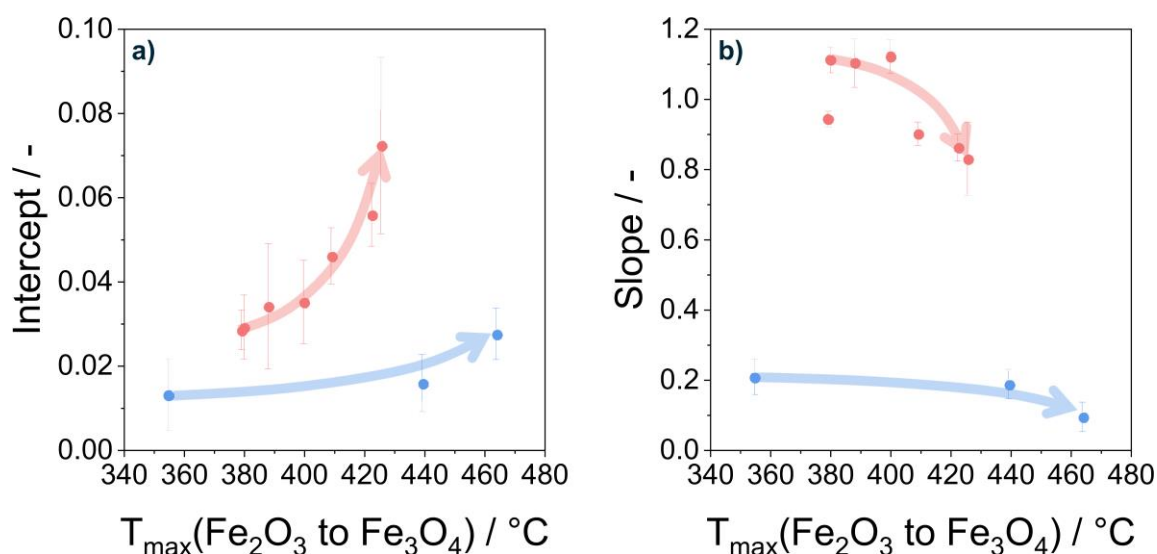. Therefore, not the crystallite size itself, but the reducibility of catalysts is an important parameter, which can help to manage the direct CO_2 methanation route. CO hydrogenation to CH_4 is as well affected by the reducibility of fresh catalysts, but the tendency is opposite to the one established for the direct methanation route. The higher the reducibility, the higher the impact of CO hydrogenation to CH_4 into overall methane formation (Figure 4.26b). Although, this effect is less pronounced than direct CO_2 hydrogenation to CH_4.
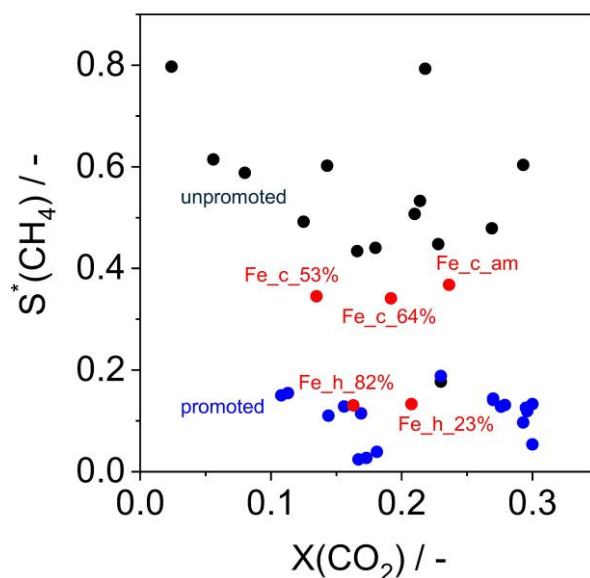
Figure 4.27. CH_4 distribution among all hydrocarbons (without accounting CO) versus CO_2 conversion obtained over the present Fe_2O_3 catalysts (red dots) and previously reported non-supported unpromoted (black dots) or promoted non-supported (blue dots) Fe-based materials with top 10% performance. The corresponding references and additional previously tested catalysts with higher CH_4 selectivity are shown in Figure A.6.

To benchmark the developed catalysts in terms of the undesired CH_4 formation against the best performing state-of-the-art Fe-based catalysts, Figure 4.27 was prepared. It shows the selectivity to methane without accounting CO, i.e. the methane distribution among all hydrocarbons, as CO potentially could be separated from the outlet gases and reused in the large-scale production process. The data for the methane distribution over unpromoted and promoted catalysts were selected from the database from Q. Yang et al. [73]. The Fe_h_* materials show the selectivity to methane as low as the top 10% best-performing promoted Fe-based catalysts and remarkably outperformed all previously developed unpromoted catalysts. It should be also mentioned that despite the fact that the Fe_c_* materials produce more methane than the Fe_h_* materials, they still revealed lower selectivity comparatively to the

unpromoted reported catalysts. Therefore, the present results clearly demonstrate the potential of the approach for the preparation of unpromoted Fe_2O_3 materials with hindered selectivity to methane.

4.2.5 Reaction-induced changes in catalyst composition and its consequence on the catalytic performance

The composition of catalysts reduced at 400 °C in the same manner as before CO_2-FTS experiment was analyzed by means of XRD. The samples contain a mixture of Fe_3O_4 and Fe with the weight amount of the latter phase being between 22.4 and 55.2 wt% (Table 4.7). The content of metallic Fe in the reduced materials correlates well with the reducibility of fresh catalysts. Spent catalysts (after 110 h on-stream in CO_2-FTS at 300 °C) consist of a mixture of Fe_3O_4 and Fe_5C_2 according to Mössbauer spectroscopic data (Table 4.8). As iron carbides are formed through the reaction of metallic Fe with CO produced during the CO_2-FTS, it could be assumed that the fraction of metallic Fe in the reduced samples should correlate with the fraction of Fe_5C_2 in their spent counterparts. However, no such dependence could be established.

Table 4.7.   Catalyst composition after reductive catalyst pretreatment according to XRD. Reduction conditions: temperature: 400 °C, $H_2:N_2$ = 1:1, time: 2 h, GHSV 2340 mL/g_{cat}/h, catalyst amount: 200 mg.

Catalyst	Fe_3O_4 / wt %	Fe / wt %
Series 1		
Fe_c_10nm	54.9	45.1
Fe_c_14nm	56.6	43.4
Fe_c_19nm	56.8	43.2
Fe_c_26nm	59.5	40.1
Fe_h_31nm	77.6	22.4
Series 2		
Fe_h_23%	44.8	55.2
Fe_c_53%	55.3	44.7
Fe_c_64%	57.0	43.0
Fe_c_am	61.3	38.7
Fe_h_82%	71.4	28.6

It could be seen in Table 4.8 that like in the case of magnetite-containing samples iron carbides are non-homogeneously distributed along the catalyst bed. Its content was quantitatively identified through analyzing Mössbauer spectra of different catalyst amounts (m_i=10, 20, 50, 100 or 300 mg) loaded into individual reactors for CO_2-FTS experiments (Figure A.7, Figure A.8). The spatial distribution of the phase composition along the catalyst bed was determined by subtracting the composition obtained in the previous m_i from the following m_{i+1} catalyst amount, where m_1, m_2, m_3, m_4, and m_5 represent 10, 20, 50, 100 and 300 mg, respectively. The phase composition in the first segment of the catalyst bed is equal to the composition in m_1 (Figure 4.28).
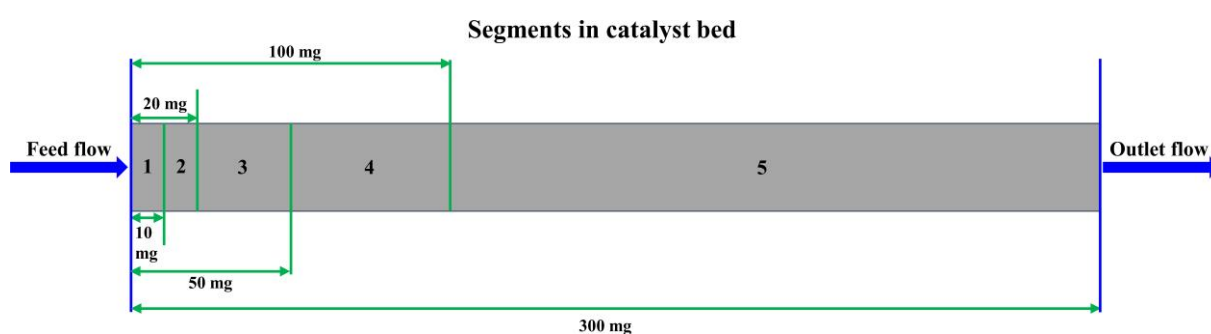

Figure 4.28. A schematic representation how the segments in the catalyst bed are defined.

Figure 4.29 represents the composition of different Fe-containing phases along the overall catalyst bed in a dimensional form ranging between 0 and 1, where 1 reflects the highest sample amount of 300 mg. All other sample amounts were normalized with respect to this amount. For all materials, it could be seen that Fe_5C_2 is created directly in the first up-stream located segment and its fraction decreases along the catalyst bed upon progressing CO_2 conversion. Contrarily, Fe_3O_4 is the dominant phase in the down-stream located layers. However, the quantitative spatial distribution of the Fe_5C_2 and Fe_3O_4 phases depends on the kind of catalyst. The catalysts derived from in-house synthesized iron (II) oxalate dihydrate possess exclusively Fe_5C_2 in the first 1/6 layer. The pure carbide layer of the catalysts synthesized from commercial iron (II) oxalate dihydrate is only 1/20. Moreover, a decrease in the fraction of Fe_5C_2 along the remaining 19/20 downstream located segments in these materials is significantly stronger than in catalysts derived from in-house synthesized precursor. The ununiformed distribution of Fe_3O_4 and Fe_5C_2 should be determined by the rates of Fe carburization with CO and oxidation of Fe/Fe_5C_2 by H_2O as well as by the rates of generation of these reaction products and CO consumption.

Table 4.8. Composition (wt %) of spent catalysts (after 110 h on-stream) in different segments based on the results of quantitative analysis of Mössbauer spectra.

Catalyst	Phase	0-10 mg	10-20 mg	20-50 mg	50-100 mg	100-300 mg
Fe_c_10	Fe_5C_2 / %	100.0	86.8	64.6	29.2	0.6
	Fe_3O_4 / %	0.0	13.2	35.4	70.8	99.4
Fe_h_31	Fe_5C_2 / %	100.0	100.0	100.0	72.8	2.6
	Fe_3O_4 / %	0.0	0.0	0.0	27.2	97.4
Fe_h_23	Fe_5C_2 / %	100.0	100.0	100.0	76.2	4.4
	Fe_3O_4 / %	0.0	0.0	0.0	23.8	95.6
Fe_c_64	Fe_5C_2 / %	100.0	80.8	33.4	18.3	4.2
	Fe_3O_4 / %	0.0	19.2	66.6	81.7	95.8
Fe_c_am	Fe_5C_2 / %	100.0	84.0	51.1	31.8	4.2
	Fe_3O_4 / %	0.0	16.0	48.9	68.2	95.8
Fe_h_82	Fe_5C_2 / %	100.0	100.0	100.0	70.4	0.6
	Fe_3O_4 / %	0.0	0.0	0.0	29.6	99.4

To understand which consequences the spatial distribution of Fe_5C_2 and Fe_3O_4 species have on product formation, segmental rates of CH_4 and C_{2+}-hydrocarbons production as well as their ratio were calculated according to equation 4.8 in the catalyst segments defined in Figure 4.28. A decrease in the formation rate of C_{2+}-hydrocarbons was established for all catalysts along the catalyst bed due to a switch from differential to integral reactor operation (Figure 4.29). The catalysts prepared from commercial iron (II) oxalate dihydrate (Fe_c_*) exhibit a higher rate in the first 1/6 catalyst segment in comparison with the materials derived from in-house synthesized iron (II) oxalate dihydrate (Fe_h_*). Therefore, iron carbide in the Fe_c_* catalysts possesses higher intrinsic activity than iron carbide in the Fe_h_* catalysts for the formation of C_{2+}-hydrocarbons. However, an opposite order of catalyst activity was established in down-stream located segments because the content of Fe_5C_2 in 5/6 down-stream layers of the Fe_c_* catalysts is very low.

$$r_j(i) = \frac{\dot{n}_i^a - \dot{n}_i^{a-1}}{m^a - m^{a-1}} \qquad (4.8)$$

where $\dot{n}$ and m represent the molar outlet flows of CH_4 or C_{2+}-hydrocarbons and catalyst amount, respectively. The superscripts a-1 or a reflect different segments of the catalyst bed. The subscript j stands for a certain segment, i.e. 1, 2, 3, or 5 as depictured in Figure 4.28.
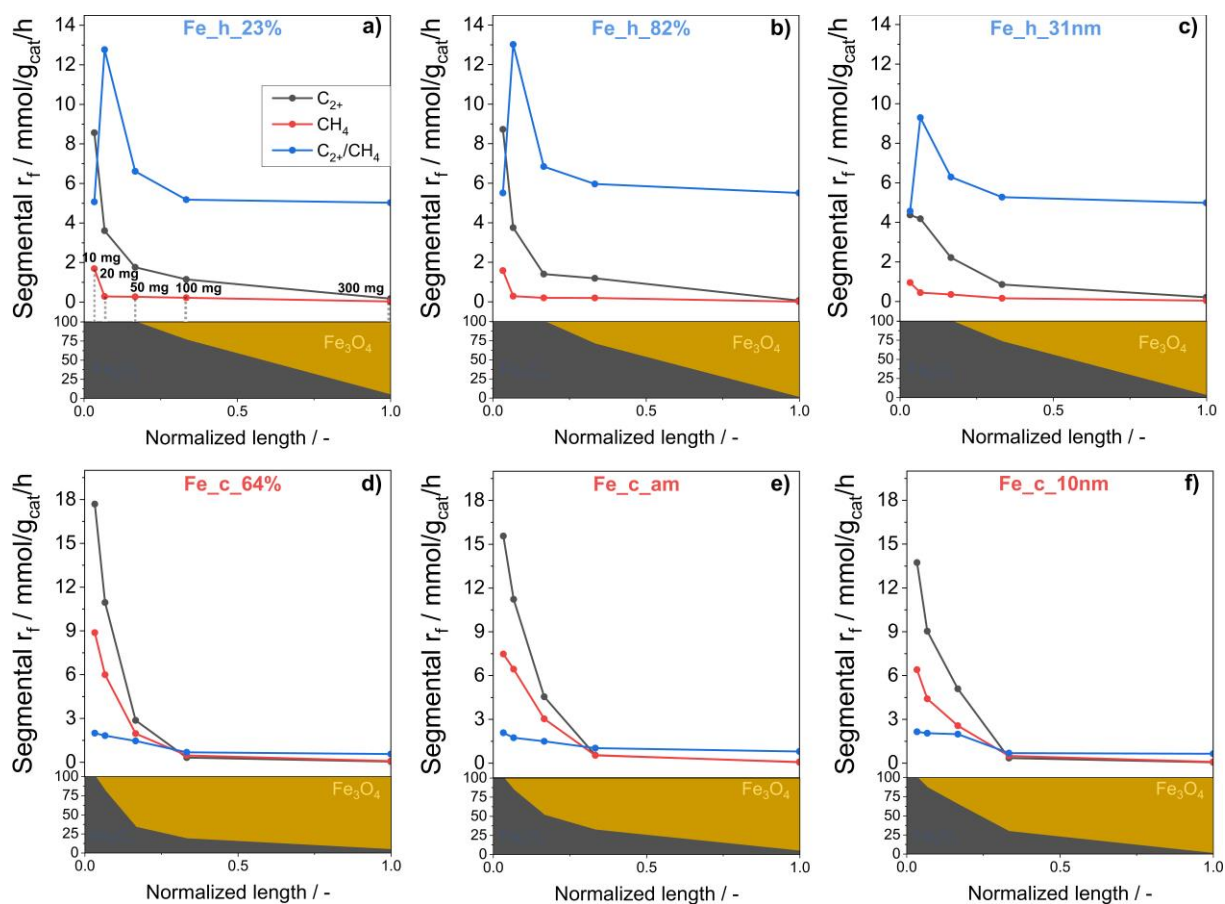
Figure 4.29. Spatial profiles of segmental formation rates of C_{2+}-hydrocarbons, CH_4 and C_{2+}-hydrocarbons/CH_4 ratio and spatial composition distribution along the catalyst bed. Presented values are obtained over 10, 20, 50, 100 and 300 mg catalyst mass loads by substitution previous mass load values from the current. Therefore, shown data represents formation rates of the specific reaction products on the catalyst bed intervals normalized to 300 mg mass load.

The Fe_c_* materials revealed higher activity towards CH_4 production in comparison with the Fe_h_* materials (Figure 4.29). The latter catalysts produce this undesired reaction product in the first 1/30 up-stream located segment, while the remaining 29/30 down-stream catalyst segment is practically not involved in the formation of methane. On the contrary, significantly larger (about 1/6) first layer of the catalyst bed of the Fe_c_* materials take part in the formation of methane.

The difference between the Fe_c_* and Fe_h_* materials become even more prominent when considering the ratio of the C_{2+}-hydrocarbons formation rate to the CH_4 formation rate. This ratio in the first layer of the Fe_c_* materials is equal to about 2 and continuously decreases to about 1 in the down-stream located segments. The corresponding values for the Fe_h_* materials are about 5. Moreover, unlike Fe_c_* catalysts, the ratio for the Fe_h_* materials has a maximum of 10-13 in the second analyzed up-stream segment (between the first 1/30 and

71

1/15 up-stream located segment). Considering that CO could potentially be easily separated from C_{2+}-hydrocarbons and reused (in comparison with CH_4), the distinguished behavior of Fe_h_* catalysts in terms of the ratio of the C_{2+}-hydrocarbons formation rate to the CH_4 formation rate is of high importance. The $r_f(C_{2+})/r_f(CH_4)$ ratio over catalysts prepared from in-house synthesized iron (II) oxalate is 2 to 7 times higher than that determined for the catalysts derived from commercial precursor.

4.2.6 Kinetic analysis of CO, H₂ and CO₂ interaction with spent catalysts

To derive mechanistic and kinetic insights into the interaction of feed components (CO_2 and H_2) as well as CO intermediate with spent catalysts (100 mg fraction) and to understand the distinctive catalytic behavior of prepared materials, pulse experiments were conducted in a temporal analysis of products reactor system. The interaction of CO_2 reactant with spent catalysts was investigated through $CO_2/Ar = 1:1$ pulse experiments at 300 °C. No CO was detected in these experiments.

Table 4.9. Micro-kinetic models applied for kinetic modeling of CO_2 adsorption and activation.

Model	Elementary step	Rate constants
1	Diffusion	D_{eff}
2	$CO_2 + * \rightarrow *-CO_2$	$k_{ads}^{eff\ a}$
	$*-CO_2 \rightarrow CO_2 + *$	k_{des}
3	$CO_2 + 2* \rightarrow *-CO + *-O$	$k_{diss}^{eff\ a}$
	$*-CO + *-O \rightarrow CO_2 + 2*$	k_{ass}^{eff}
4	$CO_2 + * \rightarrow *-CO_2$	$k_{ads}^{eff\ a}$
	$*-CO_2 \rightarrow * + CO_2$	k_{des}
	$*-CO_2 + * \rightarrow *-CO + *-O$	$k_{diss}^{eff\ a}$
	$*-CO + *-O \rightarrow *-CO_2 + *$	k_{ass}

a. Because of the correlation between the overall concentration of active sites and the rate constants of CO_2 adsorption or dissociation, only their product could be determined. They are denoted as k_{ads}^{eff} or k_{diss}^{eff}.

The kind (reversible or irreversible) of CO_2 adsorption was determined through analyzing dimensionless responses of CO_2 and Ar according to the theory of the TAP reactor [115]. The Ar response is called the standard diffusion curve. These responses were acquired through the transformation of the corresponding experimental transients using equations 3.1-3.2.

Regardless of the analyzed sample, the dimensionless CO_2 response crosses the dimensionless Ar response, and its peak maximum is below that of Ar (Figure A.9). This is a fingerprint of reversible adsorption of CO_2. On this basis, various microkinetic models (Table 4.9) were applied to describe the experimental data to identify the model, which fits the best non-transformed CO_2 responses. The best description of the experimental CO_2 responses of Fe_c_64%, Fe_c_am, Fe_c_14nm and Fe_c_19nm was achieved with model 4 (Figure 4.30). This model considers a reversible molecular adsorption of CO_2. The adsorbed CO_2 species can dissociate with participation of an additional free active site to yield adsorbed CO and O species. The dissociation is reversible, i.e., the two latter species could combine back to the molecularly adsorbed CO_2. The sensitivity analysis revealed that the association rate constant could be excluded without worthening the fit. Thus, only the rate constants of CO_2 adsorption, desorption of adsorbed CO_2 and dissociation of adsorbed CO_2 could be unambiguously obtained as the fitting parameters. As the rate constants of CO_2 adsorption or dissociation of adsorbed CO_2 correlate with the total number of active sites, the corresponding effective rate constants (a product of the rate constant and the total number of active sites, i.e. $k_{ads}^{eff}(CO_2)$ and $k_{dis}^{eff}(CO_2)$) are reported together with the rate constant of desorption of adsorbed CO_2 in Table 4.10.
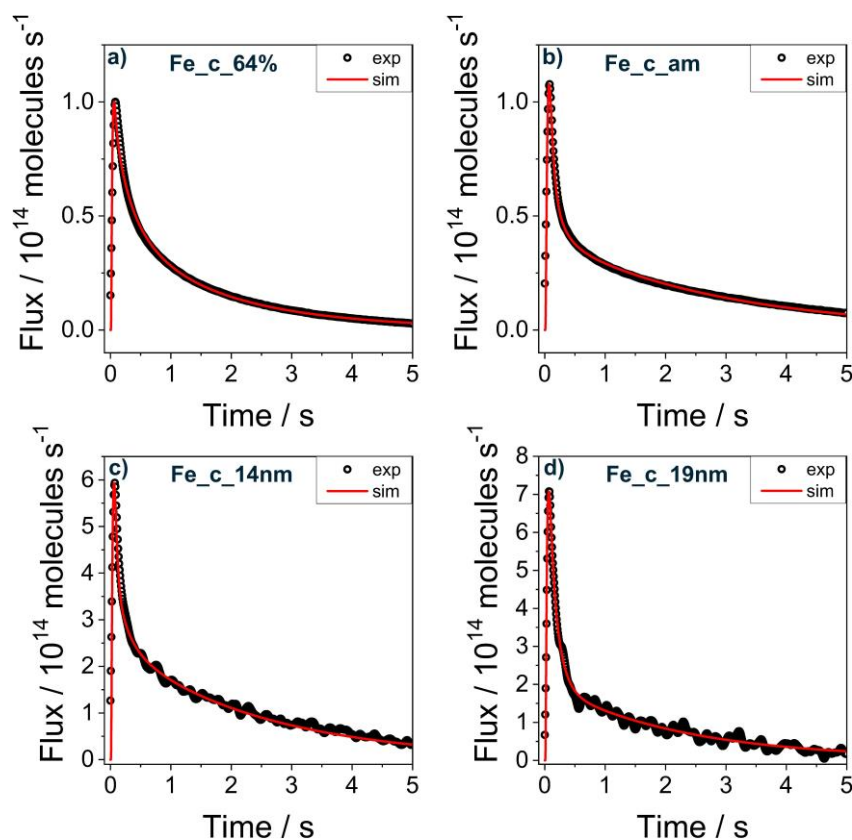

Figure 4.30. Comparison of simulated responses obtained with Model 4 in Table 4.9 with the experimental CO_2 responses over selected spent catalysts.

As could be seen in Table 4.10, the spent catalysts do not meaningfully differ in the adsorption constant ($k_{ads}^{eff}(CO_2)$) values while significant differences were determined for the desorption constants ($k_{des}(CO_2)$). Consequently, the spent materials possess different values of the equilibrium constant of CO_2 adsorption denoted as the $k_{ads}^{eff}(CO_2)/k_{des}(CO_2)$ ratio (Table 4.10). The ratio increases in the following order: Fe_c_19nm > Fe_c_am ≥ Fe_c_14nm > Fe_c_64%. Accordingly, the same activity order was established for the efficient constant of dissociation of adsorbed CO_2. The higher the dissociation constant value, the higher the surface coverage by CO and O species is.

Table 4.10. Kinetic parameters of CO_2 and CO activation and the amount of HD formed via H_2–D_2 exchange over selected spent catalysts.

Catalyst	CO_2				CO	H_2/D_2
	$k_{ads}^{eff}(CO_2)$ / s^{-1}	$k_{des}(CO_2)$ / s^{-1}	$k_{ads}^{eff}(CO_2)/k_{des}(CO_2)$ / -	$k_{dis}^{eff}(CO_2)$ / s^{-1}	$k_{ads}^{eff}(CO)$ / s^{-1}	n(HD) / -
Fe_h_23%	$-^a$	$-^a$	$-^a$	$-^a$	$2.20 \cdot 10^2$	0.0080
Fe_c_64%	$2.37 * 10^3$	$1.28 * 10^1$	$1.86 * 10^2$	$2.92 * 10^{-1}$	$5.40 \cdot 10^1$	0.0104
Fe_c_am	$4.53 * 10^3$	$5.87 * 10^{-1}$	$7.72 * 10^3$	4.89	$8.75 \cdot 10^2$	0.0122
Fe_h_82%	$-^a$	$-^a$	$-^a$	$-^a$	$6.78 \cdot 10^2$	0.0068
Fe_c_10nm	$-^a$	$-^a$	$-^a$	$-^a$	0.00^b	0.0220
Fe_c_14nm	$6.20 * 10^3$	1.26	$4.94 * 10^3$	2.80	0.00^b	0.0375
Fe_c_19nm	$4.13 * 10^3$	$3.00 * 10^{-1}$	$1.38 * 10^4$	$2.84 * 10^1$	0.00^b	0.0194
Fe_h_31nm	$-^a$	$-^a$	$-^a$	$-^a$	$1.80 \cdot 10^2$	0.0016

a. Kinetic analysis is impossible due to very strong CO_2 adsorption or/and more complicated model requirement.
b. CO response is described by diffusion.

Because of the very strong CO_2 adsorption and consequently the low signal to noise ratio, the above-described kinetic analysis failed to provide reliable data for the Fe_h_23% and Fe_h_82% materials. Nevertheless, it could be safely concluded that the $k_{ads}^{eff}(CO_2)/k_{des}(CO_2)$ ratio of these catalysts should be higher than the one of other materials based on the crossing point of the dimensionless responses of CO_2 and Ar, which is shifted to longer times for the Fe_h_23% and Fe_h_82% materials. Model 4 was also deficient to describe the experimental

CO_2 responses of the Fe_c_10nm and Fe_h_31nm materials. The description failure could be explained by the quality of the experimental signal due to a strong CO_2 adsorption. Another possible reason could be that the mechanism/elemental steps of CO_2 interaction with sample surface changes/complicates in comparison with Model 4.

To investigate the interaction of CO with spent catalysts, CO/Ar = 1:1 pulse experiments were performed and evaluated as above-described for the CO_2 pulse experiments. No noticeable difference between the dimensionless CO and Ar responses was obtained for the Fe_c_10nm, Fe_c_14nm and Fe_c_19nm materials. This means that CO interacts with the surface of these catalysts very weakly. The dimensionless CO response of other materials does not cross the dimensionless Ar response and its peak maximum is below that of Ar (Figure A.10). This is a distinguish marker of irreversible CO adsorption [115]. Nevertheless, different microkinetic models (Table 4.11) considering reversible interactions were applied to describe the experimental CO responses to double-check this theoretical statement.

Table 4.11. Micro-kinetic models applied for kinetic modeling of CO adsorption and activation.

Model	Elementary step	Rate constants
1	Diffusion	D_{eff}
2	$CO + * \rightarrow *-CO$	k_{ads}^{eff} [a]
	$*-CO \rightarrow CO + *$	k_{des}
3	$CO + 2* \rightarrow *-C + *-O$	k_{diss}^{eff} [a]
	$*-C + *-O \rightarrow CO + 2*$	k_{ass}^{eff}
4	$CO + * \rightarrow *-CO$	k_{ads}^{eff} [a]
	$*-CO \rightarrow * + CO$	k_{des}
	$*-CO + * \rightarrow *-C + *-O$	k_{diss}^{eff} [a]
	$*-C + *-O \rightarrow *-CO + *$	k_{ass}

a. Due to the correlation between total concentration of active sites and the rate constants of adsorption or dissociation, only their product could be calculated and denoted as k_{ads}^{eff} or k_{diss}^{eff}.

The best description of the experimental data with the lowest deviation between the experimental and modelled responses was obtained by using model 2 (Figure 4.31). This model considers a reversible molecular adsorption of CO on a free active site. The obtained rate constants of CO adsorption and desorption of adsorbed CO are presented in Table 4.10. The

results of sensitivity analysis revealed that the desorption rate constant could be excluded without worthening the fit, which again proves that CO adsorbs irreversibly. The values of CO effective adsorption rate constant increase in the following order: Fe_c_am > Fe_h_82% > Fe_h_23% ≈ Fe_h_31nm > Fe_c_64% >> Fe_c_10nm ≈ Fe_c_14nm ≈ Fe_c_19nm.
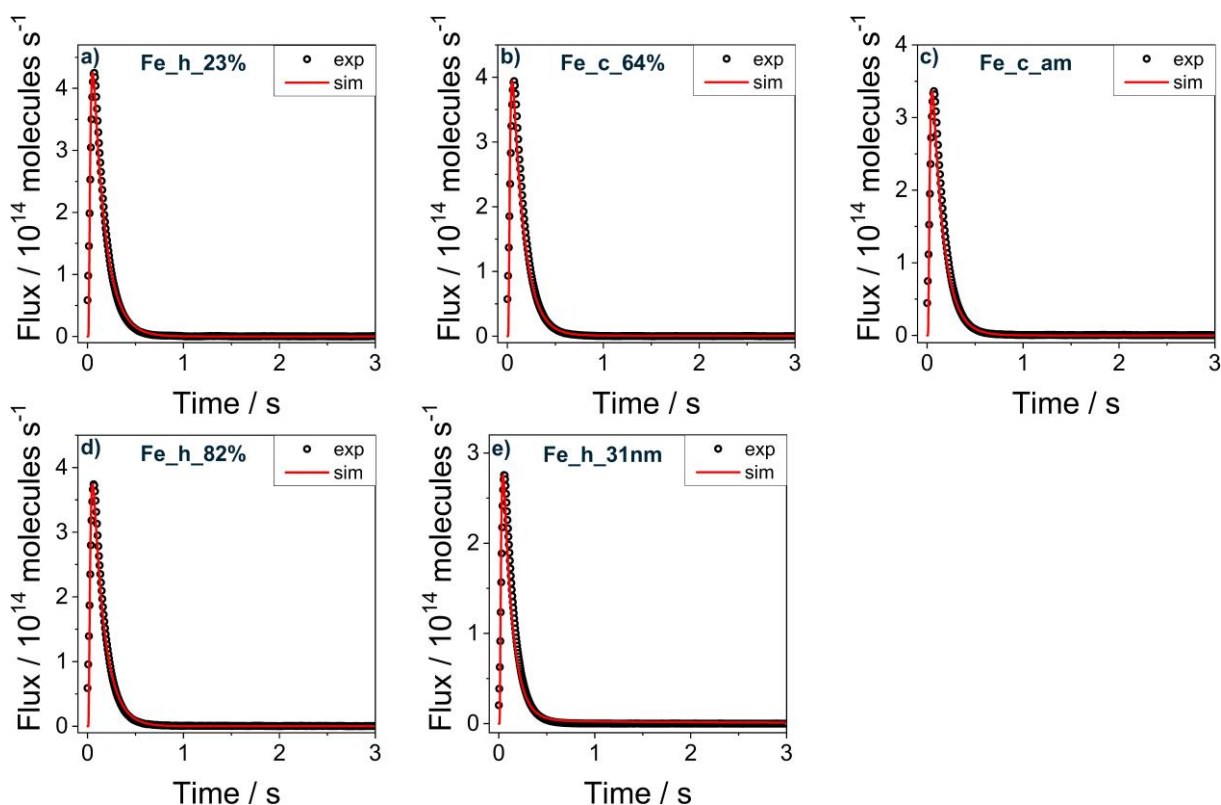

Figure 4.31. Comparison of simulated responses obtained with Model 2 in Table 4.11 with the experimental CO responses over selected spent catalysts.

Hydrogen isotopic exchange experiments were conducted to investigate the ability of spent materials to activate gas-phase hydrogen. Unfortunately, no HD was detected at the reaction temperature of the catalytic experiments, i.e., at 300 °C due to much shorter contact time in the TAP tests in comparison with the CO_2-FTS tests. Therefore, additional exchange experiments were performed at 400 °C, at which some amounts of HD were detected. The transient responses of D_2, HD and H_2 obtained at this temperature are given in Figure A.11. As the HD response is detected after those of H_2 and D_2, it could be safely concluded that H-H and D-D bonds were dissociated upon activation of these feed components on the surface of samples and a new H-D bond was formed. The amount of HD formed in these experiments is a measure of catalyst activity for dissociation and formation of these bonds. The corresponding values for all the materials are given in Table 4.10. The highest ability to activate hydrogen was determined for Fe_c_10nm, Fe_c_14nm and Fe_c_19nm catalysts. In comparison to these materials, the

amount of HD detected over Fe_h_23%, Fe_c_64%, Fe_c_am and Fe_h_82% catalysts is more than twice lower. These materials do not differ much from each other in this regard. The Fe_h_31nm catalyst possesses the weakest ability for H_2 activation. Therefore, regarding H_2 activation ability, the materials could be ordered as follows: Fe_c_14nm >> Fe_c_10nm ≈ Fe_c_19nm >> Fe_c_am ≈ Fe_c_64% > Fe_h_23% ≈ Fe_h_82% >> Fe_h_31nm.
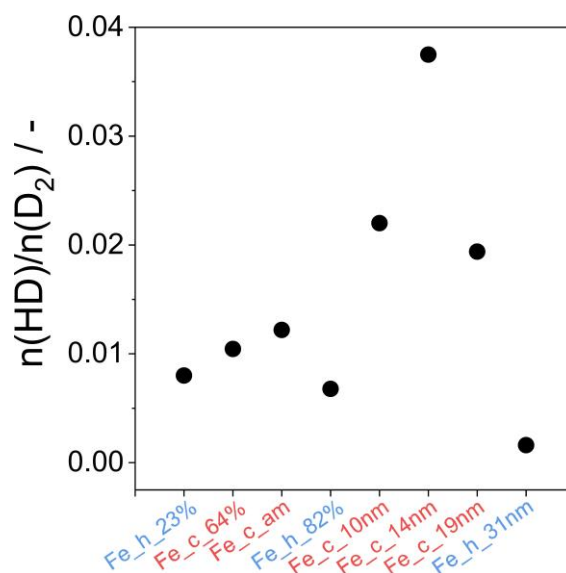

Figure 4.32. The HD amount normalized to the initial D_2 amount in H_2–D_2 exchange experiments at 400 °C over selected spent catalysts (100 mg fraction).

4.2.7 Iron carbide defect structure and its influence on adsorption ability and catalytic performance

According to the analysis of spatial distribution of steady-state catalyst composition, there is no Fe_3O_4 phase in the first up-stream located layer (up to first 1/6) of any spent catalyst. Fe_5C_2 is exclusively present in the first segment (Figure 4.29). As all reaction products CO, CH_4 and C_{2+}-hydrocarbons are produced in this segment, it could be suggested that the iron carbide is an active phase for both the RWGS reaction and CO_x hydrogenation to CH_4 as well as C-C coupling reactions yielding higher hydrocarbons. In agreement with this statement, Zhu et al. [130] recently reported that a model Fe_5C_2 catalyst was able to generate all the mentioned products without the presence of Fe_3O_4 phase. However, it cannot be completely excluded that a thin layer (low content undetectable by Mössbauer) of Fe_3O_4 could be formed on the surface of Fe_5C_2. Magnetite is generally accepted to be responsible for the conversion of CO_2 to CO. The present study additionally showed that Fe_5C_2 materials formed from differently synthesized Fe_2O_3 strongly differ in their reactivity to form C_{2+}-hydrocarbons and CH_4, which is determined from the analysis of the reaction rates in the first catalysts segment (Figure 4.29). The iron

carbide in Fe_c_* materials revealed approximately 2 times higher formation rates of CH_4 and C_{2+}-hydrocarbons than the one in Fe_h_* catalysts. The difference in iron carbides properties is also displayed in the ratio of C_{2+}-hydrocarbons/CH_4 formation rates.

Table 4.12. Experimental values of relative content of Fe state (ratio in brackets) in Fe_5C_2 and hyperfine field obtained experimentally at 298 K. Estimated values of hyperfine field at 0 K (Table A.2) as well as calculated C/Fe ratio based on the relationship between the average B_{hf} (0 K) and C/Fe ratio reported by [131]. Mössbauer data of 100 mg fraction of spent catalysts (110 h on-stream) was used for calculation.

Catalyst	Fe state	Content / %	B_{hf} (298 K)$_{exp}$ / T	B_{hf} (0 K)$_{est}$ / T	C/Fe ratio
Fe_c_10nm	I	40.1 (2.0)	21.64	26.27	0.344
	II	37.4 (1.9)	18.40	22.82	
	III	22.5 (1.1)	10.84	13.85	
Fe_h_31nm	I	38.4 (2.0)	21.57	26.19	0.353
	II	37.8 (2.0)	18.30	22.69	
	III	23.8 (1.2)	10.70	13.67	
Fe_h_23%	I	36.8 (2.0)	21.68	26.32	0.349
	II	39.8 (2.2)	18.42	22.84	
	III	23.3 (1.3)	10.84	13.85	
Fe_c_64%	I	45.3 (2.0)	21.25	25.80	0.331
	II	36.7 (1.6)	18.52	22.96	
	III	18.0 (0.8)	10.83	13.84	
Fe_c_am	I	39.2 (2.0)	21.48	26.08	0.349
	II	38.3 (2.0)	18.38	22.79	
	III	22.5 (1.1)	10.74	13.73	
Fe_h_82%	I	37.6 (2.0)	21.53	26.14	0.353
	II	39.0 (2.1)	18.32	22.72	
	III	23.4 (1.2)	10.75	13.74	

To elucidate possible fundamental reasons behind the distinctive reactivity of Fe_5C_2, iron carbide structural properties were further investigated using the obtained Mössbauer spectra of spent materials. Fe_5C_2 belongs to a monoclinic crystal system (C2/c space group) and has 28 atoms in the unit cell (Figure 4.33a). Fe atoms are located in three different positions, which could be identified by Mössbauer spectroscopy (Figure A.8). These states are related as 2:2:1 in the perfect Fe_5C_2 structure [132]. However, the distribution of these states in spent catalysts

in this study deviates from the theoretical one due to the imperfection of their crystal structures (Table 4.12).

As suggested by Liu et al. [131], the C/Fe ratio in iron carbides present in spent materials was calculated using the average hyperfine field value (average B_{hf}). This field is expressed as the sum of the hyperfine fields (B_{hf}) of different Fe states multiplied by their occupational weight. The values of individual hyperfine fields were determined from the Mössbauer spectra of the measured samples. The average hyperfine field in Fe_5C_2 as a function of C/Fe ratio is defined in equation 4.9. However, it should be noted that Mössbauer experimental data was collected at 298 K, while the above-mentioned theoretical relationship was determined for the hyperfine field values obtained at 0 K. Taking this into account, the hyperfine field values of different Fe states were calculated based on the ratio between the hyperfine field values in the perfect Fe_5C_2 structure obtained experimentally in [131] at 0 and 298 K (Table A.2).

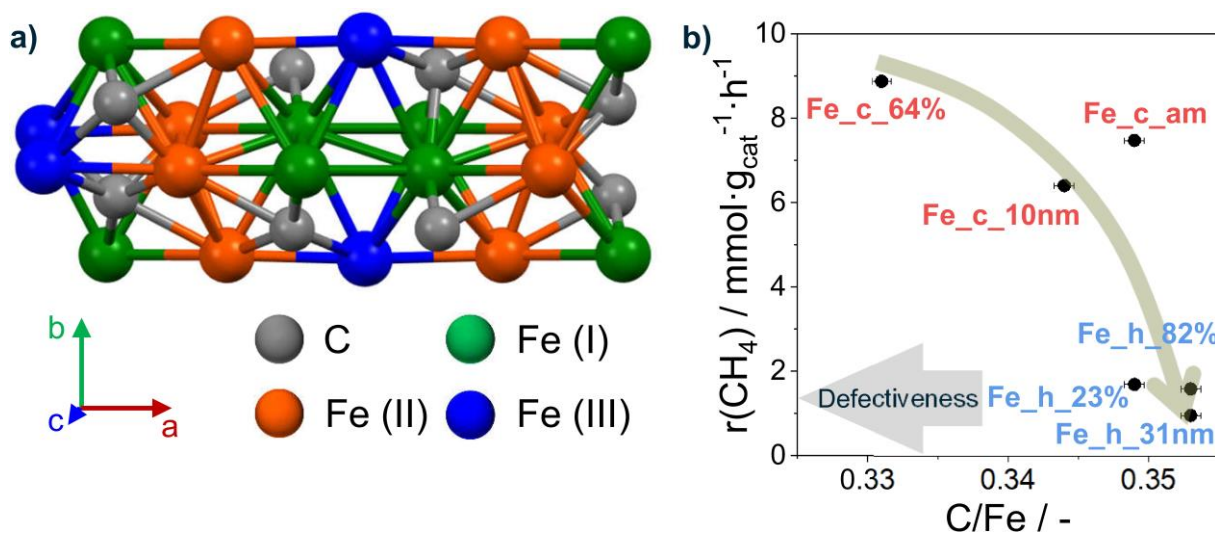$$\text{average } B_{hf} = -33.1 * (C/Fe) + 33.58 \qquad (4.9)$$

Figure 4.33. (a) The crystal structure of Fe_5C_2 (b) the relationship between the initial CH_4 formation rate and C/Fe ratio in iron carbides calculated from Mössbauer data of spent catalysts (100 mg fraction).

The calculated ratio of C/Fe for all investigated materials is lower than the theoretical one in the perfect Fe_5C_2 structure (Figure 4.33b). Therefore, iron carbides in spent catalysts deviates from the stoichiometric composition. In other words, the Fe_5C_2 structure should have carbon vacancies. However, the amount of these defects in the iron carbides in the spent Fe_h_* materials should be lower than in their Fe_c_* counterparts as deduced from the C/Fe ratio. Regardless of the defectiveness, this ratio is representative for electronic properties of Fe atoms

in the Fe_5C_2 structure. The higher the ratio, the more electronic density should be transferred from Fe to C atoms. Under this consideration, Fe atoms in the iron carbide in the Fe_h_* spent materials should be in more oxidized state in comparison with their Fe_c_* counterparts. As the only difference between the home-synthesized and commercial iron oxalate dihydrates used for the preparation of Fe_2O_3 catalysts is the size of particles and of their agglomerates, the morphology seems to be a decisive descriptor affecting the ability of Fe_2O_3 to *in situ* form iron carbides with specific defective and electronic properties.

Based on the above discussion and the results of catalytic experiments in Figure 4.29, it could be concluded that both the defectiveness and the electronic properties of iron carbides might be responsible for the difference in the reactivity of Fe_5C_2 in the Fe_c_* and Fe_h_* materials. Iron carbides with defect-lesser structure and Fe atoms being in the more oxidized state revealed lower reactivity for CO_x hydrogenation and C-C coupling reactions. These carbides possess stronger ability to adsorb CO_2 and CO and lower ability to adsorb and activate H_2 in comparison with iron carbides with defect-richer structure and Fe atoms being in the less oxidized state (Table 4.11). Therefore, the surface coverage of such carbides is richer in carbon-containing species and poorer in hydrogen-containing species. This situation is beneficial for suppressing CH_4 formation in favor of long-chained unsaturated hydrocarbons.

4.2.8 Summary

The controlled decomposition of iron (II) oxalate dihydrate in air was shown to be a suitable approach for generation of hematite-containing catalysts. Tailored catalyst preparation allowed to investigate effects of crystallite size and initial composition (α-/γ-Fe_2O_3) on catalytic performance and reaction-induced changes into Fe_5C_2 under reaction conditions. The variation of the size of α-Fe_2O_3 crystallites in single-phase catalysts and of the ratio of α-Fe_2O_3/γ-Fe_2O_3 phases in mixed-phase materials provided the possibility to vary the reducibility of iron (III) oxide catalysts.

Reaction pathways leading from CO_2 to CO, CH_4 and C_{2+}-hydrocarbons over the above-mentioned catalysts were determined and do not differ from those established for magnetite-containing catalysts with one exception. Hydrogenolysis of C_{2+}-hydrocarbons to CH_4 do not play any significant role in CO_2-FTS over hematite-containing catalysts. The reducibility of these catalysts was shown to be an important descriptor for controlling methane selectivity. The higher the reducibility, the lower the impact of direct CO_2 methanation and the higher the impact of CO hydrogenation to CH_4 into overall methane formation is. Although, the latter

effect is less pronounced than the former one, thus, leading to the lower overall CH_4 production. The morphology of iron (II) oxalate dihydrate has the largest influence on the production of methane because it affects the defective structure of Fe_5C_2, which was expressed as the ratio of C/Fe. All iron carbides are generated directly in the up-stream part of the catalyst bed and their content decreases in the down-stream layers upon progressing CO_2 conversion. The spatial distribution is dependent on partial pressures of CO and H_2O participating in Fe carburization to Fe_5C_2 and oxidation of Fe/Fe_5C_2, respectively. The reactivity of Fe_5C_2 to consume CO determines the strength of the increase in the ratio of H_2O/CO along the catalysts bed and the spatial distribution of Fe_5C_2 and Fe_3O_4. Defective-lesser carbides possess lower reactivity towards CO_x hydrogenation and, therefore, are present in higher amount in downstream-located catalyst layers in comparison with defective-richer iron carbides. Different reactivity of iron carbides is the consequence of their different adsorption properties. The lower the deviation of Fe_5C_2 from the stochiometric composition, the higher the ability of the iron carbide to adsorb CO and CO_2 and the lower the ability to activate H_2 is. Stronger CO_x and weaker H_2 adsorption led to a lower overall CO_2 consumption reaction rate but suppressed formation of CH_4. Defective-lesser iron carbides show higher olefin/paraffin (among C_2-C_4 hydrocarbons) and C_{2+}/CH_4 formation rate ratios.

4.3 Magnetite-containing catalysts promoted with alkali metals

Magnetite-containing catalysts with the variation of the kind of alkali metal promoter (Li, Na, K, Rb or Cs) with a fixed M/Fe atomic ratio (0.005) or with different Rb/Fe atomic ratios (0.001, 0,005, 0.01 or 0.05) were prepared through the decomposition of iron (II) oxalate dihydrate doped with the corresponding alkali metal carbonate. The idea behind was to understand the effects of the amount and the nature of alkali metal promoter on CO_2 conversion and product selectivity as well as the pathways of product formation in the course of CO_2 hydrogenation to higher hydrocarbons.

4.3.1 General characterization of fresh catalysts

The content of alkali metal dopant in the prepared materials was controlled by means of ICP or AAS analysis. The determined amount is in accordance with the desired M/Fe ratio (Table 4.13). Slightly lower content of Cs could be explained by lower accuracy of AAS method in comparison with ICP analysis.

Table 4.13. The content of alkali metals determined by ICP or AAS (for Cs) analysis.

	w(Fe) / %	w(M) / %	$v(Fe)^a$ / mol	$v(M)^a$ / mol	v(M)/v(Fe) / -
0.005Li/Fe	78.85	0.05	1.4118	0.0065	0.0046
0.005Na/Fe	79.35	0.19	1.4208	0.0080	0.0057
0.005K/Fe	78.67	0.27	1.4086	0.0070	0.0050
0.005Rb/Fe	79.86	0.54	1.4299	0.0063	0.0044
0.005Cs/Fe	78.19	0.68	1.4000	0.0051	0.0037
0.001Rb/Fe	71.01	0.11	1.3252	0.0013	0.0010
0.01Rb/Fe	72.83	1.21	1.3040	0.0142	0.0109
0.05Rb/Fe	66.05	5.00	1.1826	0.0585	0.0495

a. Calculated based on 100 g of the substance.

The phase composition of all fresh promoted and unpromoted magnetite-containing catalysts was determined by means of XRD analysis The corresponding XRD patterns are shown in Figure 4.34. Fe_3O_4, Fe, Fe_3C and Fe_5C_2 phases were identified in all catalysts. Their content according to the Rietveld analysis does not depend on the kind or the amount of alkali metal promoter. Some minor deviations could be explained by the measurement error. The crystallite size of the dominant (80.7%) Fe_3O_4 phase is 20 nm, while the crystallite size of the metallic Fe

present with the fraction of 1.5% is a little bit larger - 26 nm. Iron carbides Fe_3C and Fe_5C_2 with the corresponding crystallite sizes are 20 and 18 nm are present with the weight amounts of 9.4 and 8.3%, respectively.
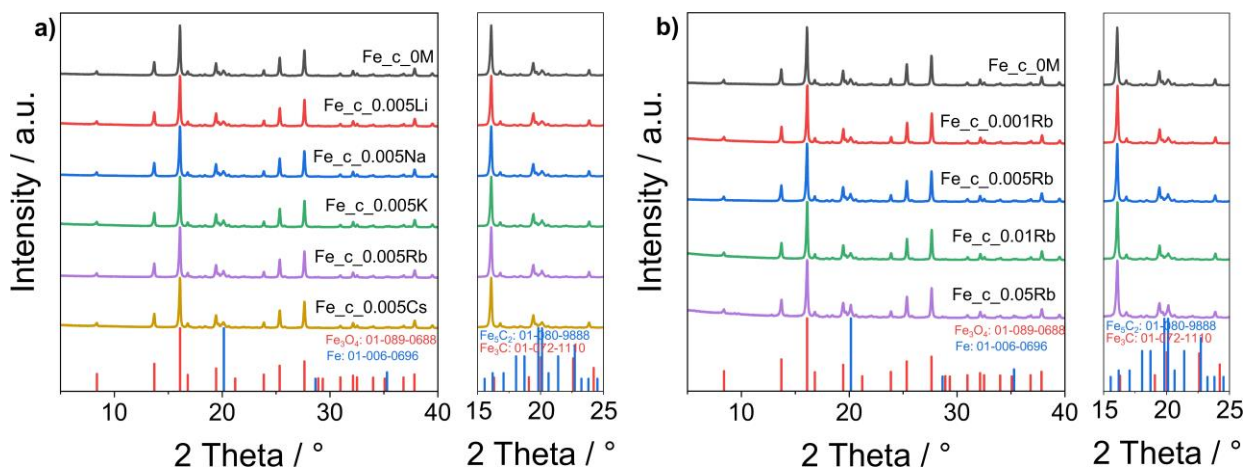

Figure 4.34. XRD patterns of fresh magnetite-containing promoted with an alkali metal catalysts.

The presence of iron carbides in the catalysts derived through decomposition of iron oxalate dihydrate precursor under O_2-free conditions was thoroughly discussed in section 4.1.1. Briefly, iron oxalate decomposes to solid-phase FeO and gas-phase CO and CO_2. Wüstite phase is unstable below 570 °C and disproportionates to metallic Fe and Fe_3O_4. Iron carbides are formed through a reaction of metallic Fe with CO [114]. Although, the promoted catalysts were prepared under the same conditions as in the synthesis of Fe_h_330, a deviation in the fraction of iron carbide phases between these two groups of catalysts was established. The reason can be the usage of commercial iron oxalate dihydrate instead of the in-house synthesized one used to prepare Fe_h_330. Thus, differently prepared iron oxalates have different reactivity in the decomposition reaction.

The BET specific surface area (S_{BET}) of about 23 m^2/g was determined for all fresh catalysts. This result together with the above-discussed XRD results suggests that the addition of alkali metal dopant does not influence the decomposition of iron oxalate dihydrate.

The effect of the dopant on the reducibility of fresh catalysts was investigated by conducting H_2-TPR measurements. The obtained H_2-TPR profiles are presented in Figure 4.35. All the catalysts consume hydrogen continuously above 420 °C without any pronounced maximum, which is in accordance with previously described reduction of magnetite-containing catalysts and supported by a previous study dealing with Fe_3O_4-nanocatalysts [76]. The reduction

proceeds through a two-step mechanism $Fe_3O_4 \rightarrow FeO \rightarrow Fe$, with the first step occurring at lower temperatures [123]. However, these individual steps are not well distinguished in the present H_2-TPR profiles, which could be affected by the concentration of feed H_2 or/and heating rate.
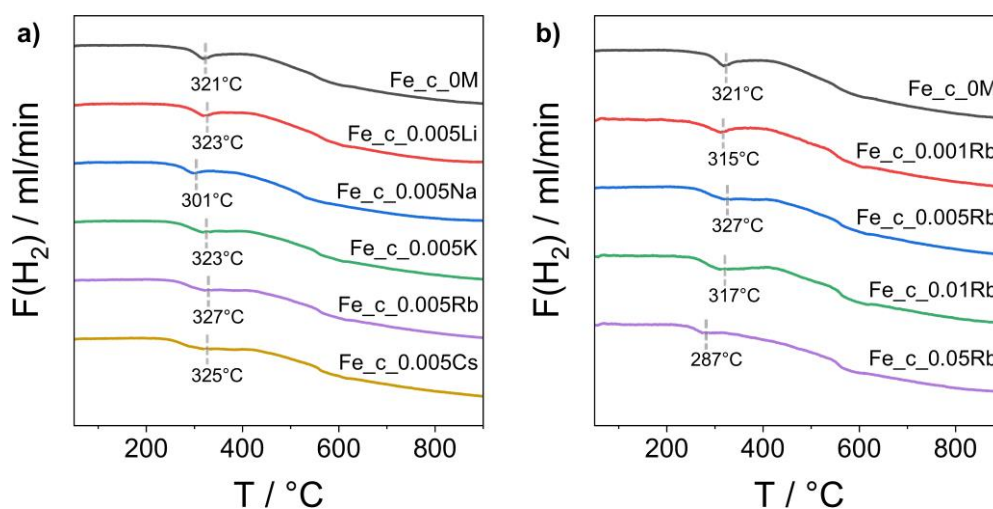

Figure 4.35. Profiles of H_2 flow upon H_2-TPR (5 vol% H_2 in Ar) of fresh catalysts.

In addition to the main reduction processes occurring above 420 °C, another well-resolved H_2 consumption peak characterized by the temperature of maximal reaction rate in the range of 280-330 °C could be observed. It could be related to the complete hydrogenation of iron carbides resulting in metallic Fe and gas-phase CH_4 [124]. The formation of methane was experimentally detected as a signal at AMU of 16 also reaching maximum at the same temperature, where H_2 is consumed without water formation (Figure A.12). The absence of water is proved by the fact that signal at AMU of 18 related to water was not observed at the respective temperature. The temperature of the maximal rate of H_2 consumption due to iron carbides reduction is not influenced by any kind of alkali metal promoter, except for Na. Generally, this temperature is located between 315 and 327 °C, but for sodium-promoted material it lays at 301 °C. No effect of promoter on the reducibility of fresh catalysts could be the consequence of its relatively low concentration. When the concentration increases, the reduction of iron carbides proceeds at lower temperature as established for the Rb-containing materials (Figure 4.35b), for which Rb loading was varied.

4.3.2 *The effect of the kind of the promoter on the catalytic performance*

A long-term stability CO_2-FTS experiment (about 65 h on stream) with the alkali-metal-promoted materials was carried out at 300 °C and 15 bar without any preceding reductive catalyst treatment. All catalysts performed stable after reaching a steady-state operation after

the first 30 h on stream (Figure 4.36). With exception for 0.005Li/Fe, an increase in the olefin/paraffin ratio within C_2-C_4 hydrocarbons with time-on-stream could be observed for other catalysts.
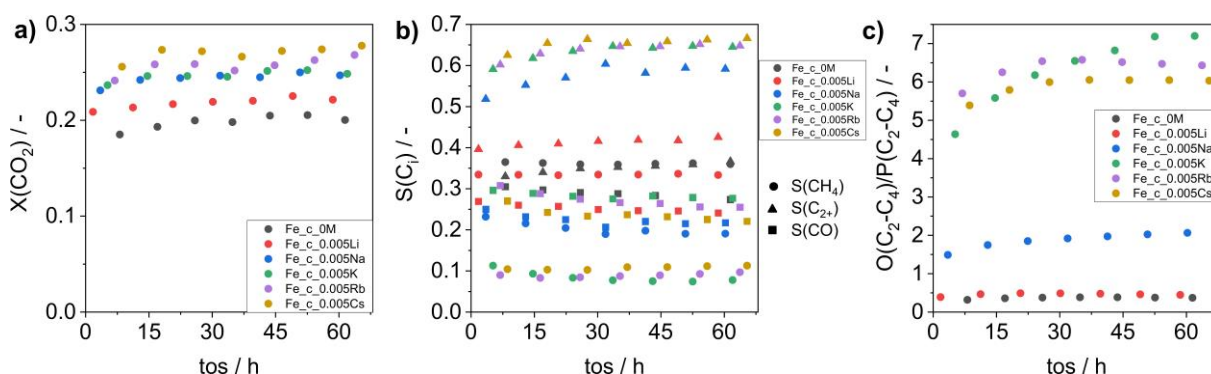

Figure 4.36. On-stream profiles of (a) CO_2 conversion, (b) product selectivity and (c) olefin/paraffin ratio within C_2-C_4 hydrocarbons in CO_2-FTS over magnetite-containing catalysts promoted with different kind of alkali promoter. Reaction conditions: total pressure: 15 bar, reaction feed: CO_2:H_2:N_2 = 1:3:0.3, GHSV: 7020 mL/g_{cat}/h, temperature: 300 °C, catalyst amount: 50 mg.

Catalytic performance strongly depends on the kind of the alkali metal promoter. It is best illustrated by the selectivity-conversion plots for CO, CH_4 and C_{2+}-hydrocarbons as well as by the O(C_2-C_4)/P(C_2-C_4)-conversion plot (Figure 4.37). Different degrees of CO_2 conversion were achieved by changing the contact time through varying the catalyst amount (600, 300, 100, 50, 20, 10, 5 mg) while using a constant feed flow. The selectivity to CO decreases with an increase in CO_2 conversion, although there is a slight increase for some catalysts when the conversion exceeds 0.3 (Figure 4.37a). Such increase was previously observed in CO_2-FTS over hematite-containing catalysts (section 4.2.3) and is explained by a ununiform spatial distribution of catalytically active phases. A linear extrapolation of the CO selectivity to zero CO_2 conversion would lead to a non-zero high (above 0.8) value. This is a fingerprint for the direct conversion of CO_2 to CO. The decrease in the selectivity to CO with rising CO_2 conversion is due to further consumption of CO to hydrocarbons. The selectivity to higher hydrocarbons increases with an increase in the conversion. Its linear extrapolation to zero CO_2 conversion would give a zero value, that implies that C_{2+}-hydrocarbons are not formed directly from CO_2 (Figure 4.37b). CO is also hydrogenated to methane as could be concluded from rising CH_4 selectivity with rising CO_2 conversion. However, a non-zero CH_4 selectivity at zero degree of CO_2 conversion obtained by a linear extrapolation of the corresponding selectivity-conversion relationship suggests that CH_4 is also formed directly from CO_2 (Figure 4.37c). Therefore, two pathways of CH_4 formation could be postulated. The above results prove again

that overall pathways of CO_2 hydrogenation to CO, CH_4 and C_{2+}-hydrocarbons do not depend on the kind of catalysts applied and is uniform for all materials investigated in this study (Figure 4.11).
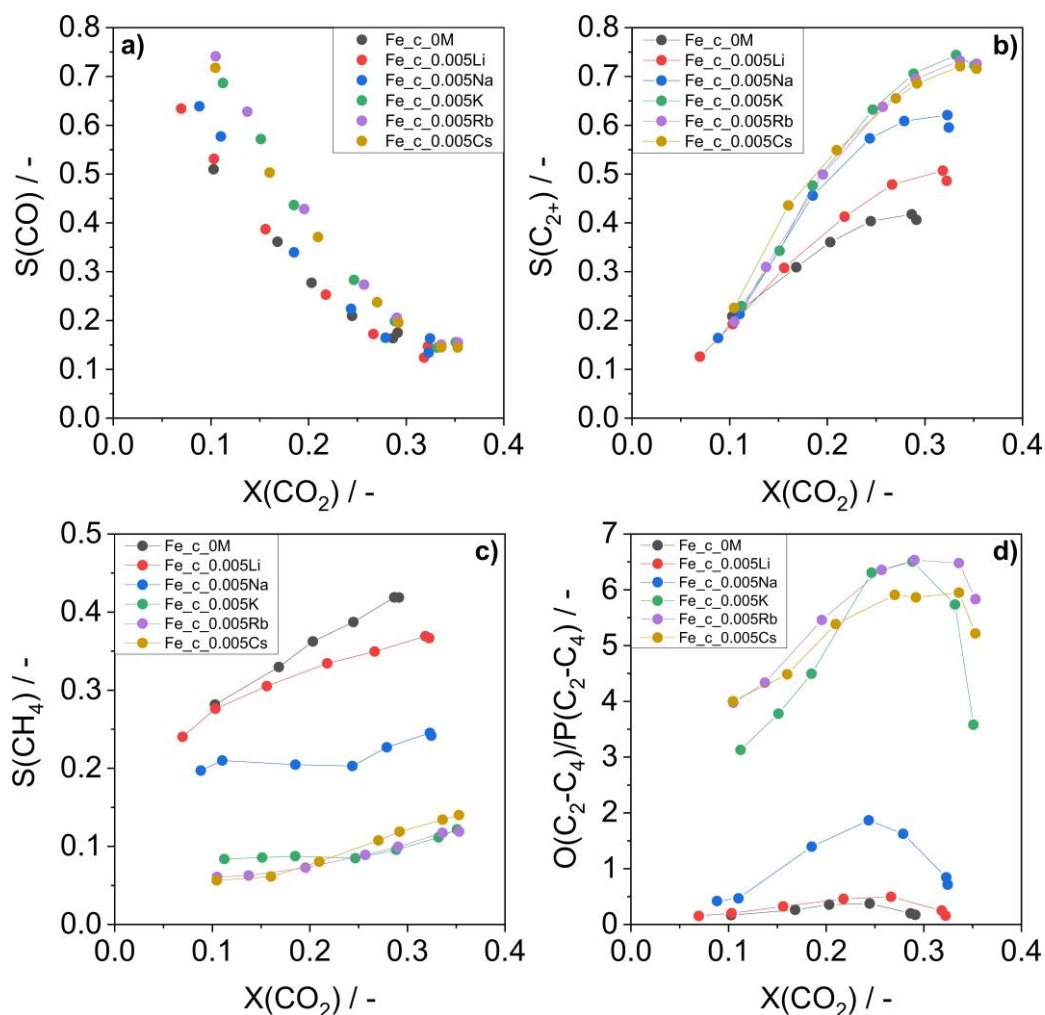

Figure 4.37. (a)-(c) Selectivity-conversion relationships (d) olefin/paraffin ratio within C_2-C_4 hydrocarbons dependence from conversion obtained over magnetite containing catalysts promoted with different kind of alkali promoter. Reaction conditions: total pressure: 15 bar, reaction feed: CO_2:H_2:N_2 = 1:3:0.3, GHSV: 585-70200 mL/g_{cat}/h, temperature: 300 °C.

The effect of the kind of alkali metal promoter on product distribution in CO_2-FTS is clearly seen from the selectivity-conversion plots for CO, CH_4 and C_{2+}-hydrocarbons. Any promoter positively influences the selectivity to C_{2+}-hydrocarbons and hinders the selectivity to CH_4 but to a different extent. Li causes the weakest promotion effect followed by Na. The best results in terms of the highest selectivity to C_{2+}-hydrocarbons and $O(C_2$-$C_4)$/$P(C_2$-$C_4)$ ratio as well as the lowest selectivity to CH_4 were obtained over K-, Rb- or Cs-promoted materials. No significant difference between these promoters could be established.

Interestingly, the $O(C_2-C_4)/P(C_2-C_4)$ ratio goes through a maximum with rising CO_2 conversion and the position of the maximum depends on the kind of the promoter. The lower the electronegativity (Pauling scale) of the promoter, the higher conversion level is required to achieve the maximum (Figure 4.37d). The same statement could also be made for the selectivity to C_{2+}-hydrocarbons. There is a decrease in this selectivity after reaching about 0.3 degree of CO_2 conversion. The lower the electronegativity of the promoter, the stronger the shift of the selectivity maximum to higher conversion values is (Figure 4.37b). Moreover, the electronegativity of the alkali metal dopant according to the Pauling scale was successfully correlated with the overall CO_2 consumption rate obtained in differential part of the reactor, i.e. at CO_2 conversion degree below 0.11 (Figure 4.38). The higher the difference between the electronegativity values of Fe and alkali metal, i.e., the lower the electronegativity of the alkali metal, the higher the consumption rate is. It was also determined that the rate C_{2+}-hydrocarbons formation increases but the rate of CH_4 formation decreases, when the alkali metal electronegativity decreases. Such correlations allow to assume that an alkali metal donates some electron density to a catalyst, thus, increasing its basicity. As CO_2 is an acidic molecule, this leads to its stronger adsorption on a surface and, consequently, to a higher C/H ratio.
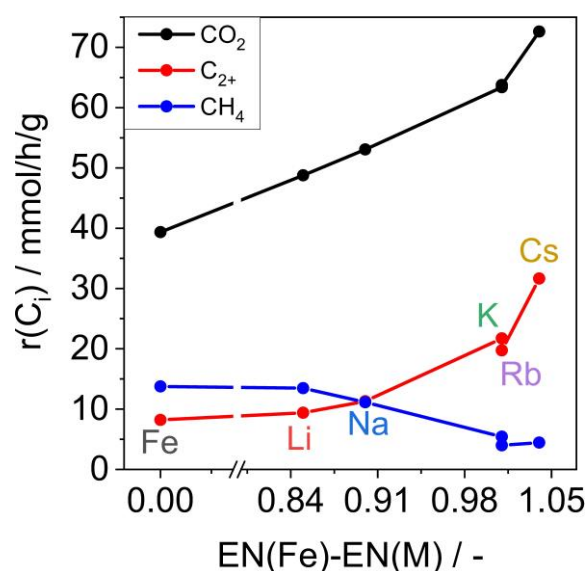

Figure 4.38. The dependence of CO_2 consumption rate ($r(CO_2)$); C_{2+}-hydrocarbons ($r_f(C_{2+})$) and CH_4 formation rates ($r_f(CH_4)$) from the electronegativity difference (Pauling scale) between Fe and alkali metal promoter (EN). Reaction conditions: total pressure: 15 bar, reaction feed: CO_2:H_2:N_2 = 1:3:0.3, GHSV: 35100 mL/g_{cat}/h, temperature: 300 °C.

To derive additional insights into the effect of the kind of alkali metal promoter on catalyst activity, segmental rates of CO_2 consumption, C_{2+}-hydrocarbons and CH_4 formation as well as

the ratio of the latter two were calculated according to equation 4.8 also used for analyzing CO_2-FTS over hematite-containing catalysts in section 4.2.5. For all materials, there is a decrease in the consumption rate of CO_2 along the catalyst bed due to a decrease in the partial pressure of CO_2 (Figure 4.39a).
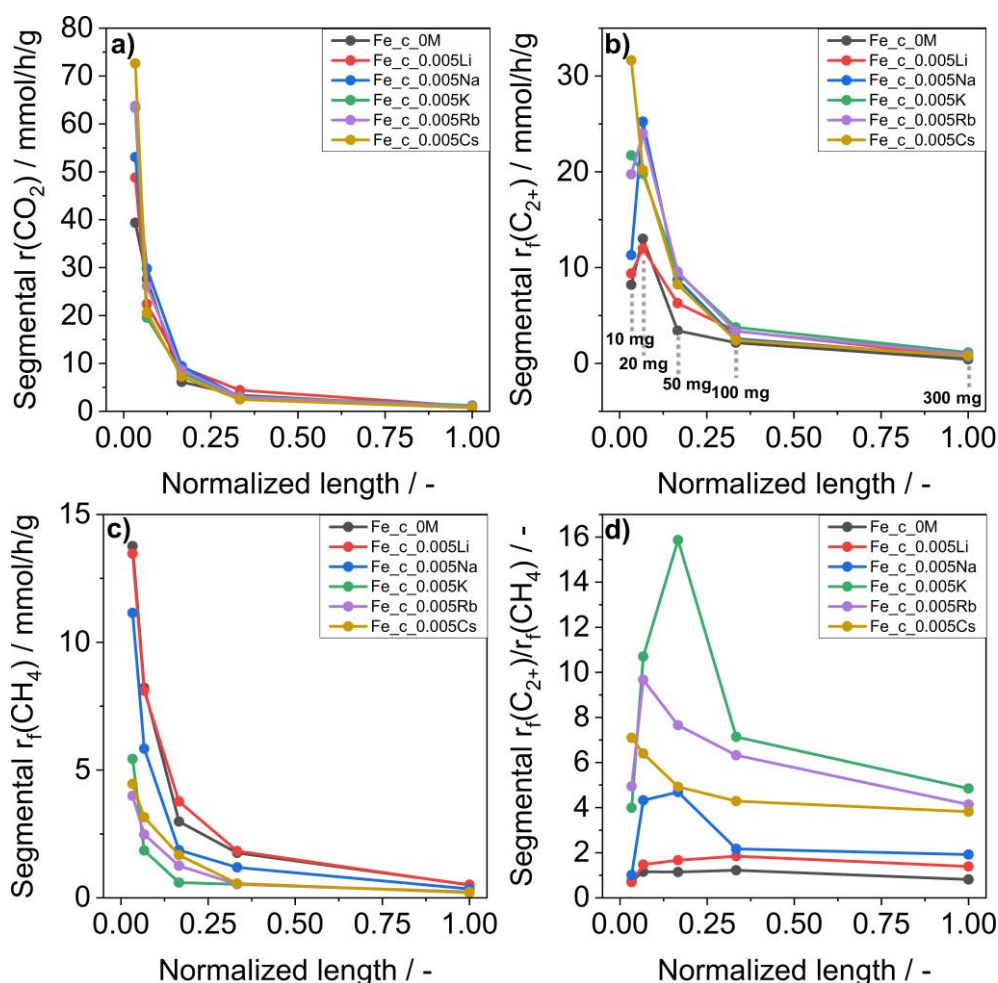

Figure 4.39. Spatial profiles of (a) segmental CO_2 consumption rate, (b) segmental formation rates of C_{2+}-hydrocarbons, (c) segmental formation rates of CH_4 and (d) C_{2+}-hydrocarbons/CH_4 formation rates ratio. Presented values are obtained over 10, 20, 50, 100, 300 mg catalyst mass loads by substitution previous mass load values from the current. Therefore, shown data represents formation rates of the specific reaction products on the catalyst bed intervals normalized to 300 mg mass load.

The rate of CH_4 formation also decreases from upstream to downstream segment (Figure 4.39c). Remarkably, Fe_c_0.005K produces almost no CH_4 after the first 1/6 layer of 300 mg catalyst bed, while this activity level over Fe_c_0.005Rb and Fe_c_0.005Cs is achieved after the first 1/3 layer. Non-doped, Li- or Na-promoted catalysts produce CH_4 along the whole catalyst bed. Interestingly, the K, Rb and Cs promoters decrease the CH_4 formation rate in the first segment (differential reactor operation), while Li and Na have almost no effect. The formation rate of

C_{2+}-hydrocarbons has a maximum along the catalyst bed for all the catalysts except for the K- and Cs-promoted materials (Figure 4.39b). The maximum is present due to the fact C_{2+}-hydrocarbons are secondary products. CO is produced in a first part of the catalyst bed and then hydrogenated to hydrocarbons. The highest ratio of C_{2+}/CH_4 formation rates also passes a maximum in downstream-located catalyst layers. The highest peak value has K-promoted catalyst, followed by Rb- and Cs-doped materials. The maximum is achieved between the 1/6 and 1/3 segments of the catalyst bed for unpromoted and Li-promoted materials, while for the Na- or K-containing catalysts, the peak position is between the first 1/15 and 1/6 part of the bed. For the Rb-promoted catalyst it shifts even more to the inlet, the maximum is achieved in the 1/30-1/15 located segment. No maximum was detected for the Cs-doped sample.

4.3.3 The effect of the amount of Rb promoter on catalytic performance

CO_2-FTS experiments over magnetite-containing catalyst promoted with different amounts of Rb were conducted over about 65 h on-stream at 300 °C, 15 bar and different contact times without any preceding catalyst reduction. The catalysts reached their steady-state operation after 30 h and remained stable for the remaining time (Figure 4.40). To illustrate the effect of Rb loading on product selectivity, selectivity-conversion plots for CO, CH_4 and C_{2+}-hydrocarbons as well as an $O(C_2-C_4)/P(C_2-C_4)$-conversion plot were prepared and are shown in Figure 4.41. Different degrees of CO_2 conversion were achieved by changing the contact time through varying the catalyst amount (600, 300, 100, 50, 20, 10, 5 mg) while using a constant feed flow.
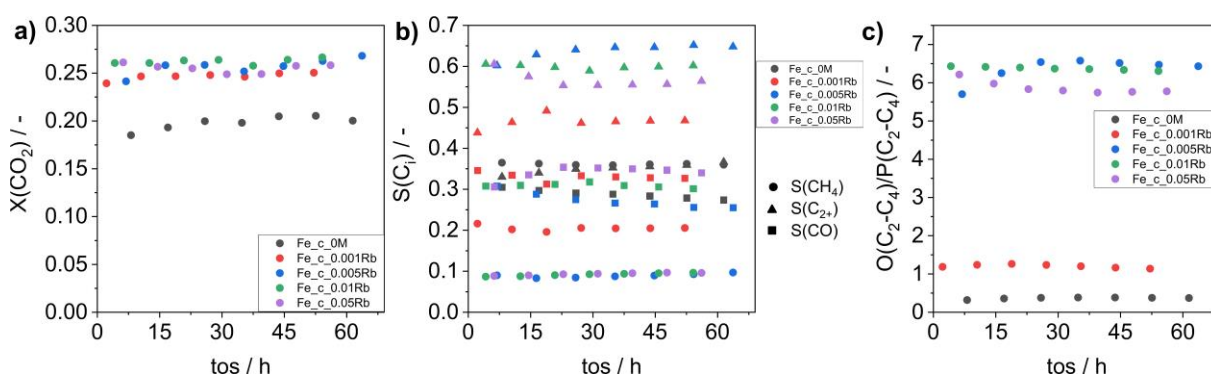

Figure 4.40. On-stream profiles of (a) CO_2 conversion and (b) product selectivity (c) olefin/paraffin ratio within C_2-C_4 hydrocarbons in CO_2 hydrogenation over magnetite containing catalysts promoted with different amount of Rb. Reaction conditions: total pressure: 15 bar, reaction feed: CO_2:H_2:N_2 = 1:3:0.3, GHSV: 7020 mL/g_{cat}/h, temperature: 300 °C, catalyst amount: 50 mg.

Any amount of Rb promoter positively influences the selectivity to C_{2+}-hydrocarbons and hinders the selectivity to CH_4 as well as enhances the $O(C_2\text{-}C_4)/P(C_2\text{-}C_4)$ ratio. While Fe_c_0.001Rb has a moderate effect on the selectivity to C_{2+}-hydrocarbons, the highest values were obtained over Fe_c_0.005Rb. The selectivity slightly decreases with a further increase in Rb loading. The decrease is due to higher CO selectivity, because the selectivity to CH_4 over the catalyst with the Rb/Fe atomic ratio of 0.005 does not meaningfully differ from that over Fe_c_0.01Rb and Fe_c_0.05Rb (Figure 4.41b,c). This result suggests that an optimal Rb content is required for efficient CO hydrogenation to higher hydrocarbons. An analogous conclusion could be made about the effect of promoter concentration on the $O(C_2\text{-}C_4)/P(C_2\text{-}C_4)$ ratio. The highest value was obtained over Fe_c_0.01Rb at the degree of CO_2 conversion of 0.3. Fe_c_0.05Rb catalyst containing the highest amount of the promoter revealed noticeably lower $O(C_2\text{-}C_4)/P(C_2\text{-}C_4)$ ratio even in comparison with Fe_c_0.005Rb material at level of CO_2 conversion higher than 0.2.
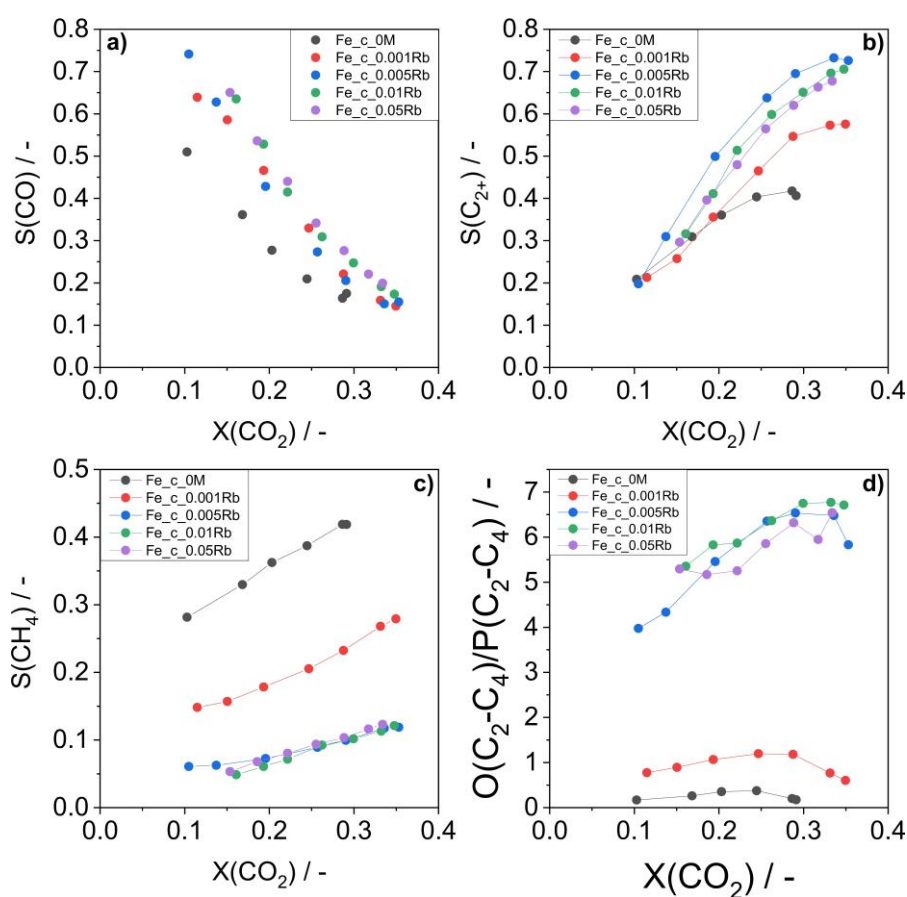

Figure 4.41. (a)-(c) Selectivity-conversion relationships (d) olefin/paraffin ratio within C_2-C_4 hydrocarbons dependence from conversion obtained over magnetite containing catalysts promoted with different amounts of Rb. Reaction conditions: total pressure: 15 bar, reaction feed: CO_2:H_2:N_2 = 1:3:0.3, GHSV: 585-70200 mL/g_{cat}/h, temperature: 300 °C.

Further insights into the effect of Rb content on CO_2-FTS were derived through analyzing segmental rates of overall CO_2 consumption, C_{2+}-hydrocarbons and CH_4 formation as well as C_{2+}/CH_4 formation rate ratio (Figure 4.42). For all catalysts, there is a decrease in the consumption rate of CO_2 along the catalyst bed due to transition from differential to integral reactor operation mode (Figure 4.42a). The Fe_c_0.01Rb material showed higher value of the reaction rate than Fe_c_0.05Rb catalyst in the first segment, where differential operation conditions are achieved. Lower values were determined for Fe_c_0.001Rb and Fe_c_0.005Rb catalysts, which do not differ much in this regard. But they are more than one and a half times greater than the one determined for the unpromoted material in the first 1/30 segment.
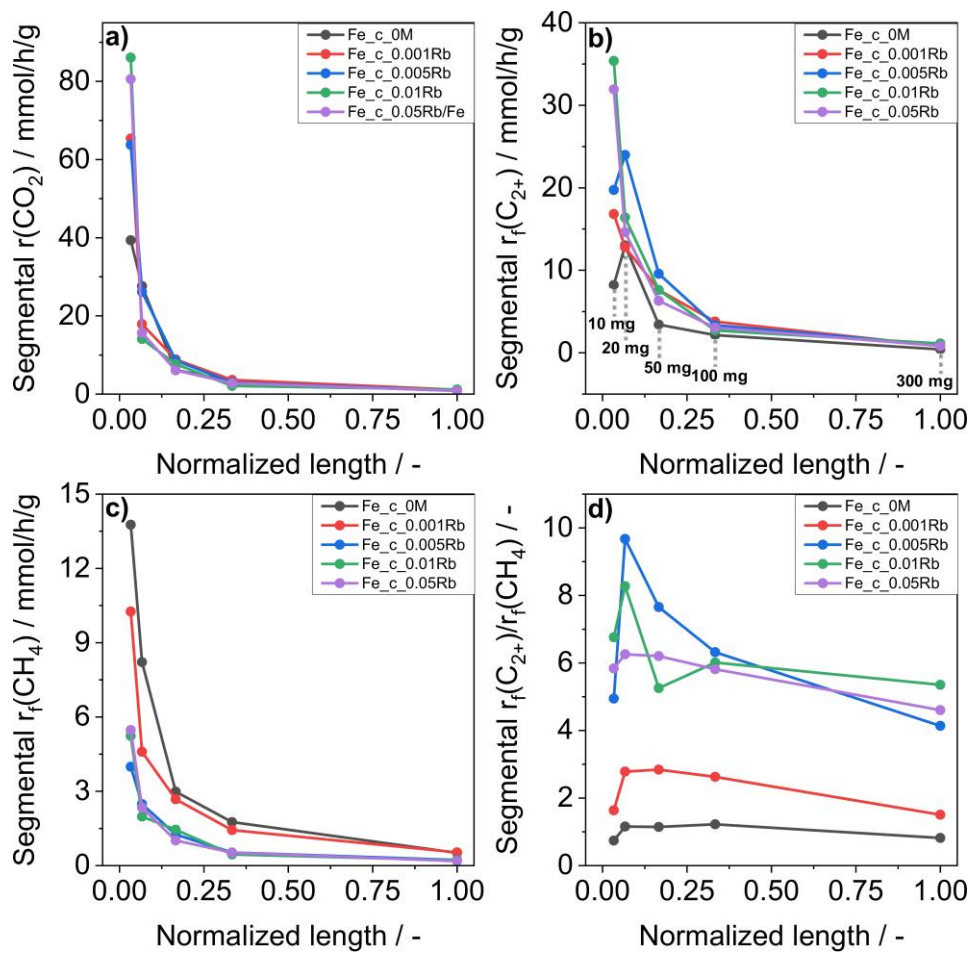

Figure 4.42. Spatial profiles of (a) segmental CO_2 consumption rate, (b) segmental formation rates of C_{2+}-hydrocarbons, (c) segmental formation rates of CH_4 and (d) C_{2+}-hydrocarbons/CH_4 formation rates ratio. Presented values are obtained over 10, 20, 50, 100, 300 mg catalyst mass loads by substitution previous mass load values from the current. Therefore, shown data represents formation rates of the specific reaction products on the catalyst bed intervals normalized to 300 mg mass load.

Spatial distribution of the CH_4 formation rate also shows a decreasing tendency along the catalyst bed (Figure 4.42c). The catalyst with the Rb/Fe atomic ratio of 0.001 has the weakest

effect on methane formation rate in comparison with the unpromoted catalyst. The lowest value of CH_4 formation rate (the strongest effect) in the initial part of the catalyst bed has Fe_c_0.005Rb. Nevertheless, the rate over this catalyst decreases along the catalyst bed and becomes almost the same as the methane formation rate values determined for Fe_c_0.01Rb and Fe_c_0.05Rb catalysts. The formation rate of C_{2+}-hydrocarbons over Fe_c_0M and Fe_c_0.005Rb passes a maximum along the catalyst bed (Figure 4.42b). Fe_c_0.01Rb has the highest C_{2+}/CH_4 formation rate ratio in the first bed segment but Fe_c_0.005Rb material shows the highest maximum value (Figure 4.42d). The peak maximum of C_{2+}/CH_4 formation rate ratio is achieved between the first 1/30 and 1/15 located segment for all Rb-promoted materials.

4.3.4 The contribution of methane formation routes into the overall methane production over alkali metal promoted magnetite containing catalysts

As concluded from the selectivity-conversion relationships in Figure 4.41, there are two primary reactions in the course of CO_2-FTS: CO_2 conversion to CO and CH_4 (Figure 4.43). To understand the influence of the kind of alkali metal promoter and the amount of Rb on the individual routes of methane formation, the rates of methane formation were analyzed as a function of CO_2 conversion degree. $r^0(CH_4)$ reflects the rate of CO_2 hydrogenation to CH_4 and $r^0(CO)$ stands for the rate of CO_2 conversion into CO. CO can be further hydrogenated to CH_4 and C_{2+}-hydrocarbons. Hereafter, $r^{CO}(CH_4)$ stands for the rate of CO conversion into CH_4 and $r^{CO}(C_{2+})$ is the rate of CO conversion into C_{2+}-hydrocarbons.
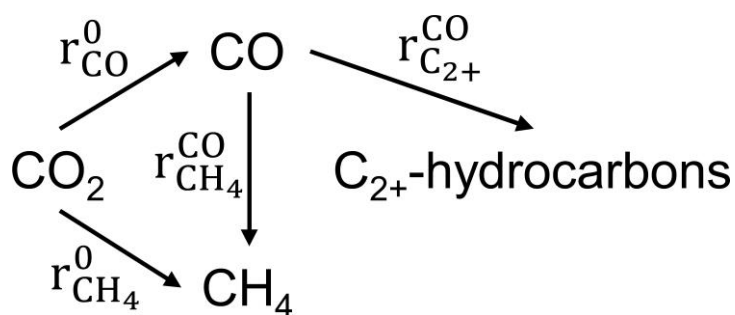

Figure 4.43. The scheme of CO_2 conversion into various reaction products with the abbreviations used for the specific reaction rates.

On this basis, the primary (at zero degree of CO_2 conversion) selectivity to methane ($S^0(CH_4)$) can be expressed through $r^0(CH_4)$ and $r^0(CO)$ according to equation 4.10. Using this equation, it is possible to calculate the ratio of $r^0(CO)$ to $r^0(CH_4)$ from $S^0(CH_4)$ (equation 4.11) and to get a relationship between primary $r^0(CO)$ and $r^0(CH_4)$ reaction rates (equation 4.12).

$$S^0(CH_4) = \frac{r^0(CH_4)}{r^0(CH_4)+r^0(CO)} = \frac{1}{1+\frac{r^0(CO)}{r^0(CH_4)}} \tag{4.10}$$

$$\frac{r^0(CO)}{r^0(CH_4)} = \frac{1-S^0(CH_4)}{S^0(CH_4)} \tag{4.11}$$

$$r^0(CO) = \frac{1-S^0(CH_4)}{S^0(CH_4)}r^0(CH_4) \tag{4.12}$$

Under consideration of CO hydrogenation to methane, the selectivity to the latter product at a non-zero degree of CO_2 conversion ($S^i(CH_4)$) can be expressed by equation 4.13.

$$S^i(CH_4) = \frac{r^0(CH_4)+r^{CO}(CH_4)}{r^0(CO)-r^{CO}(C_{2+})-r^{CO}(CH_4)+r^{CO}(CH_4)+r^0(CH_4)+r^{CO}(C_{2+})} = \frac{r^0(CH_4)+r^{CO}(CH_4)}{r^0(CH_4)+r^0(CO)} \tag{4.13}$$

Substituting the expression for $r^0(CO)$ from equations 4.12 into equation 4.13 would lead to equation 4.14. The ratio of $r^{CO}(CH_4)$ to $r^0(CH_4)$ could be obtained from the latter expression and is given in equation 4.15.

$$S^i(CH_4) = \frac{r^0(CH_4)+r^{CO}(CH_4)}{r^0(CH_4)+\frac{1-S^0(CH_4)}{S^0(CH_4)}r^0(CH_4)} = \frac{1+\frac{r^{CO}(CH_4)}{r^0(CH_4)}}{1+\frac{1-S^0(CH_4)}{S^0(CH_4)}} = \left(1+\frac{r^{CO}(CH_4)}{r^0(CH_4)}\right)S^0(CH_4) \tag{4.14}$$

$$\frac{r^{CO}(CH_4)}{r^0(CH_4)} = \frac{S^i(CH_4)-S^0(CH_4)}{S^0(CH_4)} \tag{4.15}$$

As the total rate of CH_4 formation is defined as the sum of the reaction rates of primary and secondary pathways (equation 4.16), $r^0(CH_4)$ and $r^{CO}(CH_4)$ can be expressed by equations 4.17 and 4.18, respectively.

$$r^{total}(CH_4) = r^0(CH_4) + r^{CO}(CH_4) \tag{4.16}$$

$$r^0(CH_4) = r^{total}(CH_4)\frac{S^0(CH_4)}{S^i(CH_4)} \tag{4.17}$$

$$r^{CO}(CH_4) = r^{total}(CH_4)\frac{S^i(CH_4)-S^0(CH_4)}{S^i(CH_4)} \tag{4.18}$$

Using equations 4.17 and 4.18, the segmental reaction rates of methane formation through CO and CO_2 hydrogenation as well as their ratio ($r^{CO}(CH_4)/r^0(CH_4)$) were calculated to demonstrate how the contribution of the primary CO_2 methanation and secondary CO hydrogenation pathways to overall CH_4 production depends on the kind of alkali metal promoter and Rb loading. The obtained results are presented in the form of spatial profiles of the segmental rates to show their changes along the catalyst bed (Figure 4.44 and Figure 4.45).
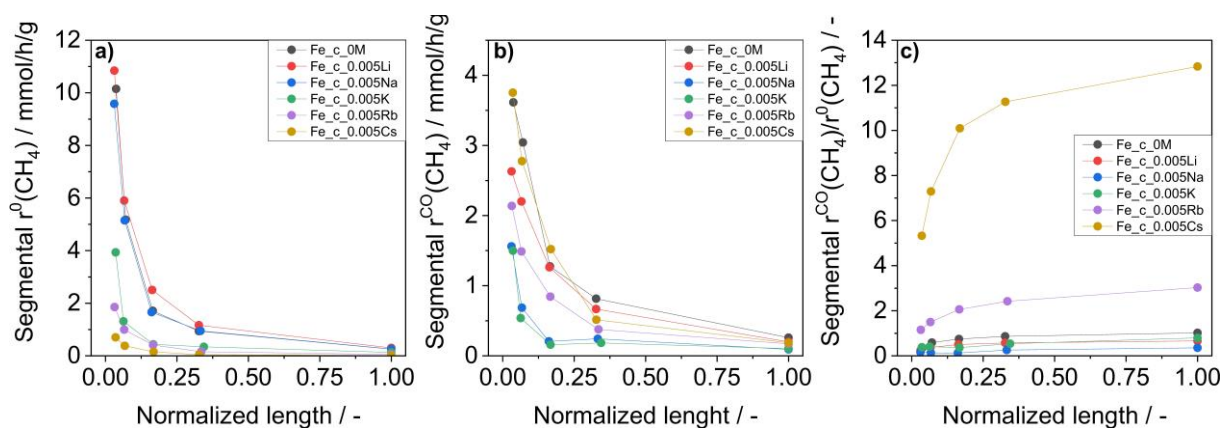
Figure 4.44. Spatial profiles of (a) segmental CO_2 methanation rate ($r^0(CH_4)$), (b) segmental CO hydrogenation to CH_4 rate ($r^{CO}(CH_4)$), (c) the ratio of CO and CO_2 hydrogenation rates to CH_4 over the magnetite-containing catalysts promoted with different kind of alkali metal.

It is seen in Figure 4.44 that the kind of the alkali metal promoter has a decisive effect on the impact of primary and secondary methane formation routes to the overall methane production. For all catalysts, an uprising tendency of $r^{CO}(CH_4)/r^0(CH_4)$ was established with rising CO_2 conversion (Figure 4.44c). It could be the consequence of rising CO and decreasing CO_2 partial pressures along the catalyst bed. The dependency yet is not very strong for the Fe_c_0M catalyst and the highest ratio value is below 1. This means that the direct CO_2 methanation pathway has higher impact on the overall methane production over this catalyst than the CO hydrogenation route. The addition of Li or Na hinders the latter pathway but only slightly affects the primary CO_2 hydrogenation rate. As a consequence, the $r^{CO}(CH_4)/r^0(CH_4)$ ratio for these promoted samples is lower in comparison with the unpromoted catalyst (Figure 4.44). In other words, the direct methanation is the dominant route of methane formation over Li- or Na-containing catalysts. As this pathway is almost not affected by the promoters, the low hindering effect on the overall methane production is observed as could be seen from the methane segmental formation rate (Figure 4.39c). The $r^{CO}(CH_4)/r^0(CH_4)$ ratio over Fe_c_0.005K is also lower than the one determined for the unpromoted catalyst. However, unlike Li- or Na-containing materials both CO and CO_2 hydrogenation rates are affected by potassium promoter. But secondary CO hydrogenation pathway is suppressed stronger than the direct methanation route. Therefore, the CO_2 hydrogenation to CH_4 as well prevails over K-promoted catalyst. For Fe_c_0.005Rb and Fe_c_0.005Cs, the direct CO_2 methanation is significantly suppressed, while the CO hydrogenation rate is moderately hindered over Rb-containing catalyst and is almost not affected by Cs promoter in comparison with the unpromoted counterpart (Figure 4.44a,b). Therefore, a decrease in the overall production of methane is observed. As reflected in the

$r^{CO}(CH_4)/r^0(CH_4)$ ratio for Rb- or Cs-promoted materials, the dominant pathway of methane formation over these catalysts is the secondary hydrogenation of CO, while the direct methanation route is drastically suppressed.

Concerning the effect of Rb loading on methane formation, it could be established that the higher its content, the higher the $r^{CO}(CH_4)/r^0(CH_4)$ ratio is (Figure 4.45c). That means that CO hydrogenation route becomes more prominent with rising amount of Rb dopant. This is a result of a significant decrease in the direct CO_2 methanation rate and a moderate increase in CO hydrogenation rate to CH_4 with rising Rb content (Figure 4.45a,b). While the direct correlation could be established between the content of Rb promoter and the decrease in $r^0(CH_4)$, no direct dependency between the amount of the alkali metal and the increase in $r^{CO}(CH_4)$ was determined. Moreover, the strength of this increase is meaningfully lower than the decrease in the CO_2 hydrogenation rate to CH_4. Therefore, the hindering effect of Rb on the overall methane production is observed.
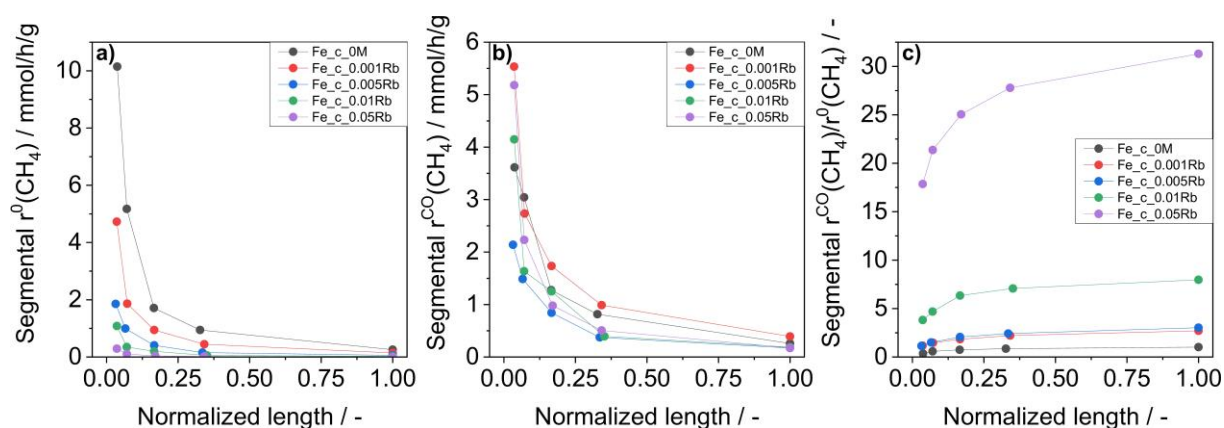
Figure 4.45. Spatial profiles of (a) segmental CO_2 methanation rate ($r^0(CH_4)$), (b) segmental CO hydrogenation to CH_4 rate ($r^{CO}(CH_4)$), (c) the ratio of CO and CO_2 hydrogenation rates to CH_4 over the magnetite-containing catalysts promoted with different amount of Rb.

4.3.5 Summary

A series of magnetite-containing catalysts promoted with different alkali metals (Li, Na, K, Rb or Cs) and different amounts of Rb (the Rb/Fe ratio is 0.001, 0.005, 0.01 and 0.05) were synthesized through controlled decomposition of commercial iron (II) oxalate dihydrate promoted with carbonate of the corresponding alkali metal through incipient wetness impregnation. Neither the kind nor the amount of promoter was identified to affect the phase composition and the morphology of as-prepared catalysts. When varying the kind of promoter,

no effect was also established for overall catalyst reducibility with exception for the Na dopant. However, when the concentration of Rb promoter was increased, a significant shift of the iron carbides reduction peak maximum was observed. Therefore, it could be assumed that any alkali metal increases the reducibility, but the manifestation of the effect depends individually on the amount of the promoter.

A particular focus was put on investigating the promoter effect on product formation in CO_2-FTS from a kinetic viewpoint. The promoter does not change the general pathways of CO_2 conversion into CO, CH_4 and C_{2+}-hydrocarbons. There is, however, a clear effect of the promoter on the individual reaction steps and the overall CO_2 consumption rate. The electronegativity of the alkali metal according to the Pauling scale was determined to be an important descriptor positively influencing the CO_2 hydrogenation rate. Any alkali metal enhances the selectivity to C_{2+}-hydrocarbons and hinders the selectivity to CH_4. However, the origin of the latter effect depends on the kind of the promoter. Owning to a novel approach of kinetic analysis it was possible to distinguish the contributions of direct CO_2 ($r^0(CH_4)$) and secondary CO ($r^{CO}(CH_4)$) methanation routes to the overall methane production. The addition of Li or Na moderately lowers the CO hydrogenation rate but almost does not affect the direct CO_2 methanation rate in comparison with the unpromoted catalyst. That is why these dopants have low hindering effect on the overall methane production. Both CO and CO_2 methanation pathways are hindered in the presence of K promoter. CO_2 hydrogenation to CH_4 is the dominant route to this product over unpromoted, Li-, Na- or K-containing catalysts as concluded from the $r^{CO}(CH_4)/r^0(CH_4)$ ratio values. On the contrary, the direct CO_2 methanation is significantly suppressed over Rb- or Cs-promoted catalysts. The secondary CO hydrogenation is the main route of methane production over these catalysts. The highest selectivity to C_{2+}-hydrocarbons and the highest $O(C_2-C_4)/P(C_2-C_4)$ ratio as well as the lowest selectivity to CH_4 were obtained over catalysts promoted with K, Rb or Cs.

Any amount of Rb promoter positively influences the selectivity to C_{2+}-hydrocarbons and hinders the selectivity to CH_4 as well as enhances the $O(C_2-C_4)/P(C_2-C_4)$ ratio. There is, however, an optimal Rb/Fe ratio to achieve the highest performance. A decrease in the direct methanation rate but an increase in the CO hydrogenation rate to CH_4 were determined with rising Rb concentration. The suppressed overall methane formation is achieved because the strength of the hindering effect on CO_2 hydrogenation is meaningfully higher than the increase in the CO hydrogenation rate.

5 Conclusions

The present study has demonstrated that tailored decomposition of iron (II) oxalate dihydrate is a suitable method for the generation of mixed-phase bulk iron-containing catalysts with tunable fractions of Fe_3O_4, FeO, Fe, Fe_3C and/or Fe_5C_2 phases as well as for the preparation of single-phase α-Fe_2O_3 with different crystallite size or mixed-phase iron (III) oxide with adjustable α-/γ-Fe_2O_3 ratio. Such purposeful synthesis allows the unambiguous understanding of the transformation of iron-containing phases under conditions of CO_2 hydrogenation to higher hydrocarbons as well as the elucidation of the effects of initial composition and its structural parameters (crystallite size) on the catalytic performance. The potential of the introduced approach for preparation of selective catalysts is clearly demonstrated through the comparison of the achieved catalytic performance with that previously reported in literature. The developed Fe-based catalysts are on the level with the top 3 best-performing state-of-the-art materials in terms of suppressed selectivity to methane and enhanced olefin/paraffin ratio within C_2-C_4 hydrocarbons.

Reaction pathways of CO_2 hydrogenation to CO, CH_4 and higher hydrocarbons were established to be not dependent on the initial composition of Fe-based catalysts because of reaction-induced structural changes. Fe_3O_4, Fe_5C_2, Fe_3C (to a lesser extent) and Fe (to a lesser extent) are the main phases present in steady-state catalysts. For all investigated catalysts, CO is the main primary product, taking part in further hydrogenation to CH_4 and higher hydrocarbons. Two additional routes of CH_4 formation were established, which are the direct CO_2 methanation and hydrogenolysis of higher hydrocarbons. The latter reaction plays a role over unpromoted magnetite-based catalysts.

It was demonstrated that steady-state catalyst composition changes along the catalyst bed. Fe_5C_2 is the major component in the upstream located catalyst layers. Its concentration decreases downstream in favor of Fe_3O_4. The iron carbide spatial distribution depends on partial pressures of CO and H_2O participating in Fe carburization to Fe_5C_2 and Fe/Fe_5C_2 oxidation to Fe_3O_4, respectively. The iron carbide ability to consume CO determines the strength of the decrease in the ratio of CO/H_2O along the catalysts bed and the spatial distribution of Fe_5C_2 and Fe_3O_4. In view of spatial catalyst composition profiles, the performance – composition relationships can be unambiguously established when the catalysts are compared at a similar degree of CO_2 conversion. Thus, a positive correlation between the fraction of iron carbides in spent catalysts and the selectivity to C_{2+}-hydrocarbons was determined. Metallic Fe was shown to participate

in CO hydrogenation to CH_4. Beside the RWGS reaction, Fe_3O_4 is also active in CO_2 hydrogenation to CH_4 but to a lesser extent.

The reducibility of differently composed Fe-based catalysts, which could be controlled through varying the initial composition ($Fe_xO_yC_z$, α-/γ-Fe_2O_3) or the crystallite size of α-Fe_2O_3, was proved to be an important factor affecting the overall CO_2 conversion rate. Higher reducibility not only increases the CO_2 consumption rate but also lowers the impact of direct CO_2 methanation and increases the impact of CO hydrogenation to CH_4 into overall methane formation. The inhibiting effect of CO_2 methanation is, however, stronger than the promoting effect of CO hydrogenation to CH_4.

The morphology of iron (II) oxalate dihydrate was shown to have the largest influence on the selectivity to methane because it determines the defectiveness of Fe_5C_2, which is expressed as the ratio of C/Fe. Defective-lesser carbides possess lower reactivity towards CO_x hydrogenation and, therefore, are present in higher amount in down-stream located catalyst layers in comparison with defective-richer iron carbides. The lower deviation from the stochiometric composition results in suppressed activity of such Fe_5C_2 to activate H_2 and to strongly adsorb CO and CO_2. As a consequence, the overall CO_2 consumption reaction rate decreases, but lower selectivity to methane and higher olefin to paraffin (among C_2-C_4 hydrocarbons) as well as C_{2+}/CH_4 ratios are achieved.

A positive correlation between the electronegativity (the Pauling scale) of alkali metal promoters for magnetite-containing materials and the overall CO_2 consumption rate was established. Any promoter enhances the C_{2+}-hydrocarbons selectivity and suppresses the selectivity to CH_4. Such correlation suggests that the promoting effect is achieved because of metal electronic interactions. A promoter donates electronic density to Fe and increases its basicity, which leads to the stronger adsorption of CO_2 on a surface and, consequently, to a higher C/H ratio. The addition of Li and Na lowers the CO hydrogenation rate to CH_4 but almost does not affect the direct CO_2 methanation rate in comparison with the unpromoted catalyst. This is the reason why these dopants have low hindering effect on the overall methane production. The best-performed catalysts in terms of the highest selectivity to C_{2+}-hydrocarbons and the O(C_2-C_4)/P(C_2-C_4) ratio and the lowest selectivity to CH_4 contain K, Rb or Cs promoters. The both pathways of methane production are suppressed over K-promoted material in comparison with unpromoted catalyst. As concluded from the $r^{CO}(CH_4)/r^0(CH_4)$ ratio values CO_2 direct methanation is the main pathway of methane formation over unpromoted, Li-, Na- or K-containing catalysts. This route, on the other hand, is significantly suppressed over Rb- or

Cs-promoted catalysts, while the CO hydrogenation rate is moderately hindered over Rb-containing catalyst and is almost not affected by Cs promoter. Therefore, CO hydrogenation to CH_4 prevails over these catalysts.

Any amount of Rb promoter enhances the selectivity to C_{2+}-hydrocarbons and the $O(C_2$-$C_4)/P(C_2$-$C_4)$ ratio as well as hinders the selectivity to CH_4. Nevertheless, there is an optimal Rb amount ensuring the highest performance. The contribution of CO hydrogenation route into overall CH_4 production becomes more prominent with rising amount of Rb dopant. The reason for this is a decrease in the direct CO_2 methanation rate accompanied with an increase in CO hydrogenation rate to CH_4 with increasing Rb content. The strength of the increase, however, is meaningfully lower than the decrease in the CO_2 hydrogenation rate to CH_4, which determines the hindering effect of Rb promoter on the overall methane production.

6 Outlook

As was shown in the present study, iron carbides forming mostly in the up-stream layers of the catalyst bed upon progressing the CO_2 conversion are likely to be active in all reactions occurring during the CO_2-FTS. The morphology of iron carbides could significantly differ and has the largest influence on the product distribution. The defectiveness of Fe_5C_2 expressed as the ratio of C/Fe was proved to affect the adsorption of CO, CO_2 and H_2. These interactions control the C/H ratio on the surface of iron carbide and, consequently, the product selectivity. Therefore, the approach suggested in the present study should be further applied to get deeper insights in the factors affecting (i) distribution of iron carbides along the catalyst bed under CO_2-FTS conditions, (ii) defect structure of iron carbides, and (iii) the relationships between structural characteristics of iron carbides and their ability to activate H_2, CO and CO_2. Moreover, the fundamentals determining the resistance of iron carbides against irreversible oxidation to iron oxides by water under reaction conditions should be elucidated. Such knowledge would be of high importance to control iron carbide distribution from up-stream to down-stream catalyst layers because the concentration of water formed in CO_2-FTS increases accordingly.

From an engineering point of view, the negative effect of increasing concentration of water could be partly mitigated by exploiting two consequently connected reactors. The upstream located reactor is used for the RWGS reaction. The generated dry (after water condensation) feed is directed to the downstream-located reactor filled with a CO-FTS or CO_2-FTS catalyst. The feed ratio of CO/CO_2/H_2 for the latter reaction can be controlled through operation conditions of the upstream located reactor. Another engineering possibility to increase iron carbide content along the catalyst bed and, consequently, the conversion of CO_2 and selectivity to C_{2+}-hydrocarbons could potentially be the usage of a reverse-flow reactor. The feed mixture in such reactor is introduced from an "inlet" followed by the change of the flow direction: gases are fed from an "outlet". Periodical switches in the flow direction would not allow to reach the steady-state catalyst composition. If the rate of the carburization of Fe_3O_4 by CO is higher than the rate of Fe_5C_2 oxidation by water, an optimal regime of switching time could be found for the formation of the catalyst composition composed mostly of iron carbides.

References

[1] D. Luthi, M. Le Floch, B. Bereiter, T. Blunier, J.M. Barnola, U. Siegenthaler, D. Raynaud, J. Jouzel, H. Fischer, K. Kawamura, T.F. Stocker, High-resolution carbon dioxide concentration record 650,000-800,000 years before present, Nature, 453 (2008) 379-382.

[2] M.K. van Aalst, The impacts of climate change on the risk of natural disasters, Disasters, 30 (2006) 5-18.

[3] S.E. Schwartz, Uncertainty in climate sensitivity: Causes, consequences, challenges, Energy Environ. Sci., 1 (2008) 430-453.

[4] B. Metz, O. Davidson, H.d. Coninck, M. Loos, L. Meyer, Carbon dioxide capture and storage, 2005.

[5] I.E. Agency, Key World Energy Statistics, 2020.

[6] Y.A. Daza, J.N. Kuhn, CO_2 conversion by reverse water gas shift catalysis: comparison of catalysts, mechanisms and their consequences for CO_2 conversion to liquid fuels, RSC Adv., 6 (2016) 49675-49691.

[7] J. Kemper, Biomass and carbon dioxide capture and storage: A review, Int. J. Greenh. Gas Control., 40 (2015) 401-430.

[8] W. Wang, S. Wang, X. Ma, J. Gong, Recent advances in catalytic hydrogenation of carbon dioxide, Chem Soc Rev, 40 (2011) 3703-3727.

[9] E.V. Kondratenko, G. Mul, J. Baltrusaitis, G.O. Larrazabal, J. Perez-Ramirez, Status and perspectives of CO_2 conversion into fuels and chemicals by catalytic, photocatalytic and electrocatalytic processes, Energy Environ. Sci., 6 (2013) 3112-3135.

[10] R.M. Cuéllar-Franca, A. Azapagic, Carbon capture, storage and utilisation technologies: A critical analysis and comparison of their life cycle environmental impacts, J. CO2 Util., 9 (2015) 82-102.

[11] A. Rafiee, K.R. Khalilpour, D. Milani, CO_2 Conversion and Utilization Pathways, Polygeneration with Polystorage for Chemical and Energy Hubs2019, pp. 213-245.

[12] T. Sakakura, J.C. Choi, H. Yasuda, Transformation of carbon dioxide, Chem. Rev., 107 (2007) 2365-2387.

[13] M. Mikkelsen, M. Jørgensen, F.C. Krebs, The teraton challenge. A review of fixation and transformation of carbon dioxide, Energy Environ. Sci., 3 (2010) 43-81.

[14] G.A. Olah, A. Goeppert, G.K.S. Prakash, Chemical Recycling off Carbon Dioxide to Methanol and Dimethyl Ether: From Greenhouse Gas to Renewable, Environmentally Carbon Neutral Fuels and Synthetic Hydrocarbons, J. Org. Chem., 74 (2009) 487-498.

[15] H. Goehna, P. Koenig, Producing methanol from CO_2, Chemtech, 24 (1994) 36-41.

[16] M. Cokoja, C. Bruckmeier, B. Rieger, W.A. Herrmann, F.E. Kuhn, Transformation of carbon dioxide with homogeneous transition-metal catalysts: a molecular solution to a global challenge?, Angew Chem Int Ed Engl, 50 (2011) 8510-8537.

[17] R. Zevenhoven, S. Eloneva, S. Teir, Chemical fixation of CO_2 in carbonates: Routes to valuable products and long-term storage, Catal. Today, 115 (2006) 73-79.

[18] X.D. Xu, J.A. Moulijn, Mitigation of CO_2 by chemical conversion: Plausible chemical reactions and promising products, Energy & Fuels, 10 (1996) 305-325.

[19] F. Pontzen, W. Liebner, V. Gronemann, M. Rothaemel, B. Ahlers, CO_2-based methanol and DME - Efficient technologies for industrial scale production, Catal. Today, 171 (2011) 242-250.

[20] http://www.carbonrecycling.is, 2011.

[21] Y.F. Zhao, Y. Yang, C. Mims, C.H.F. Peden, J. Li, D.H. Mei, Insight into methanol synthesis from CO_2 hydrogenation on Cu(111): Complex reaction network and the effects of H_2O, J. Catal., 281 (2011) 199-211.

[22] X.M. Guo, D.S. Mao, G.Z. Lu, S. Wang, G.S. Wu, The influence of La doping on the catalytic behavior of Cu/ZrO$_2$ for methanol synthesis from CO$_2$ hydrogenation, J. Mol. Catal. A, 345 (2011) 60-68.

[23] A. Bansode, B. Tidona, P.R. von Rohr, A. Urakawa, Impact of K and Ba promoters on CO$_2$ hydrogenation over Cu/Al$_2$O$_3$ catalysts at high pressure, Catal. Sci. Tech., 3 (2013) 767-778.

[24] K.H. Sun, Z.G. Fan, J.Y. Ye, J.M. Yan, Q.F. Ge, Y.N. Li, W.J. He, W.M. Yang, C.J. Liu, Hydrogenation of CO$_2$ to methanol over In$_2$O$_3$ catalyst, J. CO2 Util., 12 (2015) 1-6.

[25] P. Gao, S.S. Dang, S.G. Li, X.N. Bu, Z.Y. Liu, M.H. Qiu, C.G. Yang, H. Wang, L.S. Zhong, Y. Han, Q. Liu, W. Wei, Y.H. Sun, Direct Production of Lower Olefins from CO$_2$ Conversion via Bifunctional Catalysis, ACS Catal., 8 (2018) 571-578.

[26] Z.L. Li, J.J. Wang, Y.Z. Qu, H.L. Liu, C.Z. Tang, S. Miao, Z.C. Feng, H.Y. An, C. Li, Highly Selective Conversion of Carbon Dioxide to Lower Olefins, ACS Catal., 7 (2017) 8544-8548.

[27] L. Guo, J. Sun, X. Ji, J. Wei, Z. Wen, R. Yao, H. Xu, Q. Ge, Directly converting carbon dioxide to linear α-olefins on bio-promoted catalysts, Commun., 1 (2018).

[28] H.M.T. Galvis, K.P. de Jong, Catalysts for Production of Lower Olefins from Synthesis Gas: A Review, ACS Catal., 3 (2013) 2130-2149.

[29] M. Ronda-Lloret, G. Rothenberg, N.R. Shiju, A Critical Look at Direct Catalytic Hydrogenation of Carbon Dioxide to Olefins, ChemSusChem, 12 (2019) 3896-3914.

[30] N. Madaan, R. Haufe, N.R. Shiju, G. Rothenberg, Oxidative Dehydrogenation of n-Butane: Activity and Kinetics Over VO$_x$/Al$_2$O$_3$ Catalysts, Top. Catal., 57 (2014) 1400-1406.

[31] T. Riedel, G. Schaub, K.W. Jun, K.W. Lee, Kinetics of CO$_2$ hydrogenation on a K-promoted Fe catalyst, Ind. Eng. Chem. Res, 40 (2001) 1355-1363.

[32] U. Olsbye, S. Svelle, M. Bjorgen, P. Beato, T.V.W. Janssens, F. Joensen, S. Bordiga, K.P. Lillerud, Conversion of Methanol to Hydrocarbons: How Zeolite Cavity and Pore Size Controls Product Selectivity, Angew. Chem., Int. Ed., 51 (2012) 5810-5831.

[33] F.R.G. Best, A. Mundstock, G. Drager, P. Rusch, N.C. Bigall, H. Richter, J. Caro, Methanol-to-Olefins in a Membrane Reactor with in situ Steam Removal - The Decisive Role of Coking, ChemCatChem, 12 (2020) 273-280.

[34] X.L. Liu, M.H. Wang, C. Zhou, W. Zhou, K. Cheng, J.C. Kang, Q.H. Zhang, W.P. Deng, Y. Wang, Selective transformation of carbon dioxide into lower olefins with a bifunctional catalyst composed of ZnGa$_2$O$_4$ and SAPO-34, Chem.Commun., 54 (2018) 140-143.

[35] M. Bjorgen, S. Svelle, F. Joensen, J. Nerlov, S. Kolboe, F. Bonino, L. Palumbo, S. Bordiga, U. Olsbye, Conversion of methanol to hydrocarbons over zeolite H-ZSM-5: On the origin of the olefinic species, J. Catal., 249 (2007) 195-207.

[36] S. Svelle, F. Joensen, J. Nerlov, U. Olsbye, K.P. Lillerud, S. Kolboe, M. Bjorgen, Conversion of methanol into hydrocarbons over zeolite H-ZSM-5: Ethene formation is mechanistically separated from the formation of higher alkenes, J. Am. Chem. Soc., 128 (2006) 14770-14771.

[37] J.Q. Chen, A. Bozzano, B. Glover, T. Fuglerud, S. Kvisle, Recent advancements in ethylene and propylene production using the UOP/Hydro MTO process, Catal. Today, 106 (2005) 103-107.

[38] I.M. Dahl, S. Kolboe, On the reaction mechanism for hydrocarbon formation from methanol over SAPO-34 .2. Isotopic labeling studies of the co-reaction of propene and methanol, J. Catal., 161 (1996) 304-309.

[39] P. Tian, Y.X. Wei, M. Ye, Z.M. Liu, Methanol to Olefins (MTO): From Fundamentals to Commercialization, ACS Catal., 5 (2015) 1922-1938.

[40] H.B. Zhang, X.L. Liang, X. Dong, H.Y. Li, G.D. Lin, Multi-Walled Carbon Nanotubes as a Novel Promoter of Catalysts for CO/CO$_2$ Hydrogenation to Alcohols, Catal. Surv. Asia, 13 (2009) 41-58.

[41] P.S.S. Prasad, J.W. Bae, K.W. Jun, K.W. Lee, Fischer-Tropsch Synthesis by Carbon Dioxide Hydrogenation on Fe-Based Catalysts, Catal. Surv. Asia, 12 (2008) 170-183.

[42] B.Z. Yao, W.J. Ma, S. Gonzalez-Cortes, T.C. Xiao, P.P. Edwards, Thermodynamic study of hydrocarbon synthesis from carbon dioxide and hydrogen, GREENH GASES, 7 (2017) 942-957.

[43] J.J. Chen, C. Yang, Thermodynamic Equilibrium Analysis of Product Distribution in the Fischer-Tropsch Process Under Different Operating Conditions, ACS Omega, 4 (2019) 22237-22244.

[44] L. Torrente-Murciano, D. Mattia, M.D. Jones, P.K. Plucinski, Formation of hydrocarbons via CO_2 hydrogenation - A thermodynamic study, J. CO2 Util., 6 (2014) 34-39.

[45] R.W. Dorner, D.R. Hardy, F.W. Williams, B.H. Davis, H.D. Willauer, Influence of Gas Feed Composition and Pressure on the Catalytic Conversion of CO_2 to Hydrocarbons Using a Traditional Cobalt-Based Fischer-Tropsch Catalyst, Energy & Fuels, 23 (2009) 4190-4195.

[46] T. Riedel, H. Schulz, G. Schaub, K.W. Jun, J.S. Hwang, K.W. Lee, Fischer-Tropsch on iron with H_2/CO and H_2/CO_2 as synthesis gases: the episodes of formation of the Fischer-Tropsch regime and construction of the catalyst, Top. Catal., 26 (2003) 41-54.

[47] S. Krishnamoorthy, A.W. Li, E. Iglesia, Pathways for CO_2 formation and conversion during Fischer-Tropsch synthesis on iron-based catalysts, Catal. Lett., 80 (2002) 77-86.

[48] D. Wang, Z.H. Xie, M.D. Porosoff, J.G.G. Chen, Recent advances in carbon dioxide hydrogenation to produce olefins and aromatics, Chem, 7 (2021) 2277-2311.

[49] R.A.F. R. B. Anderson, and H. H. Storch, Fischer-Tropsch Reaction Mechanism Involving Stepwise Growth of Carbon Chain, J. Chem. Phys., 19 (1951) 313-319.

[50] S. Abello, D. Montane, Exploring Iron-based Multifunctional Catalysts for Fischer-Tropsch Synthesis: A Review, ChemSusChem, 4 (2011) 1538-1556.

[51] M.E. Dry, Catalytic aspects of industrial Fischer-Tropsch synthesis, J. Mol. Catal., 17 (1982) 133-144.

[52] W. Zhou, K. Cheng, J.C. Kang, C. Zhou, V. Subramanian, Q.H. Zhang, Y. Wang, New horizon in C_1 chemistry: breaking the selectivity limitation in transformation of syngas and hydrogenation of CO_2 into hydrocarbon chemicals and fuels, Chem. Soc. Rev., 48 (2019) 3193-3228.

[53] M. Janardanarao, Direct catalytic conversion of synthesis gas to lower olefins, Ind. Eng. Chem. Res, 29 (1990) 1735-1753.

[54] G.P. Van der Laan, A. Beenackers, Kinetics and selectivity of the Fischer-Tropsch synthesis: A literature review, Catal. Rev.-Sci. Eng., 41 (1999) 255-318.

[55] B.W. Wojciechowski, The kinetics of the Fischer-Tropsch synthesis, Catal. Rev.-Sci. Eng., 30 (1988) 629-702.

[56] B. Sarup, B.W. Wojciechowski, Studies of the Fischer-Tropsch synthesis on a cobalt catalyst. 1. Evaluation of product distribution parameters from experimental data, Can. J. Chem. Eng., 66 (1988) 831-842.

[57] R.A. Dictor, A.T. Bell, Fischer-Tropsch synthesis over reduced and unreduced irone oxide catalysts, J. Catal., 97 (1986) 121-136.

[58] E.W. Kuipers, C. Scheper, J.H. Wilson, I.H. Vinkenburg, H. Oosterbeek, Non-ASF product distributions due to secondary reactions during Fischer-Tropsch synthesis, J. Catal., 158 (1996) 288-300.

[59] E. Iglesia, S.C. Reyes, R.J. Madon, Transport-enhanced alpha-olefin readsorption pathways in Ru-catalyzed hydrocarbon synthesis, J. Catal., 129 (1991) 238-256.

[60] H. Schulz, K. Beck, E. Erich, Kinetics of Fischer-Tropsch selectivity, Fuel Proc. Techn., 18 (1988) 293-304.

[61] H.M.T. Galvis, J.H. Bitter, C.B. Khare, M. Ruitenbeek, A.I. Dugulan, K.P. de Jong, Supported Iron Nanoparticles as Catalysts for Sustainable Production of Lower Olefins, Science, 335 (2012) 835-838.

[62] E. Schwab, A. Weck, J. Steiner, K. Bay, Syngas to Lower Olefins, Oil Gas-Eur. Mag., 36 (2010) 44-47.

[63] H.M.T. Galvis, A.C.J. Koeken, J.H. Bitter, T. Davidian, M. Ruitenbeek, A.I. Dugulan, K.P. de Jong, Effects of sodium and sulfur on catalytic performance of supported iron catalysts for the Fischer-Tropsch synthesis of lower olefins, J. Catal., 303 (2013) 22-30.

[64] S. Novak, R.J. Madon, H. Suhl, Secondary effects in the Fischer-Tropsch synthesis, J. Catal., 77 (1982) 141-151.

[65] Y.S. Zhang, Y.L. Yao, J.Q. Shen, J.L. Chang, J. Gorimbo, X.Y. Liu, D. Hildebrandt, Effect of ethylene co-feeding in Fischer-Tropsch synthesis: A study of reaction equilibrium and competition, Fuel, 302 (2021).

[66] T. Komaya, A.T. Bell, Estimates of rate coefficients for elementary processes occurring during Fischer-Tropsch synthesis over Ru/TiO_2, J. Catal., 146 (1994) 237-248.

[67] X.D. Zhan, B.H. Davis, Assessment of internal diffusion limitation on Fischer-Tropsch product distribution, Appl. Catal. A, 236 (2002) 149-161.

[68] W. Wang, S.P. Wang, X.B. Ma, J.L. Gong, Recent advances in catalytic hydrogenation of carbon dioxide, Chem. Soc. Rev., 40 (2011) 3703-3727.

[69] D. Tibiletti, A. Goguet, F.C. Meunier, J.P. Breen, R. Burch, On the importance of steady-state isotopic techniques for the investigation of the mechanism of the reverse water-gas-shift reaction, Chem.Commun., (2004) 1636-1637.

[70] J.A. Loiland, M.J. Wulfers, N.S. Marinkovic, R.F. Lobo, $Fe/gamma-Al_2O_3$ and Fe-$K/gamma-Al_2O_3$ as reverse water-gas shift catalysts, Catal. Sci. Tech., 6 (2016) 5267-5279.

[71] H.Y. Yang, C. Zhang, P. Gao, H. Wang, X.P. Li, L.S. Zhong, W. Wei, Y.H. Sun, A review of the catalytic hydrogenation of carbon dioxide into value-added hydrocarbons, Catal. Sci. Tech., 7 (2017) 4580-4598.

[72] R.P. Ye, J. Ding, W.B. Gong, M.D. Argyle, Q. Zhong, Y.J. Wang, C.K. Russell, Z.H. Xu, A.G. Russell, Q.H. Li, M.H. Fan, Y.G. Yao, CO_2 hydrogenation to high-value products via heterogeneous catalysis, Nat. Commun., 10 (2019) 1-15.

[73] A.S. Qingxin Yang, Alexander Matvienko, Henrik Lund, Martin Holena, Evgenii V. Kondratenko, Revealing property-performance relationships for efficient CO_2 hydrogenation to higher hydrocarbons over Fe-based catalysts: Statistical analysis of literature data and its experimental validation, Appl. Catal. B, 282 (2021) 1-11.

[74] W.J. Wang, X. Jiang, X.X. Wang, C.S. Song, Fe-Cu Bimetallic Catalysts for Selective CO_2 Hydrogenation to Olefin-Rich C_{2+} Hydrocarbons, Ind. Eng. Chem. Res, 57 (2018) 4535-4542.

[75] M. Albrecht, U. Rodemerck, M. Schneider, M. Broring, D. Baabe, E.V. Kondratenko, Unexpectedly efficient CO_2 hydrogenation to higher hydrocarbons over non-doped Fe_2O_3, Appl. Catal. B, 204 (2017) 119-126.

[76] J. Tu, M. Ding, Y. Zhang, Y. Li, T. Wang, L. Ma, C. Wang, X. Li, Synthesis of Fe_3O_4-nanocatalysts with different morphologies and its promotion on shifting C_{5+} hydrocarbons for Fischer–Tropsch synthesis, Catal. Commun., 59 (2015) 211-215.

[77] C.G. Visconti, M. Martinelli, L. Falbo, A. Infantes-Molina, L. Lietti, P. Forzatti, G. Iaquaniello, E. Palo, B. Picutti, F. Brignoli, CO_2 hydrogenation to lower olefins on a high surface area K-promoted bulk Fe-catalyst, Appl. Catal. B, 200 (2017) 530-542.

[78] J. Zhu, G.H. Zhang, W.H. Li, X.B. Zhang, F.S. Ding, C.S. Song, X.W. Guo, Deconvolution of the Particle Size Effect on CO_2 Hydrogenation over Iron-Based Catalysts, ACS Catal., 10 (2020) 7424-7433.

[79] T.Z. Chen, W. Jiang, X.L. Sun, W.S. Ning, Y. Liu, G. Xu, G.R. Han, Size-controlled Synthesis of Hematite $alpha-Fe_2O_3$ Nanodisks Closed with (0001) Basal Facets and {11-20} Side Facets and their Catalytic Performance for CO_2 Hydrogenation, ChemistrySelect, 5 (2020) 430-437.

[80] B. Liu, S.S. Geng, J. Zheng, X.L. Jia, F. Jiang, X.H. Liu, Unravelling the New Roles of Na and Mn Promoter in CO_2 Hydrogenation over Fe_3O_4-Based Catalysts for Enhanced Selectivity to Light -Olefins, ChemCatChem, 10 (2018) 4718-4732.

[81] T. Herranz, S. Rojas, F.J. Perez-Alonso, M. Ojeda, P. Terreros, J.L.G. Fierro, Genesis of iron carbides and their role in the synthesis of hydrocarbons from synthesis gas, J. Catal., 243 (2006) 199-211.

[82] D.-B. Cao, Y.-W. Li, J. Wang, H. Jiao, Chain growth mechanism of Fischer–Tropsch synthesis on $Fe_5C_2(001)$, J. Mol. Catal. A, 346 (2011) 55-69.

[83] M. Ding, Y. Yang, J. Xu, Z.C. Tao, H.L. Wang, H. Wang, H.W. Xiang, Y.W. Li, Effect of reduction pressure on precipitated potassium promoted iron-manganese catalyst for Fischer-Tropsch synthesis, Appl. Catal. A, 345 (2008) 176-184.

[84] K.O. Otun, Y.L. Yao, X.Y. Liu, D. Hildebrandt, Synthesis, structure, and performance of carbide phases in Fischer-Tropsch synthesis: A critical review, Fuel, 296 (2021).

[85] Q. Chang, C.H. Zhang, C.W. Liu, Y.X. Wei, A.V. Cheruvathur, A.I. Dugulan, J.W. Niemantsverdriet, X.W. Liu, Y.R. He, M. Qing, L.R. Zheng, Y.F. Yun, Y. Yang, Y.W. Li, Relationship between Iron Carbide Phases (epsilon-Fe_2C, Fe_7C_3, and chi-Fe_5C_2) and Catalytic Performances of Fe/SiO_2 Fischer-Tropsch Catalysts, ACS Catal., 8 (2018) 3304-3316.

[86] X.W. Liu, Z. Cao, S. Zhao, R. Gao, Y. Meng, J.X. Zhu, C. Rogers, C.F. Huo, Y. Yang, Y.W. Li, X.D. Wen, Iron Carbides in Fischer-Tropsch Synthesis: Theoretical and Experimental Understanding in Epsilon-Iron Carbide Phase Assignment, J. Phys. Chem. C, 121 (2017) 21390-21396.

[87] A. Sarkar, D. Seth, A.K. Dozier, J.K. Neathery, H.H. Hamdeh, B.H. Davis, Fischer-tropsch synthesis: Morphology, phase transformation and particle size growth of nano-scale particles, Catal. Lett., 117 (2007) 1-17.

[88] J.C. Park, S. Jang, G.B. Rhim, J.H. Lee, H. Choi, H.D. Jeong, M.H. Youn, D.W. Lee, K.Y. Koo, S.W. Kang, J.I. Yang, H.T. Lee, H. Jung, C.S. Kim, D.H. Chun, A durable nanocatalyst of potassium-doped iron-carbide/alumina for significant production of linear alpha olefins via Fischer-Tropsch synthesis, Appl. Catal. A, 564 (2018) 190-198.

[89] F.J. Perez-Alonso, M. Ojeda, T. Herranz, S. Rojas, J.M. Gonzalez-Carballo, P. Terreros, J.L.G. Fierro, Carbon dioxide hydrogenation over Fe-Ce catalysts, Catal. Commun., 9 (2008) 1945-1948.

[90] R.W. Dorner, D.R. Hardy, F.W. Williams, H.D. Willauer, Heterogeneous catalytic CO_2 conversion to value-added hydrocarbons, Energy Environ. Sci., 3 (2010) 884-890.

[91] H. Ando, Q. Xu, M. Fujiwara, Y. Matsumura, M. Tanaka, Y. Souma, Hydrocarbon synthesis from CO_2 over Fe-Cu catalysts, Catal. Today, 45 (1998) 229-234.

[92] M.K. Gnanamani, G. Jacobs, H.H. Hamdeh, W.D. Shafer, F. Liu, S.D. Hopps, G.A. Thomas, B.H. Davis, Hydrogenation of Carbon Dioxide over Co–Fe Bimetallic Catalysts, ACS Catal., 6 (2016) 913-927.

[93] R.W. Dorner, D.R. Hardy, F.W. Williams, H.D. Willauer, K and Mn doped iron -based CO_2 hydrogenation catalysts: Detection of $KAlH_4$ as part of the catalyst's active phase, Appl. Catal. A, 373 (2010) 112-121.

[94] T. Herranz, S. Rojas, F.J. Pérez-Alonso, M. Ojeda, P. Terreros, J.L.G. Fierro, Hydrogenation of carbon oxides over promoted Fe-Mn catalysts prepared by the microemulsion methodology, Appl. Catal. A, 311 (2006) 66-75.

[95] M. Amoyal, R. Vidruk-Nehemya, M.V. Landau, M. Herskowitz, Effect of potassium on the active phases of Fe catalysts for carbon dioxide conversion to liquid fuels through hydrogenation, J. Catal., 348 (2017) 29-39.

[96] Z.Y. You, W.P. Deng, Q.H. Zhang, Y. Wang, Hydrogenation of carbon dioxide to light olefins over non-supported iron catalyst, Chinese J. Catal., 34 (2013) 956-963.

[97] W.D. Shafer, G. Jacobs, U.M. Graham, H.H. Hamdeh, B.H. Davis, Increased CO_2 hydrogenation to liquid products using promoted iron catalysts, J. Catal., 369 (2019) 239-248.

[98] M.K. Gnanamani, H.H. Hamdeh, W.D. Shafer, S.D. Hopps, B.H. Davis, Hydrogenation of carbon dioxide over iron carbide prepared from alkali metal promoted iron oxalate, Appl. Catal. A, 564 (2018) 243-249.

[99] A. Fedorov, D. Linke, Data analysis of CO_2 hydrogenation catalysts for hydrocarbon production, J. CO2 Util., 61 (2022).

[100] J. Wang, Z. You, Q. Zhang, W. Deng, Y. Wang, Synthesis of lower olefins by hydrogenation of carbon dioxide over supported iron catalysts, Catal. Today, 215 (2013) 186-193.

[101] B.L. Liang, H.M. Duan, T. Sun, J.G. Ma, X. Liu, J.H. Xu, X. Su, Y.Q. Huang, T. Zhang, Effect of Na Promoter on Fe-Based Catalyst for CO_2 Hydrogenation to Alkenes, ACS Sustain. Chem. Eng., 7 (2019) 925-932.

[102] C.Y. Wei, W.F. Tu, L.Y. Jia, Y.Y. Liu, H.L. Lian, P. Wang, Z.Z. Zhang, The evolutions of carbon and iron species modified by Na and their tuning effect on the hydrogenation of CO_2 to olefins, Appl. Surf. Sci., 525 (2020) 13.

[103] X.L. Liu, C. Zhang, P.F. Tian, M.J. Xu, C.X. Cao, Z.X. Yang, M.H. Zhu, J. Xu, Revealing the Effect of Sodium on Iron-Based Catalysts for CO_2 Hydrogenation: Insights from Calculation and Experiment, J. Phys. Chem. C, 125 (2021) 7637-7646.

[104] T. Numpilai, N. Chanlek, Y. Poo-Arporn, S. Wannapaiboon, C.K. Cheng, N. Siri-Nguan, T. Sornchamni, P. Kongkachuichay, M. Chareonpanich, G. Rupprechter, J. Limtrakul, T. Witoon, Pore size effects on physicochemical properties of Fe-Co/K-Al_2O_3 catalysts and their catalytic activity in CO_2 hydrogenation to light olefins, Appl. Surf. Sci., 483 (2019) 581-592.

[105] T.Z. Xie, J.Y. Wang, F.S. Ding, A.F. Zhang, W.H. Li, X.W. Guo, C.S. Song, CO_2 hydrogenation to hydrocarbons over alumina-supported iron catalyst: Effect of support pore size, J. CO2 Util., 19 (2017) 202-208.

[106] V. Rao, A.L. Shashimohan, A.B. Biswas, Studies on the formation of γ-Fe_2O_3 (maghemite) by thermal decomposition of ferrous oxalate dihydrate, J. Mater. Sci., 9 (1974) 430-433.

[107] R. Zboril, M. Mashlan, K. Barcova, M. Vujtek, Thermally induced solid-state syntheses of gamma-Fe_2O_3 nanoparticles and their transformation to alpha-Fe_2O_3 via epsilon-Fe_2O_3, Hyperfine Interact., 139 (2002) 597-606.

[108] R. Zboril, M. Mashlan, D. Petridis, Iron(III) oxides from thermal processes-synthesis, structural and magnetic properties, Mossbauer spectroscopy characterization, and applications, Chem. Mater., 14 (2002) 969-982.

[109] P. Hermankova, M. Hermanek, R. Zboril, Thermal Decomposition of Ferric Oxalate Tetrahydrate in Oxidative and Inert Atmospheres: The Role of Ferrous Oxalate as an Intermediate, Eur. J. Inorg. Chem., (2010) 1110-1118.

[110] M. Hermanek, R. Zboril, Polymorphous Exhibitions of Iron(III) Oxide during Isothermal Oxidative Decompositions of Iron Salts: A Key Role of the Powder Layer Thickness, Chem. Mater., 20 (2008) 5284-5295.

[111] M. Hermanek, R. Zboril, M. Mashlan, L. Machala, O. Schneeweiss, Thermal behaviour of iron(II) oxalate dihydrate in the atmosphere of its conversion gases, J. Mater. Chem., 16 (2006) 1273-1280.

[112] A. Angermann, J. Topfer, Synthesis of magnetite nanoparticles by thermal decomposition of ferrous oxalate dihydrate, J. Mater. Sci., 43 (2008) 5123-5130.

[113] J. Kopp, P. Novak, J. Kaslik, J. Pechousek, Preparation of Magnetite by Thermally Induced Decomposition of Ferrous Oxalate Dihydrate in the Combined Atmosphere, Acta Chim. Slov., 66 (2019) 455-465.

[114] V. Carles, P. Alphonse, P. Tailhades, A. Rousset, Study of thermal decomposition of $FeC_2O_4*2H_2O$ under hydrogen, Thermochim. Acta, 334 (1999) 107-113.

[115] J.T. Gleaves, G.S. Yablonskii, P. Phanawadee, Y. Schuurman, TAP-2: An interrogative kinetics approach, Appl. Catal. A, 160 (1997) 55-88.

[116] J. Perez-Ramirez, E.V. Kondratenko, Evolution, achievements, and perspectives of the TAP technique, Catal. Today, 121 (2007) 160-169.

[117] K. Morgan, N. Maguire, R. Fushimi, J.T. Gleaves, A. Goguet, M.P. Harold, E.V. Kondratenko, U. Menon, Y. Schuurman, G.S. Yablonsky, Forty years of temporal analysis of products, Catal. Sci. Tech., 7 (2017) 2416-2439.

[118] M. Rothaemel, M. Baerns, Modeling and simulation of transient adsorption and reaction in vacuum using the temporal analysis of products reactor, Ind. Eng. Chem. Res, 35 (1996) 1556-1565.

[119] M. Soick, D. Wolf, M. Baerns, Determination of kinetic parameters for complex heterogeneous catalytic reactions by numerical evaluation of TAP experiments, Chem. Eng. Sci., 55 (2000) 2875-2882.

[120] A. Davydov, In Molecular Spectroscopy of Oxide Catalyst Surfaces, John Wiley & Sons2003.

[121] F. Mirabella, E. Zaki, F. Ivars-Barcelo, S. Schauermann, S. Shaikhutdinov, H.J. Freund, CO_2 Adsorption on Magnetite Fe_3O_4(111), J. Phys. Chem. C, 122 (2018) 27433-27441.

[122] A. Boudjemaa, C. Daniel, C. Mirodatos, M. Trari, A. Auroux, R. Bouarab, In situ DRIFTS studies of high-temperature water-gas shift reaction on chromium-free iron oxide catalysts, C. R. Chim., 14 (2011) 534-538.

[123] B.L. Hou, H.Y. Zhang, H.Z. Li, Q.S. Zhu, Study on Kinetics of Iron Oxide Reduction by Hydrogen, Chinese J. Chem. Eng., 20 (2012) 10-17.

[124] J. Kirchner, Z. Baysal, S. Kureti, Activity and Structural Changes of Fe-based Catalysts during CO_2 Hydrogenation towards CH_4 - A Mini Review, ChemCatChem, 12 (2020) 981-988.

[125] J. Zielinski, I. Zglinicka, L. Znak, Z. Kaszkur, Reduction of Fe_2O_3 with hydrogen, Appl. Catal. A, 381 (2010) 191-196.

[126] M.S. Liang, W.K. Kang, K.C. Xie, Comparison of reduction behavior of Fe_2O_3, ZnO and $ZnFe_2O_4$ by TPR technique, J. Nat. Gas Chem., 18 (2009) 110-113.

[127] W.K. Jozwiak, E. Kaczmarek, T.P. Maniecki, W. Ignaczak, W. Maniukiewicz, Reduction behavior of iron oxides in hydrogen and carbon monoxide atmospheres, Appl. Catal. A, 326 (2007) 17-27.

[128] G. Righi, R. Magri, Reduction and Oxidation of Maghemite (001) Surfaces: The Role of Iron Vacancies, J. Phys. Chem. C, 123 (2019) 15648-15658.

[129] L. Machala, R. Zboril, A. Gedanken, Amorphous iron(III) Oxide - A review, J. Phys. Chem. B, 111 (2007) 4003-4018.

[130] J. Zhu, P. Wang, X. Zhang, G. Zhang, R. Li, W. Li, T.P. Senftle, W. Liu, J. Wang, Y. Wang, A. Zhang, Q. Fu, C. Song, X. Guo, Dynamic structural evolution of iron catalysts involving competitive oxidation and carburization during CO_2 hydrogenation, Sci. Adv, 8 (2022) 1-12.

[131] X.W. Liu, S. Zhao, Y. Meng, Q. Peng, A.K. Dearden, C.F. Huo, Y. Yang, Y.W. Li, X.D. Wen, Mossbauer Spectroscopy of Iron Carbides: From Prediction to Experimental Confirmation, Sci. Rep, 6 (2016) 1-10.

[132] O. Malina, P. Jakubec, J. Kaslik, J. Tucek, R. Zboril, A simple high-yield synthesis of high-purity Hagg carbide (chi- Fe_5C_2) nanoparticles with extraordinary electrochemical properties, Nanoscale, 9 (2017) 10440-10446.

[133] F. Jiang, B. Liu, S.S. Geng, Y.B. Xu, X.H. Liu, Hydrogenation of CO_2 into hydrocarbons: enhanced catalytic activity over Fe-based Fischer-Tropsch catalysts, Catal. Sci. Tech., 8 (2018) 4097-4107.

[134] M. Al-Dossary, A.A. Ismail, J.L.G. Fierro, H. Bouzid, S.A. Al-Sayari, Effect of Mn loading onto MnFeO nanocomposites for the CO_2 hydrogenation reaction, Appl. Catal. B, 165 (2015) 651-660.

[135] Y.H. Choi, Y.J. Jang, H. Park, W.Y. Kim, Y.H. Lee, S.H. Choi, J.S. Lee, Carbon dioxide Fischer-Tropsch synthesis: A new path to carbon-neutral fuels, Appl. Catal. B, 202 (2017) 605-610.

[136] J.L. Zhang, S.P. Lu, X.J. Su, S.B. Fan, Q.X. Ma, T.S. Zhao, Selective formation of light olefins from CO_2 hydrogenation over Fe-Zn-K catalysts, J. CO2 Util., 12 (2015) 95-100.

[137] J. Wei, J. Sun, Z.Y. Wen, C.Y. Fang, Q.J. Ge, H.Y. Xu, New insights into the effect of sodium on Fe_3O_4-based nanocatalysts for CO_2 hydrogenation to light olefins, Catal. Sci. Tech., 6 (2016) 4786-4793.

[138] X. Cui, P. Gao, S.G. Li, C.G. Yang, Z.Y. Liu, H. Wang, L.S. Zhong, Y.H. Sun, Selective Production of Aromatics Directly from Carbon Dioxide Hydrogenation, ACS Catal., 9 (2019) 3866-3876.

[139] J. Wei, Q.J. Ge, R.W. Yao, Z.Y. Wen, C.Y. Fang, L.S. Guo, H.Y. Xu, J. Sun, Directly converting CO_2 into a gasoline fuel, Nat. Commun., 8 (2017) 1-8.

[140] S.S. Geng, F. Jiang, Y.B. Xu, X.H. Liu, Iron-Based Fischer-Tropsch Synthesis for the Efficient Conversion of Carbon Dioxide into Isoparaffins, ChemCatChem, 8 (2016) 1303-1307.

[141] J.S. Hong, J.S. Hwang, K.W. Jun, J.C. Sur, K.W. Lee, Deactivation study on a coprecipitated Fe-Cu-K-Al catalyst in CO_2 hydrogenation, Appl. Catal. A, 218 (2001) 53-59.

[142] J.S. Kim, S. Lee, S.B. Lee, M.J. Choi, K.W. Lee, Performance of catalytic reactors for the hydrogenation of CO_2 to hydrocarbons, Catal. Today, 115 (2006) 228-234.

[143] S.R. Yan, K.W. Jun, J.S. Hong, M.J. Choi, K.W. Lee, Promotion effect of Fe-Cu catalyst for the hydrogenation of CO_2 and application to slurry reactor, Appl. Catal. A, 194 (2000) 63-70.

[144] B.L. Liang, T. Sun, J.G. Ma, H.M. Duan, L. Li, X.L. Yang, Y.R. Zhang, X. Su, Y.Q. Huang, T. Zhang, Mn decorated Na/Fe catalysts for CO_2 hydrogenation to light olefins, Catal. Sci. Tech., 9 (2019) 456-464.

[145] N. Meiri, Y. Dinburg, M. Amoyal, V. Koukouliev, R.V. Nehemya, M.V. Landau, M. Herskowitz, Novel process and catalytic materials for converting CO_2 and H_2 containing mixtures to liquid fuels and chemicals, Faraday Discuss., 183 (2015) 197-215.

[146] X.J. Su, J.L. Zhang, S.B. Fan, Q.X. Ma, T.S. Zhao, Effect of preparation of Fe-Zr-K catalyst on the product distribution of CO_2 hydrogenation, RSC Adv., 5 (2015) 80196-80202.
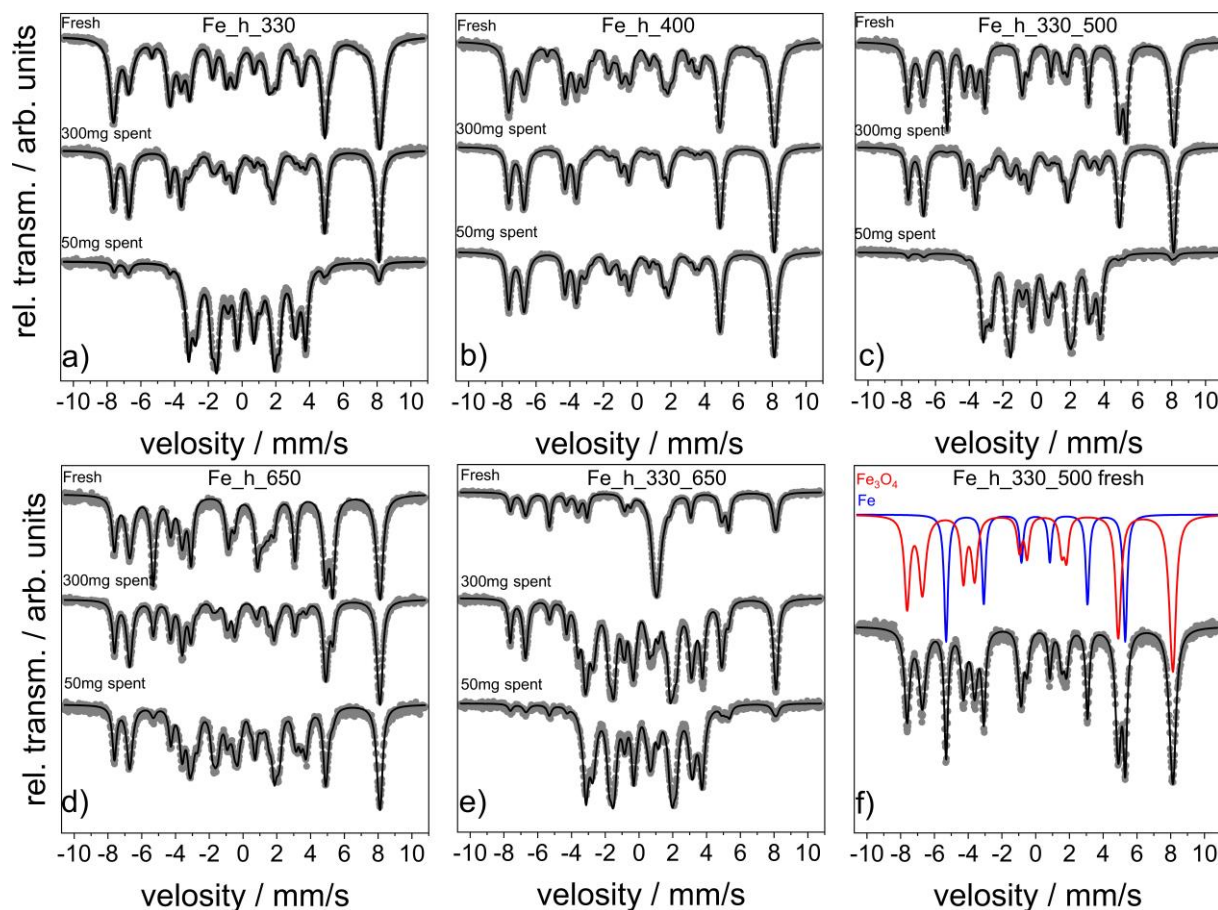
Appendix

Figure A.1. Mössbauer spectra of fresh and spent (after CO_2 hydrogenation tests with 300 or 50 mg over 95 h on stream at 300 °C and total feed flow of 5.85 mL/min) catalysts: (a) Fe_h_330, (b) Fe_h_330_500, (c) Fe_h_330_650, (d) Fe_h_400 and (e) Fe_h_650. Gray dots and black lines represent experimental spectra and fits, respectively. (f) An example of spectrum deconvolution using Lorentzian functions representing different Fe-containing phases in the fresh Fe_h_330_500 sample.
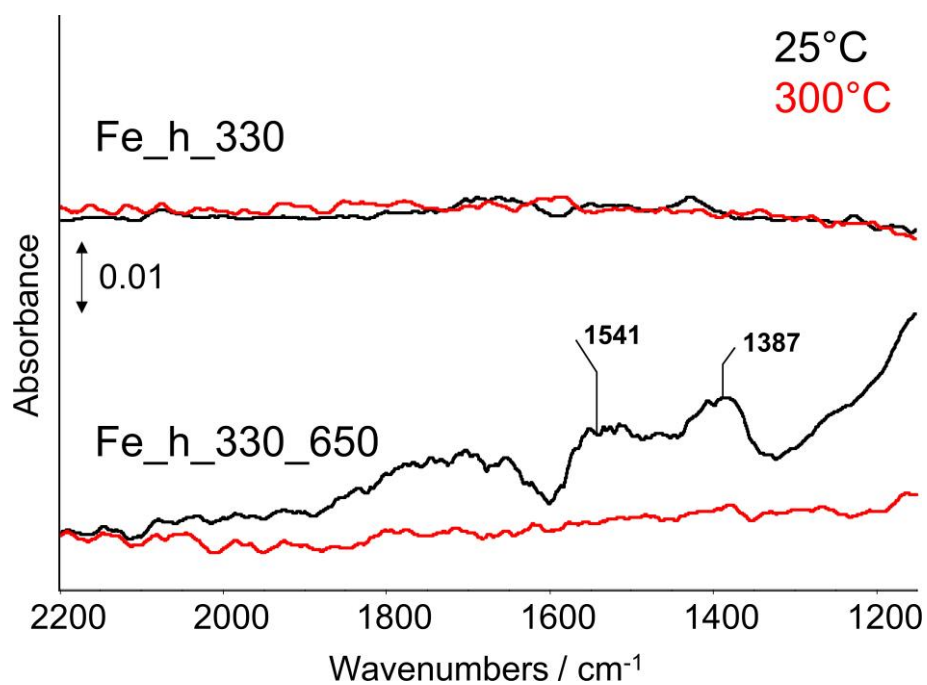
Figure A.2. DRIFT spectra recorded after 30 min exposure of Fe_h_330 and Fe_h_330_650 to CO_2:He (1:1) 25 mL/min at 25 and 300 °C.
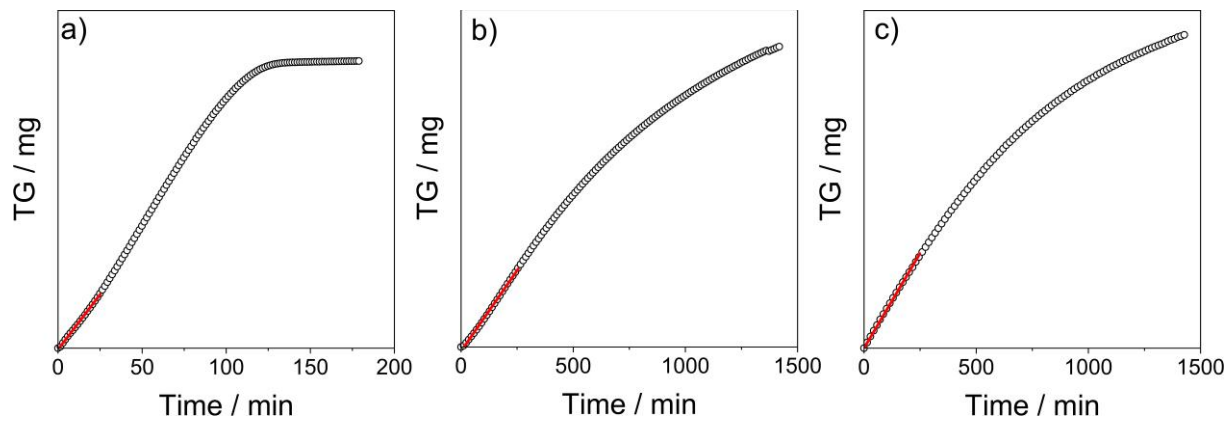
Figure A.3.   An example of the calculation of an initial rate of (a) reduction with H_2 (H_2:He = 1:1) (b) subsequent reoxidation and (c) oxidation with CO_2 (CO_2:He = 1:1) using linear part of the TGA curves for Fe_330_500 sample.
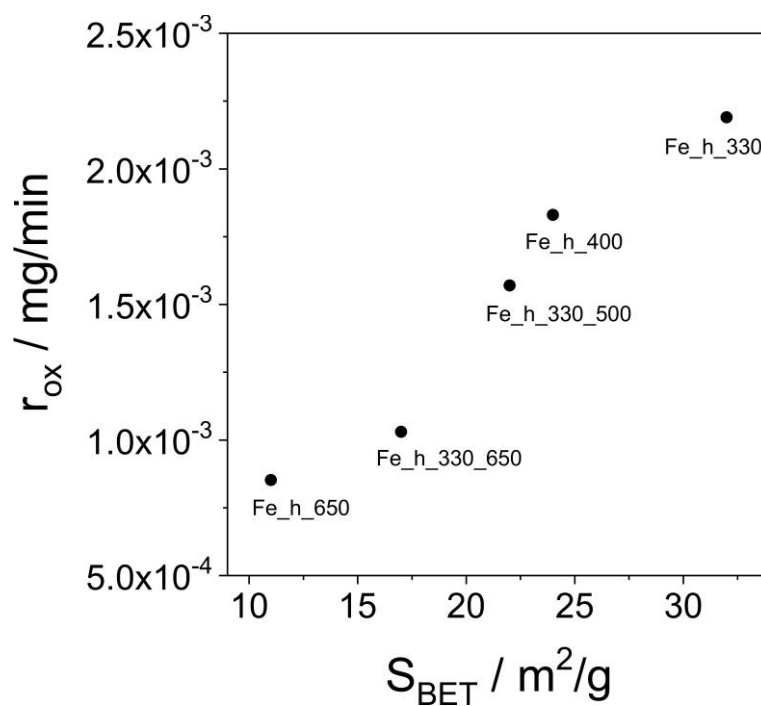
Figure A.4.   The correlation between the initial oxidation rates and the specific surface area of fresh magnetite containing catalysts.

Table A.1. Catalytic performance of the present and various state-of-art Fe-based non-supported and non-doped materials.

Catalyst	T / °C	P / bar	GHSV / ml/g$_{cat}$/h	X(CO$_2$) / %	S(CO) / %	S(CH$_4$) / %	S(C$_{2+}$) / %	O/P[a]	Ref.
Fe$_2$O$_3$	300	25	560	30.8	15.7	30.1	54.2	0.0132	[133]
Fe$_2$O$_3$_P	300	10	1140	18	16	37	47	0.1	[75]
Fe$_2$O$_3$_CT600	300	10	1140	23	21	14	65	1.4	[75]
Fe$_2$O$_3$_CT900	300	10	1140	21	29	36	35	0.2	[75]
Fe	300	10.1	15500	26.9	19	38.5	41.9		[89]
Fe	340	20	6000	12.5	31.9	49.2	50.8		[134]
Fe$_2$O$_3$	300	10	1800	14.3	33.2	40.21	26.59	0.03	[135]
Fe	340	20	1200	5.6	12	54.56	34.23		[96]
Fe$_2$O$_3$	320	5	1000	44.47	8.88	50.87	37.63	0.3272	[136]
Fe$_2$O$_3$	400	50	3000	8	78.75	12.5	8.75		[136]
Fe$_3$O$_4$	320	30	2040	22.8	8	41.2	50.8	0.2	[101]
Fe$_3$O$_4$	320	30	2000	29.3	16.6	50.29	33.03		[137]
Fe$_3$O$_4$	320	30	4000	9.2	97.9	2.09	0.01		[138]
100Fe	220	9.2	2000	2.4	25.8	58.9	15		[138]
100Fe	270	9.2	2000	21.8	17.3	64.7	16.9		[138]

Catalyst	T / °C	P / bar	GHSV / ml/g_{cat}/h	X(CO_2) / %	S(CO) / %	S(CH_4) / %	S(C_{2+}) / %	O/P[a]	Ref.
100Fe	300	10.1	8280	16.6	43	24.62	32.09	0.7	[81]
Fe_3O_4	320	30	8000	21.4	10.6	46.80	41		[139]
Fe_2O_3-230	230	1.6	6000	9.2	35.2	28.8	36		[79]
Fe_2O_3-190	230	1.6	6000	13.6	22.2	25	52.8		[79]
Fe_2O_3-43	230	1.6	6000	7.4	48.1	21.1	30.8		[79]
Fe_3O_4-pur	320	0.5	560	27.3	31.9	24.79	43.31	0.17	[80]
Fe_3O_4-EDA	320	0.5	560	21.8	13.6	23.07	63.33	0.4395	[80]
Fe_3O_4-NaAc	320	0.5	560	30.4	18.5	9.78	71.72	6.5111	[80]
Fe_3O_4-NaOH	320	0.5	560	30.0	22.9	10.25	66.85	4.3692	[80]
Fe_h_330	300	15	1170	29.18	19.72	24.32	55.95	1.0022	Present work
Fe_h_330_500	300	15	1170	23.47	40.87	8.64	50.49	5.9743	Present work
Fe_h_330_650	300	15	1170	19.47	62.48	4.77	32.75	5.2802	Present work

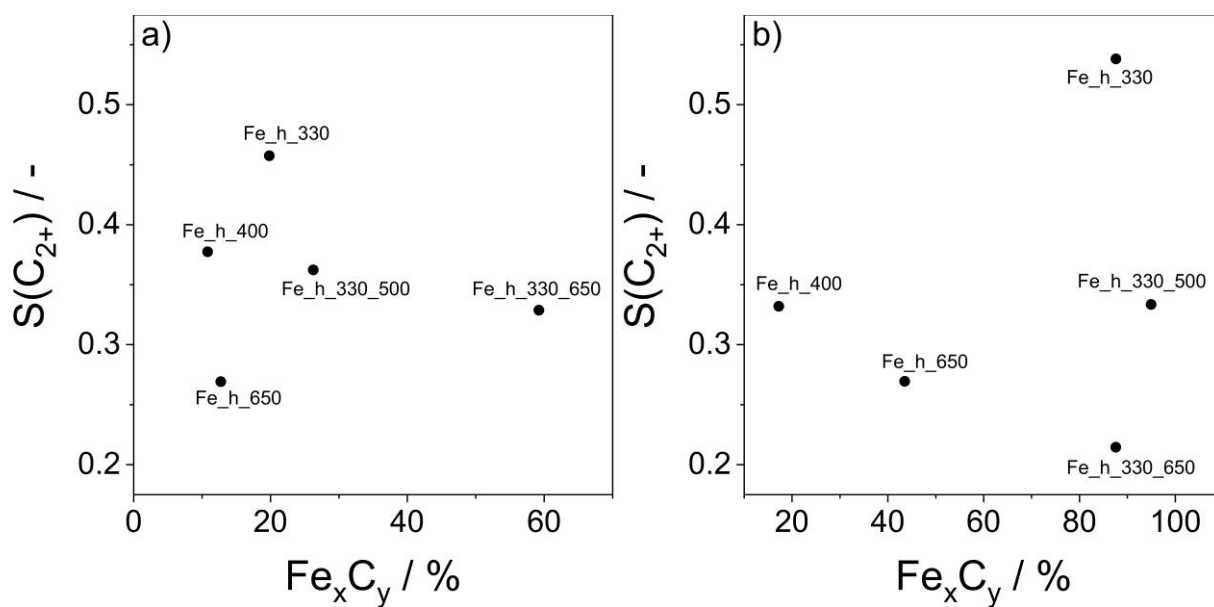a. *The ratio of olefin to paraffin within the C_2-C_4 hydrocarbons.*

Figure A.5. Selectivity to C_{2+}-hydrocarbons in CO_2 hydrogenation tests versus content of Fe_xC_y in spent (a) 300 mg or (b) 50 mg catalysts. Reaction conditions: 300 °C, $CO_2:H_2:N_2 = 1:3:0.3$, total flow: 5.85 mL/min.
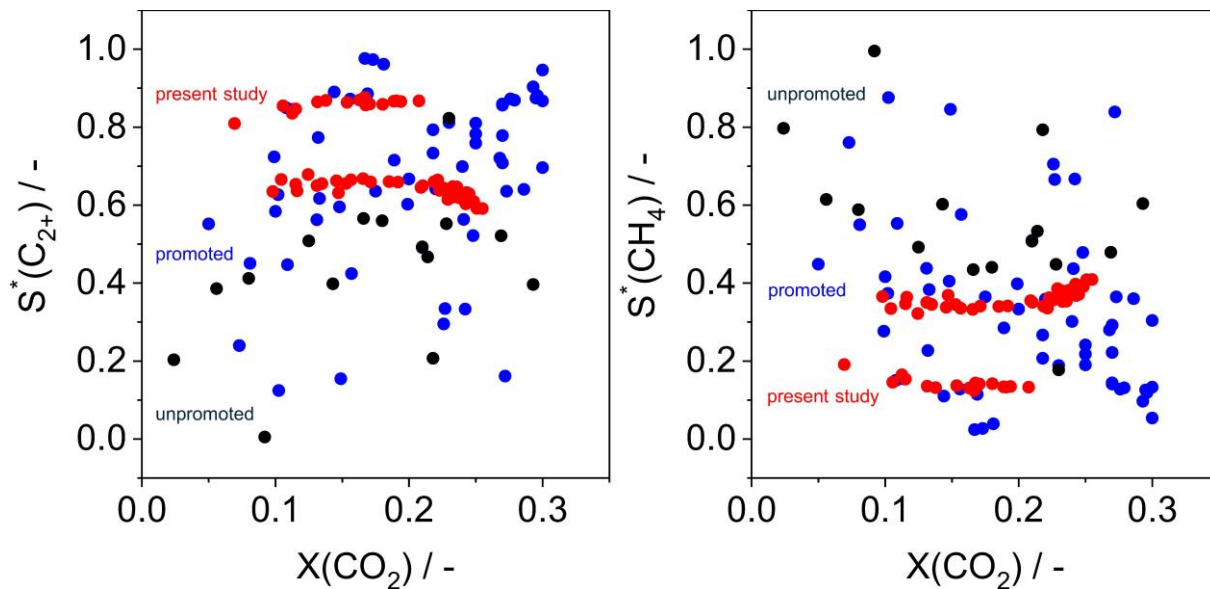
Figure A.6. CH$_4$ distribution among all hydrocarbons (without accounting CO) versus CO$_2$ conversion obtained over the present Fe$_2$O$_3$ catalysts (red dots) and previously reported non-supported unpromoted (black dots)[75, 89, 91, 92, 94, 96, 101, 133-139] or promoted non-supported (blue dots) [77, 80, 89, 91, 92, 94, 96, 101, 133-146] Fe-based materials.
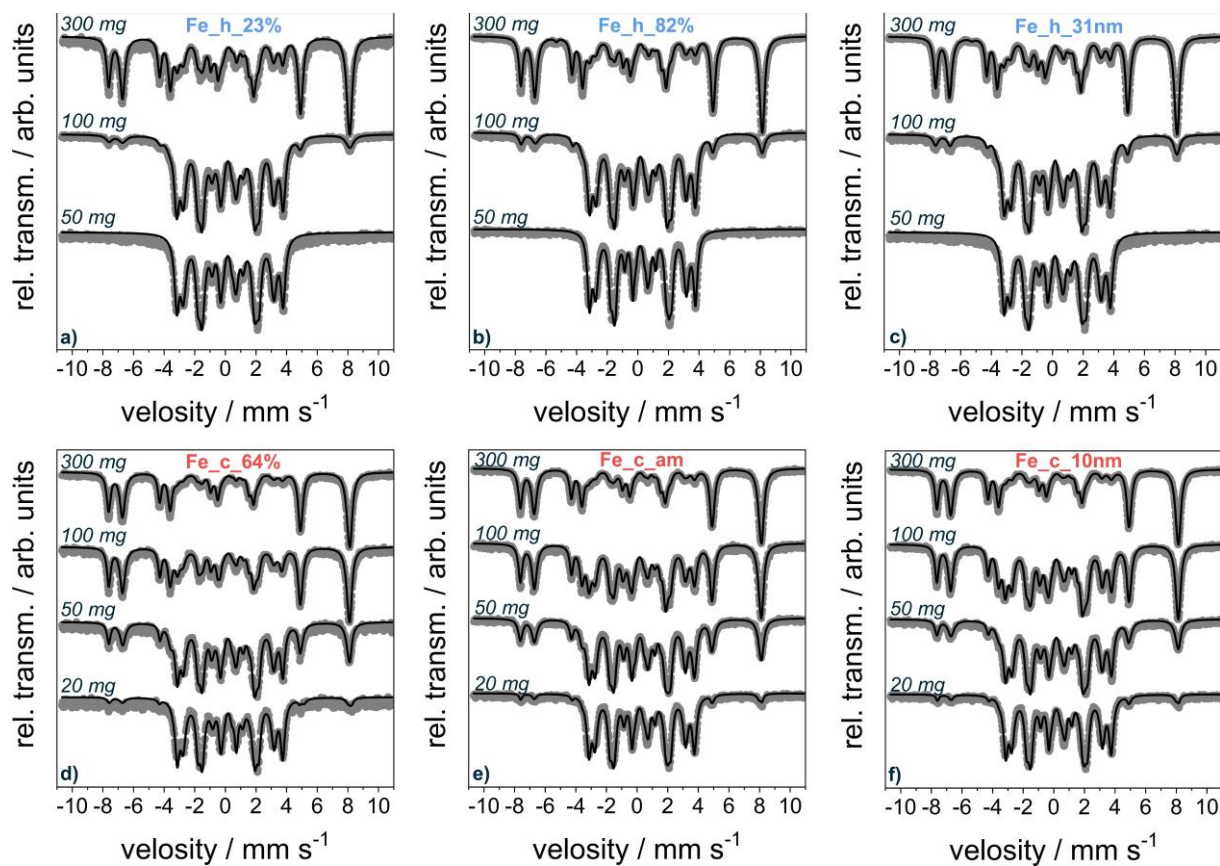
Figure A.7. Mössbauer spectra of selected spent catalysts (after CO_2 hydrogenation tests over 110 h on stream at 300 °C). Gray dots and black lines represent experimental spectra and fits, respectively.
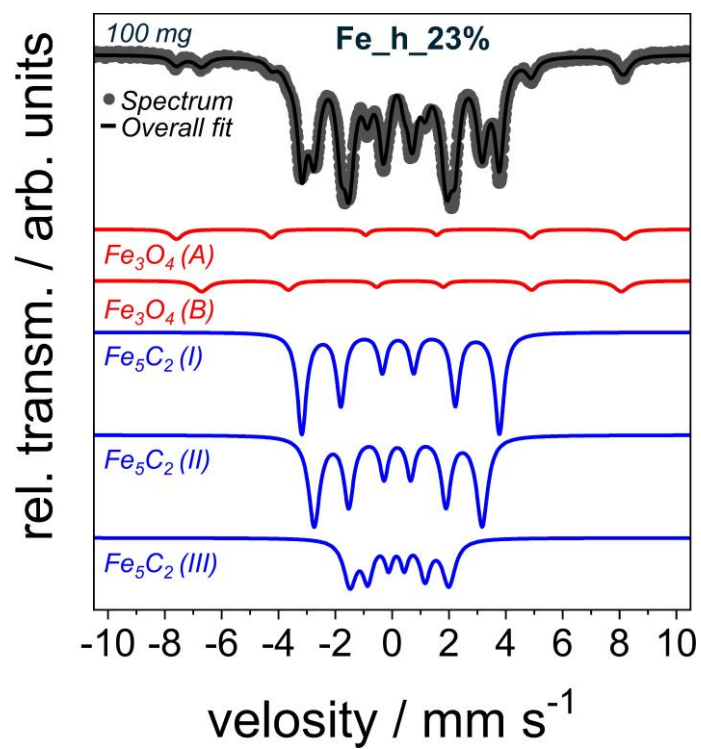
Figure A.8. An example of spectrum deconvolution using Lorentzian functions representing different Fe states in the individual Fe-containing phases in the spent Fe_h_23% sample (100 mg fraction).
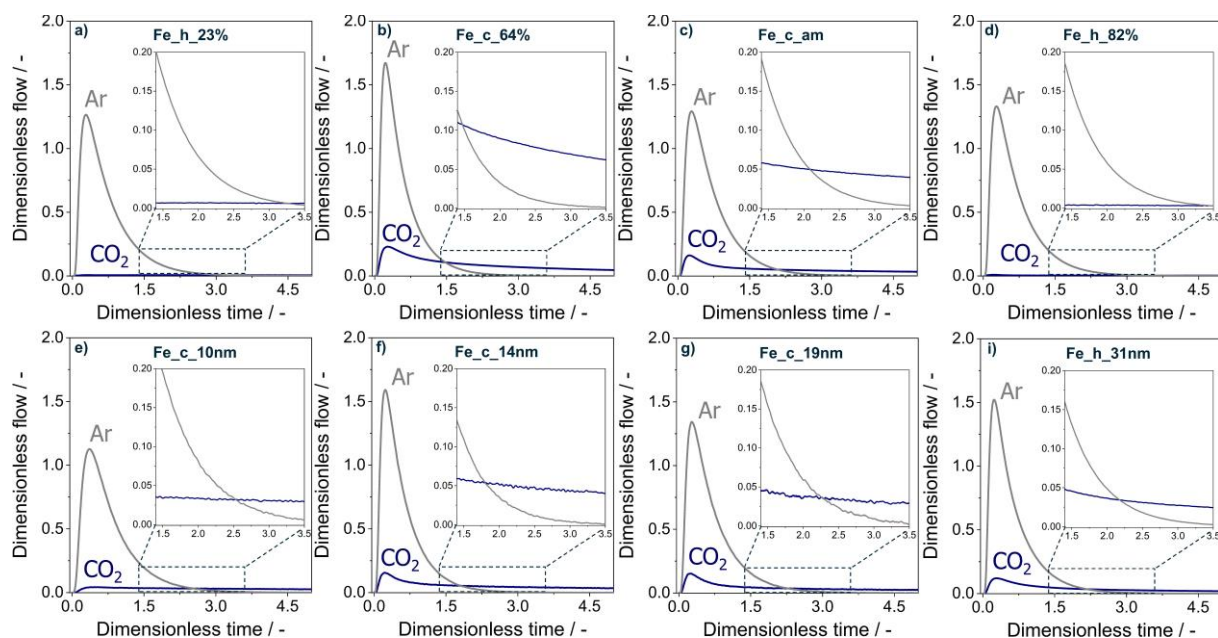
Figure A.9. Dimensionless responses of Ar and CO_2 obtained after pulsing of CO_2:Ar = 1:1 at 300 °C over selected spent catalysts (100 mg fraction).
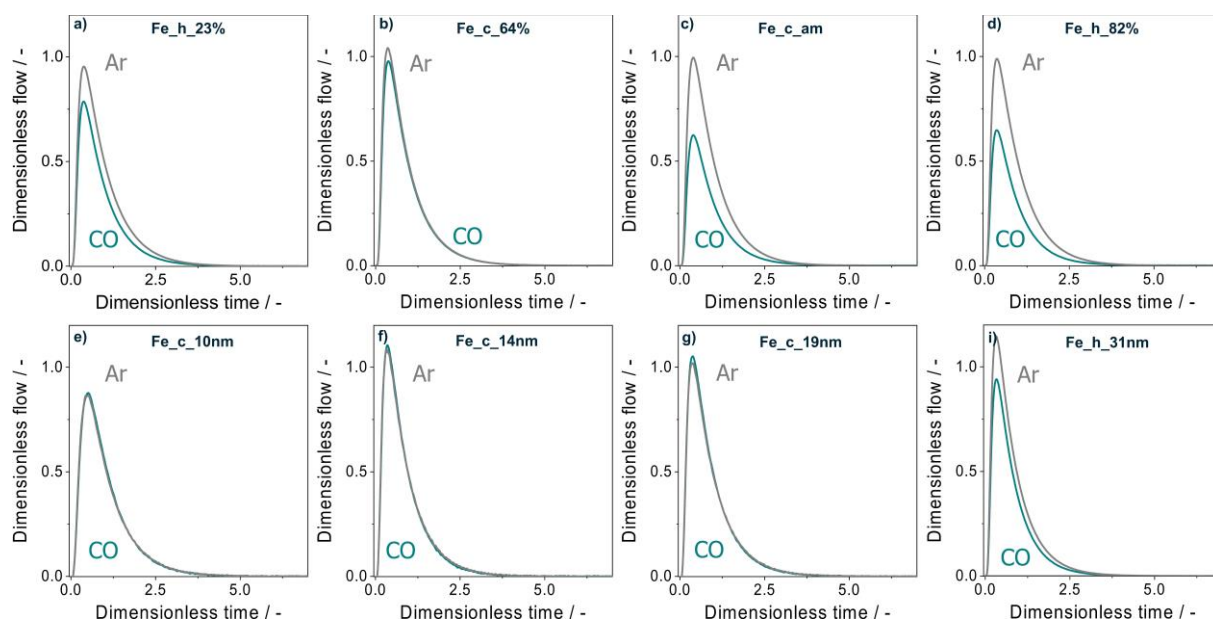
Figure A.10. Dimensionless responses of Ar and CO obtained after pulsing of CO:Ar = 1:1 at 300 °C over selected spent catalysts (100 mg fraction).
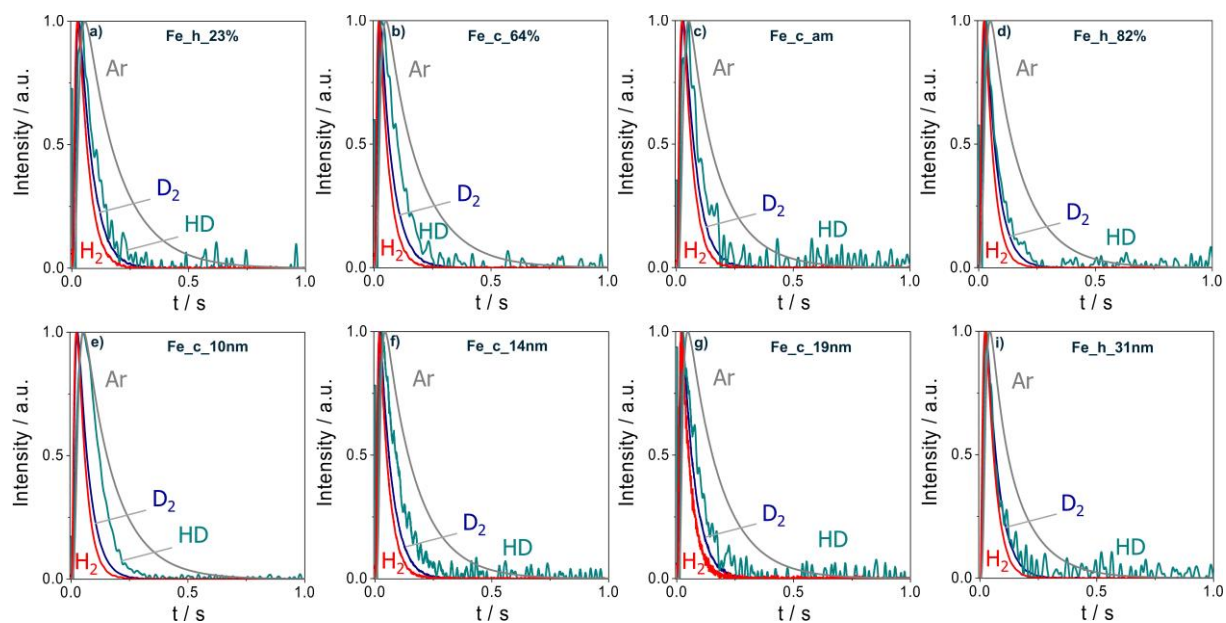
Figure A.11. Height-normalized responses of Ar, H_2, D_2 and HD obtained after pulsing of $H_2/D_2/Ar = 1:1:1$ at 400 °C over selected spent catalysts (100 mg fraction).

Table A.2. Hyperfine field of different Fe states in the perfect Fe_5C_2 structure obtained experimentally in [131] at 0 and 298 K.

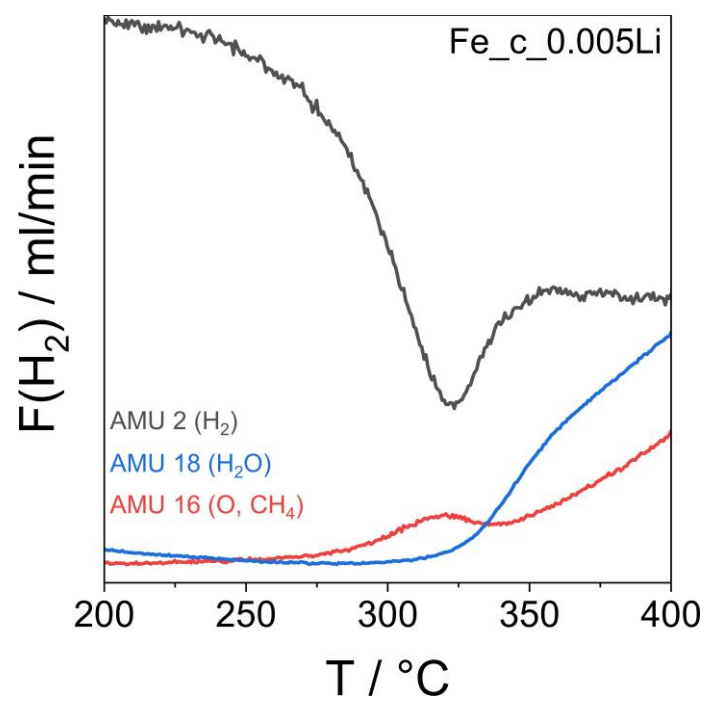| Fe state	B_{hf} (0 K) / T	B_{hf} (298 K) / T	B_{hf} (0 K)/B_{hf} (298 K) / -
I	26.1	21.5	1.214
II	22.7	18.3	1.240
III	13.8	10.8	1.278

Figure A.12. Hydrogen consumption peak attributed to iron carbides hydrogenation with the yield of CH_4 presented for selected 0.005Li/Fe fresh catalyst.

Liste der Publikationen

1. **Skrypnik, A.S.**, Petrov, S.A., Kondratenko, V.A., Yang, Q., Lund, H., Matvienko, A.A., Kondratenko, E.V., *Descriptors affecting methane selectivity in CO_2 hydrogenation over unpromoted bulk iron(III)-based catalysts,* ASC Catal. 2022, in print.

2. **Skrypnik, A.S.**, Yang, Q., Matvienko, A.A., Bychkov, V.Yu., Tulenin, Y.P., Lund, H., Petrov, S.A., Kraehnert, R., Arinchtein, A., Weiss, J., Brueckner, A., Kondratenko, E.V., *Understanding reaction-induced restructuring of well-defined $Fe_xO_yC_z$ compositions and its effect on CO_2 hydrogenation,* Appl. Catal. B 2021, 291, 120121.

DOI: 10.1016/j.apcatb.2021.120121.

3. Yang, Q., Kondratenko, V.A., Petrov, S.A., Doronkin, D.E., Saraci, E., Lund, H., Arinchtein, A., Kraehnert, R., **Skrypnik, A.S.**, Matvienko, A.A., Kondratenko, E.V., *Identifying Performance Descriptors in CO_2 Hydrogenation over Iron-based Catalysts Promoted with Alkali Metals,* Angew Chem Int Ed Engl 2022, 61, 1 – 9.

DOI: 10.1002/anie.202116517.

4. Yang, Q., **Skrypnik, A.S.**, Matvienko, A.A., Lund, H., Holena, M., Kondratenko, E.V., *Revealing property-performance relationships for efficient CO_2 hydrogenation to higher hydrocarbons over Fe-based catalysts: Statistical analysis of literature data and its experimental validation*, Appl. Catal. B 2021, 282, 1-11.

DOI: 10.1016/j.apcatb.2020.119554.

5. **Skrypnik, A.S.**, Matvienko, A.A., *The study of Nickel product morphology developed during the gaseous reduction of Nickel oxide,* Materials Today: Proceedings 2017, 4, 11425-11429.

DOI: 10.1016/j.matpr.2017.09.021.

6. Tretyakov, E.V., Peshkov, R.Y., Panteleeva, E.V., **Scrypnik, A.S.**, Stass, D.V., Romanenko, G.V., Ovcharenko, V.I., *Addition of cyanomethyl anion to the cyano group of 2-cyano-4,4,5,5-tetramethyl-4,5-dihydro-1H-imidazol-3-oxide-1-oxyl, a nitronyl nitroxide,* Tetrahedron Lett. 2016, 57, 2327-2330.

DOI: 10.1016/j.tetlet.2016.04.070.

Wissenschaftliche Beiträge

Vorträge

1. <u>Skrypnik, A.S.</u>, Matvienko, A.A., *The study of the formation of porous nickel in the reduction of nickel oxide by hydrogen*, Russia-Japan Joint Seminar "Non-equilibrium processing of materials: experiments and modeling", Novosibirsk, Russia, 02. – 04. October **2018**.

2. <u>Skrypnik, A.S.</u>, *The study of the mechanism of porous nickel formation during the gaseous reduction of bulk and nanocrystalline nickel oxide with hydrogen,* 56th International Students Scientific Conference, Novosibirsk, Russia, 22. – 27. April **2018**.

3. <u>Skrypnik, A.S.</u>, Matvienko, A.A., *The study of the morphology and the analysis of the microstructure evolution of porous metallic nickel during the thermal decomposition of nickel oxalate dihydrate*, 3rd International Russia-Kazakhstan Scientific-Applied Conference "Chemical Technology of Functional Materials", Novosibirsk, Russia, 29. – 30. April **2017**.

4. <u>Skrypnik, A.S.</u>, *The study of the mechanism of porous nickel formation during the gaseous reduction of bulk and nanocrystalline nickel oxide*, 55th International Students Scientific Conference, Novosibirsk, Russia, 16. – 20. April **2017**.

5. <u>Skrypnik, A.S.</u>, Matvienko, A.A., *The study of porous metal nickel microstructure developed during the gaseous reduction of nanocrystalline nickel oxide*, Japan-Russia Joint Seminar „Advanced Materials: Synthesis Process and Nanostructure", Sendai, Japan, 19. – 24. March **2017**.

6. <u>Skrypnik, A.S.</u>, Matvienko, A.A., *The study of nickel product morphology developed during the gaseous reduction of nickel oxide*, Russia-Japan Joint Seminar "Advanced Materials: Synthesis, Processing and Properties of Nanostructures", Novosibirsk, Russia, 01. – 03. November **2016**.

Poster

1. <u>Skrypnik, A.S.</u>, Yang, Q., Matvienko, A.A., Petrov, S.A., Kondratenko, E.V., *Controlling methane selectivity in CO_2 hydrogenation over Fe_2O_3-based catalysts: effects of iron precursor, particle size and initial composition*, 55. Jahrestreffen Deutscher Katalytiker, Weimar, Germany, 27. – 29. June **2022**.

2. <u>Skrypnik, A.S.</u>, Yang, Q., Matvienko, A.A., Petrov, S.A., Kondratenko, E.V., *Fe-based catalysts for CO$_2$ Fisher-Tropsch: effects of iron precursor and treatment procedure on Fe-carbides formation and product selectivities*, 54. Jahrestreffen Deutscher Katalytiker, online event, 16. – 19. March **2021**.

3. <u>Skrypnik, A.S.</u>, Yang, Q., Matvienko, A.A., Petrov, S.A., Kondratenko, E.V., *Fe-based catalysts for CO$_2$ Fisher-Tropsch: effects of iron precursor and treatment procedure on Fe-carbides formation and product selectivities*, SPP2080 Status Colloquium 2021, online event, 23. – 26. February **2021**.

4. <u>Skrypnik, A.S.</u>, Yang, Q., Matvienko, A.A., Lund, H., Petrov, S.A., Kondratenko, E.V., *Approaches for revealing property-performance relationships in CO$_2$ hydrogenation to higher hydrocarbons*, Audit LIKAT, online event, 23. November **2020**.

5. <u>Skrypnik, A.S.</u>, Matvienko, A.A., *The study of the formation mechanism of porous nickel during the gaseous reduction with hydrogen of bulk and nanocrystalline nickel oxide,* Lomonosov conference, Moscow, Russia, 09. – 13. April **2018**.

Curriculum vitae

Lebenslauf

Name: Andrey Stanislavovich Skrypnik

Geboren am: 16. September 1995 in Kemerowo

Staatsangehörigkeit: russisch

Promotion

10/2019 – 09/2022	Doktorarbeit am Leibniz-Institut für Katalyse e.V. an der Universität Rostock Betreuer: Herr Prof. Dr. habil. E.V. Kondratenko Titel der Arbeit: *„Iron-based catalysts for CO_2 conversion into higher hydrocarbons"*

Studium

09/2013 – 06/2018	Chemiestudium an der Staatlichen Universität Nowosibirsk, Diplom Titel der Arbeit: *„Study of porous nickel formation mechanism during hydrogen reduction of bulk and nanocrystalline nickel oxide"*

Schulabschluss

2011 – 2013	Erlangung der Allgemeinen Hochschulreife am klassischen Lyzeum in Kemerowo, Russland

Kurse

2017	Deutsch als Fremdsprache – Deutsch B1, Hotel- und Wirtschaftsschule, Rostock
2016 – 2019	Praktikum im Novosibirsk Technology Center, Shlumberger, Nowosibirsk

Auszeichnungen und weitere Tätigkeiten

2019 – 2020	Forschungsstipendium des DAAD
2017 – 2018	Staatliches Studienstipendium
2016	Stipendium des Institute of Solid State Chemistry and Mechanochemistry

Die Teilnahme an Bildungswettbewerben

2018	Diplom des 3. Grades in International Scientific Student Conference
2017	Diplom des 2. Grades in 3rd International Russian-Kazakh Conference "Chemical Technologies of Functional Materials
2012 – 2013	Russlandweite Schüler-Olympiade in Chemie: • Mitglied der vierten regionale Etappe (Kemerowo, Russland) • 1. Platz in der Stadt Kemerowo (dritte Etappe) • 2. Platz in der Bezirksklasse in Kemerowo (zweite Etappe) • 2. Platz in der Schule in Kemerowo (erste Etappe) Diplom des 3. Grades in der gesamtsibirischen Olympiade (Nowosibirsk, Russland)
2011 – 2012	Russlandweite Schüler-Olympiade in Chemie: • Mitglied der vierten regionale Etappe (Kemerowo, Russland) • 2. Platz in der Stadt Kemerowo (dritte Etappe) • 1. Platz in der Bezirksklasse in Kemerowo (zweite Etappe)

	• 1. Platz in der Schule in Kemerowo (erste Etappe)
2010 – 2011	Russlandweite Schüler-Olympiade in Chemie:
	• 3. Platz in der Region Kemerowo (vierte Etappe)
	• 3. Platz in der Stadt Kemerowo (dritte Etappe)
	• 1. Platz in der Bezirksklasse Kemerowo (zweite Etappe)
	• 1. Platz in der Schule in Kemerowo (erste Etappe)

Sport

2012	Teilnahme an dem Tischtennis Universitätswettbewerb
	2. Platz in dem Tischtennis Wohnheimwettbewerb